KATHOLIEKE
UNIVERSITEIT
LEUVEN

Faculteit Ingenieurswetenschappen
Departement Elektrotechniek (ESAT)
Katholieke Universiteit Leuven

joint to

Facoltà di Ingegneria
Dipartimento di Ingegneria Elettrica, Elettronica
e delle Telecomunicazioni (DIEET)
Università degli Studi di Palermo

Università degli Studi
di Palermo

From surface plasmon resonance based sensors to carbon nanotube based sensors

Supervisors:

Prof. Dr. G. Groeseneken

Prof. Dr. C. Van Haesendonck

Prof. Dr. S. Riva Sanseverino
(Coordinatore del corso di Dottorato)

PhD thesis presented for the joint degree of Dottore di Ricerca in Ingegneria Elettronica e delle Telecomunicazioni (XXI ciclo, SSD: ING-INF/01, Elettronica) from the Università degli Studi di Palermo and of Doctor of Engineering from the Katholieke Universiteit Leuven.

PhD candidate:
Claudia Santini

2011

Contents

List of abbreviations

SP: surface plasmon
SPR: surface plasmon resonance
LN: lithium niobate
TM: transverse magnetic field
PE: proton exchange
CNT: carbon nanotube
SWNT: single-walled carbon nanotube
MWNT: multi-walled carbon nanotube
CVD: chemical vapor deposition
NEMS: nanoelectromechanical system
AFM: atomic force microscopy
SEM: scanning electron microscopy
TEM: transmission electron microscopy
EDX: energy dispersive X-ray spectroscopy
ECD: electro-chemical deposition
KPFM: Kelvin probe force microscopy
FIB: focused ion beam
PVD: physical vapor deposition
CMOS: complementary metal oxide semiconductor
SPM: scanning probe microscopy
EFM: electrostatic force microscopy

Introduction

A sensor is a device able to detect and measure physical quantities of a specific sample, the analyte, by measuring changes caused by these quantities on, for example, the electrical, mechanical or optical properties of the sensing element, the transducer [1]. Gas, temperature, pressure, mass sensors have important applications in a wide variety of fields ranging from medical diagnosis and alimentary safety to automotive industry and environmental monitoring [1].

Next generation sensing devices require significant improvements in order to satisfy the needs of such a wide variety of applications. In the first place the sensors require a high degree of sensitivity and specificity, in order to detect different targets with greater precision. On the other hand, the sensors should be low-cost and "label-free", employing sensing methods whereby the target itself does not require tagging with, for example, a fluorescent label. Finally, the sensors have to be compact, robust, reliable and allow for real-time measurements [1].

The advent of nanotechnology has generated great expectations towards developing new sensing methods and devices with the above discussed characteristics [2]. In particular, nanotechnology may enable the production of sensors with reduced size and weight, lower power consumption and lower cost. Moreover, at the nanoscale the materials are governed by different laws and offer different properties than in the macroscopic world. This aspect makes nanotechnology an important opportunity to develop new fascinating sensing approaches.

The need to reduce the size of the sensing devices is certainly in line with the driving trend of semiconductor industry as reflected by Moore's law [3]. This law tracks the increase of the integration density in electronic devices and, consequently, of the computational speed and data storage capacity. Similarly, the sensor related industry tends to produce smaller and smaller sensors in order to make them cheaper and lighter, to increase the number of sensors on the same chip, i.e. the sensing capacity, to integrate them into bigger devices and to produce, for example, biomedical sensors for minimally invasive diagnoses [2]. Another reason to look for smaller sensing devices is that most viruses, bacteria, pathogens, particles in gas phase and other chemical-biological agents, typically the targets of the sensing investigations, have small (below 1 μm) dimensions [4]. As such, nanoscale sensors can offer the required sensitivity to the analyte of interest.

Between the various types of sensors two are of particular interest: sensors based on surface plasmon resonance (SPR) [5] and sensors based on carbon nanotubes (CNTs) [6]. Both types of sensors allow for compact and small sensing devices. Note, however, that the dimensions of the carbon nanotubes allow to build sensors as small as a few microns while SPR sensors typically have three orders of magnitude larger dimensions. Both types of sensors allow a label-free and real-time detection. In these sensors the sensing mechanism is based on an event that induces a change

- of the power of the output wave from an optical device in the case of SPR sensors,
- of the electrical, mechanical and/or optical properties of the CNTs for CNT based sensors.

Such an event is in some way connected to the physical quantity to be measured, for example,

- for SPR sensors: the presence of contaminants in the analyte, a binding event with a particular chemical or biological element, the thickness of a thin film, the humidity, the temperature, the presence of gas in the surrounding environment and, in general, any event able to cause a change of the refractive index of the surface just above the transducer [5];
- for CNT sensors: the temperature, the humidity, the presence of gas, the pressure, a mechanical stress, an electric field and, in general, any event able to cause a change of one of the CNT properties [6].

Within thirty and twenty years from the discovery of the SPR as sensing technique and of the CNTs, respectively, both SPR and CNT sensors have demonstrated the potential to move the sensor industry towards smaller, lighter and towards more compact, sensitive and reliable sensors. Actually the two sensing techniques can be considered as being complementary, since SPR sensors offer high sensitivity while CNT based sensors are highly reliable. Recently, a dual-mode (SPR and CNT) biosensor has been proposed that enables the detection of biological events by simultaneously measuring changes in both the CNT electrical conductance and the SPR [7]. As such, this sensor provides both high sensitivity and reliability. Despite their promising features, many challenges remain, however, to be addressed before the full potential of SPR and CNT sensors can be developed.

Regarding the SPR sensors there is an increasing need to fabricate smaller sensors that can be integrated within the same chip and are able to detect different analytes (multi-analyte sensors) [5]. This would reduce the fabrication costs and enable the production of compact and versatile all-optical sensors that, for example, when using optical fibers, may allow to be remotely controlled.

Regarding the CNT sensors, the primary need is to gain control over the CNT growth and properties in order to be able to fabricate reliable and reproducible CNT sensors [6]. In particular, as the most promising CNT based sensors are electrical sensors (i.e. where the CNT electrical properties are sensitive to the surrounding environment, e.g., in terms of temperature [8], humidity [9], presence of gas [10] and to mechanical excitations [11]), the issues to be addressed are the same as the ones faced by the semiconductor industry to produce CNT electrical interconnects [12]: to control the CNT positioning and growth, e.g. to grow CNT horizontal interconnects, to avoid the high contact resistance between CNTs and metal, that dominates the overall CNT interconnect performance, and to improve the electrical, thermal and mechanical properties of CNTs grown by chemical vapor deposition (CVD).

The interest of the semiconductor industry in producing CNT electrical interconnects comes from the unique properties of the CNTs which add to their fascinating properties for sensing applications. CNTs are able to transport current as ballistic conductors [13] with current densities as high as 10^9 A/cm^2 [14]. On the other hand, CNTs can have a Young modulus up to 1 TPa [15] and a thermal conductivity of several thousands W/mK [16]. With the increase of the integration density of the electronic circuits, copper, traditionally used for interconnects, will not be able to carry the required current densities, as copper fails above 10^6 A/cm^2 due to electromigration [17]. CNTs do not suffer from electromigration thanks to the strength and directionality of their C-C covalent bonds and they can carry a current density up to three orders of magnitude higher [18, 19].

This thesis discusses the above described problems for SPR sensors (**Part I**) and CNT sensors (**Part II**) and proposes some approaches to solve these problems. **Part I** of the thesis is presented in **Chapter 1**.

Chapter 1 describes the design of a novel SPR sensor built on a lithium niobate channel waveguide. This study is carried out by numerical simulations with a field mode matching approach. The results demonstrate that in such a sensor the resonance occurs between refractive indices of 1.8 and 2, which enables to analyse high index oxides or polymeric materials. The sensitivity of this sensor can be optimised by changing design parameters such as cut of the crystal, wavelength of the input light, and thickness and length of the metal layer. Next, it is demonstrated that the resonance can be shifted down to a refractive index range of 1.3-1.4, if a thin layer with high refractive index is introduced in the sensor structure between the metal layer and the analyte. Though this solution produces a slightly more complex sensor with a reduced sensitivity, it leads to an important and more general conclusion. It demonstrates that it is possible to integrate many SPR sensors on the same substrate, each of them dedicated to a different analyte (multi-analyte sensor) by simply depositing different matching layers according to the materials we want to analyse.

Part II of the thesis discusses the growth and the characterisation of CNTs for electrical interconnects and sensing applications. **Chapter 2** describes a novel growth technique that allows to grow horizontally suspended CNTs connecting metal electrodes. The technique relies on the selective placement of Ni catalyst nanoparticles on the electrode sidewalls by electrochemical deposition (ECD). ECD has an intrinsic selective nature, since metal deposition only occurs on (semi)conductive surfaces contacted as the cathode. Therefore, when combined with appropriately designed electrode configurations, it does not require further processing to remove unwanted metal catalyst. Moreover, the ECD method allows excellent control of the Ni nanoparticle density and size distribution, that is translated into a similar control over the CNT density and diameter distribution [20–23]. This approach allows us to routinely grow CNTs from one metal electrode towards an opposing one or from both opposing electrodes.

Chapter 3 proposes a novel effective and scalable solution to solve the issue of the high electrical contact resistance in CNT electrical interconnects. In particular, we suggest to replace CNT-metal contacts by CNT-CNT contacts that are demonstrated to have a considerably lower resistance. First, we show that the growth method proposed in Chapter 2 allows to electrically connect opposing electrodes with electrode gaps up to 5μm. CNT interconnect resistances as low as 40 Ω are measured for the smallest electrode gap (200 nm) and CNTs grown from both opposing electrodes. Next, in order to evaluate the role of the different contact scenarios, low density CNT interconnects are characterised qualitatively by using Kelvin probe force microscopy (KPFM) [24] and quantitatively by electrical transport measurements. When two CNTs grow from opposing electrodes and touch each other with their outermost shells, the corresponding contact resistivity is about 14 $\Omega\mu\text{m}^2$, one order of magnitude smaller than the contact resistivity of a CNT touching the TiN electrode surface with its outermost shell. On the other hand, the contact resistance of a CNT grown from a Ni catalyst particle deposited on a TiN electrode is negligibly small when compared to the above mentioned contact resistances. Since the proposed growth method allows to create CNT-CNT contacts with a contacting yield (number of contacts out of the number of CNTs growing from the electrodes) of up to 90%, this method may provide a scalable alternative to obtain low resistance CNT horizontal interconnects.

In **Chapter 4** we investigate the breakdown of the CNT interconnects induced by Joule heating under atmospheric pressure and high vacuum (10^{-5} mbar) conditions. The electrochemical deposition described in Chapter 2 is repeated after CNT growth to decorate the CNT interconnects with Ni nanoparticles. The melting of these particles under vacuum after Joule heating induced CNT breakdown reveals that the CNTs reach temperatures higher than the Ni melting temperature (around 1500 °C). The electrical and thermal properties of the CNT interconnects are inferred from the breakdown conditions. The results of this chapter demonstrate that as-grown CNTs can carry powers up to 0.6 mW under vacuum, three times higher than under atmospheric pressure, with a maximum current density ranging from 10^6 A/cm^2 up to 10^8 A/cm^2 and a thermal conductivity up to 200 W/mK at room temperature. The experimental results presented in this chapter provide new insight into the electrical characterisation and breakdown of the CNTs and indicate that the proposed growth method is able to produce CNTs with good properties for interconnects and sensing applications.

Finally, in **Chapter 5** we probe the mechanical properties of CNTs that are grown for sensing applications. In particular, we propose a novel method to induce the mechanical resonances of the suspended CNTs that resembles the magnetic resonance force microscopy (MRFM) technique [25, 26]. This method relies on the creation of a force gradient induced by an external inhomogeneous magnetic field on CNTs loaded with Ni nanoparticles (Ni-CNTs) when these particles are at ferromagnetic resonance. Such a method is more advantageous than the traditional electrical excitation since it does not require the fabrication of high frequency circuits. Moreover, the resonance frequency of the Ni-CNTs is within the convenient range of tens of MHz, as an additional mass is added to the tip of the CNT oscillator [27]. The results described in this chapter demonstrate that the force experienced by the Ni particle spins immersed in a magnetic field, which is variable in space and in time, is able to drive the Ni-CNTs into oscillation up to resonance. Our results prove that the Ni-CNT resonance frequencies detected with the tip of an atomic force microscope (AFM) are in good agreement with the theoretical estimates and that the quality factor and, consequently, also the amplitude of the oscillations are sensitive to the presence of helium gas in the surrounding environment.

Part I
Surface Plasmon Resonance Sensors

Chapter 1

Surface Plasmon Resonance Sensors on Lithium Niobate

1.1 Introduction

Sensors based on the surface plasmon resonance (SPR) phenomenon were proposed for the first time in 1983 to measure the refractive index of organic layers adsorbed on a thin metal film [28]. From that time on SPR has been widely used as a detection technique in chemical and bio-chemical sensing, pharmaceutical research and environmental monitoring. SPR sensors are interesting for gaseous and liquid analysis and they allow for measurements of temperature, humidity, chemical and biological composition since all these parameters cause a variation of the refractive index of the measurand, called analyte [29]. They are also important for the analysis of solid materials. In particular, SPR sensors have been proposed to monitor processes of ion implantation [30] or to study the optical properties of thin films during their deposition [31]. Finally, SPR sensors have gained a big interest for biosensing applications such as detection of DNA, proteins, antibody-antigen interactions, cells and bacteria [32]. SPR sensors offer many peculiar advantages, including real time measurements, high sensitivity, no need for fluorescent labeling and immunity against electromagnetic interferences [28, 33, 34].

Between the possible configurations of SPR sensors, integrated optical waveguides offer numerous benefits such as the realization of compact and rugged sensing devices and the potential of fabricating multiple sensors on a single chip [35, 36]. In addition, in conjunction with optical fibers, optical waveguides may allow for the development of sensing devices that may be used remotely from both the source and the detector. Different types of waveguides have been proposed to build SPR sensors: planar waveguides [37], channel waveguides [36] and various other configurations [38].

SPR sensors are characterised by sensitivity, operating range and resolution [39]. The sensitivity is the slope of the sensor output curve, i.e. the slope of the output wave power with respect to the refractive index of the analyte. The operating range is the range of values of the parameter under measurement that can be detected by the sensor, i.e. where the resonance takes place. The resolution is the minimum change in the parameter under measurement that can be resolved by the sensor.

In most of the specific literature integrated optical SPR sensors are built on glass substrates [29]. These materials have refractive indices in the range of 1.3-1.4, that makes them able to analyse aqueous solutions, since they have an operating range around the refractive index of water (1.33 at a wavelength of 633 nm). On the other hand, materials such as lithium niobate (LN) and lithium tantalate, despite of their high refractive index, too high to analyse aqueous solutions, can be used to analyse polymers and solid layers and, moreover, offer several unique properties to build SPR sensors: fabrication of transverse magnetic (TM) only waveguides by the technique of the proton exchange (PE) [40], and acousto- thermo- and electro-optic control of their refractive index [41].

This chapter describes the design of a novel SPR sensor built on a LN PE channel waveguide by numerical simulations carried out with a field mode matching approach. First, it is shown that in such a sensor the operating range is always between 1.8 and 2, which makes it useful to analyse high index oxides or polymeric materials. The sensitivity and the resolution of this sensor can be optimised by changing some design parameters such as cut of the crystal, wavelength of the input light, thickness and length of the metal layer. Next, it is demonstrated that the operating range can be shifted down to a range of 1.3-1.4 if a thin layer with high refractive index (matching layer) is introduced in the sensor structure between the metal layer and the analyte. Though this solution produces a slightly more complex sensor with a reduced sensitivity and resolution, it leads to an important and more general conclusion. It demonstrates that it is possible to integrate many SPR waveguides on the same substrate each one dedicated to a different analyte, i.e. with different refractive index, by simply depositing different matching layers according to the material we want to analyse.

This research was carried out during the first year of the PhD work. It was developed in the framework of the Italian project "PON AGRO 12743 QUALI.BIO: Control of food quality through the use of biosensors made with microtechnology", both at the Department of Electrical, Electronics and Telecommunication Engineering (DIEET) of the University of Palermo and at the Electronics Research Centre of Sicily (CRES). Part of the results of this work has been published in a conference proceeding [42].

The first part of the chapter (Section 1.2) introduces the theoretical background by briefly describing the phenomenon of the SPR in Section 1.2.1 and the possible configurations of sensing in Section 1.2.2. The second part of the chapter (Section 1.3) describes the materials and methods used in this work, i.e. the LN in Section 1.3.1, the optical waveguides produced by PE in Section 1.3.2 and the simulation tools used in the design of the optical sensor in Section 1.3.3. Next, Section 1.4 presents the results related to the design of the SPR sensor realized on LN PE channel waveguides. In particular, Section 1.4.1 describes the behavior of the sensor by varying its design parameters in the case of intensity (Section 1.4.2) and wavelength (Section 1.4.3) interrogation. Section 1.4.4 presents a variant of this sensor that allows to tune the resonance refractive index. The chapter ends with a summary of the principal results (Section 1.5) and with some considerations concerning future work (Section 1.6).

1.2 Theoretical Background

1.2.1 Surface plasmon resonance

A surface plasmon (SP) wave is a charge density wave propagating along the interface between a metal and a dielectric medium [43]. It is a p-polarised wave, i.e. the magnetic field vector H is parallel to the incidence plane of the wave. As such, it can be excited only by a transverse magnetic (TM) optical light. Figure 1.1 (a) shows a schematic view of a SP wave traveling along the interface between a metal with permittivity ϵ_m and a dielectric with dielectric constant ϵ_d. An example of the distribution of the magnetic field intensity H of a SP wave in the direction of the y axis, perpendicular to the metal-dielectric interface is shown in Fig. 1.1 (b) for two different wavelengths λ. Note that the field is so-called "evanescent" as it is confined at the interface and decreases exponentially into both media.

An event of resonance occurs when the wave vector of a propagation mode in such an optical structure k_z matches the wave vector of the SP wave k_{SP}:

$$k_z = k_{SP}. \tag{1.1}$$

If the optical structure where the wave propagates is a waveguide as schematically presented in Fig. 1.1 (a), the Eq. (1.2) corresponds to:

$$\frac{2\pi}{\lambda} N_{eff} = \frac{2\pi}{\lambda} \sqrt{\frac{\epsilon_m \epsilon_d}{\epsilon_m + \epsilon_d}}, \tag{1.2}$$

where N_{eff} is the effective index of the waveguide. Under this condition, a maximum of the power of the wave propagating in the waveguide is transferred to the free electrons that propagate along the interface between the metal and the dielectric and the output power from the waveguide shows a minimum value. Since this resonance condition strongly depends on the refractive index of the dielectric through its dielectric constant ϵ_d, it is possible to sense changes of this index by a measurement of the characteristics of the output light wave. In the following we refer to this dielectric as “analyte” because it is the material we want to sense or “analyse”. Correspondingly we refer to $\epsilon_{analyte}$ and $n_{analyte}$ to indicate, respectively, the dielectric constant and the refractive index of the analyte.

1.2.2 Surface plasmon resonance sensing configurations

SPR sensors can be realised in different configurations: attenuated total reflection prism coupler, integrated optical waveguides either planar or channel-like, optical fibers and grating coupling [32]. A schematic view of these four different configurations is given in Fig. 1.2.

In a configuration based on prism coupling (Fig. 1.2 (a)) a light wave passes through a high refractive index prism and is totally reflected at the prism-metal layer interface. It generates an evanescent wave that penetrates the metal layer and propagates along the interface with a wave vector, which can be adjusted to match that of the SP wave by controlling the angle of incidence. In a configuration based on optical waveguides or optical fibers (Fig. 1.2 (b),(c)) the light wave is guided by an optical waveguide or an optical fiber, respectively, and, when entering the region with a thin metal layer, it evanescently penetrates through the metal layer exciting a SP wave at its outer boundary. Alternatively,

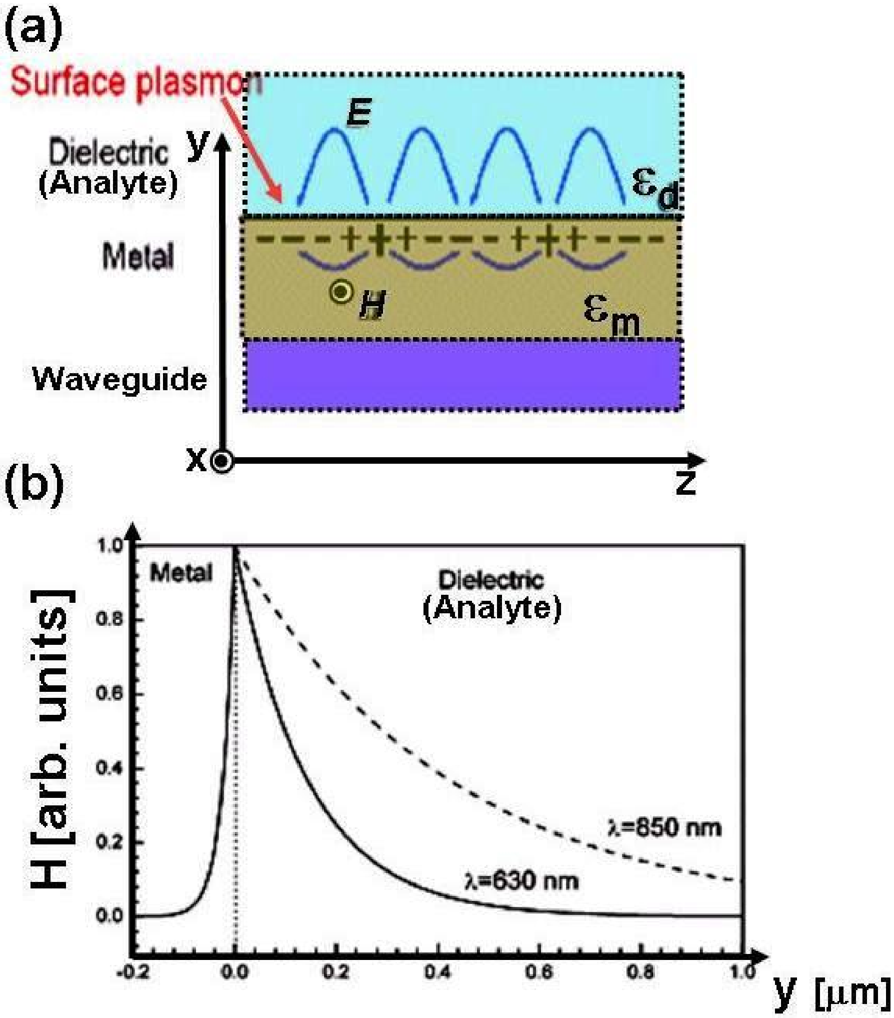

Figure 1.1: (a) Schematic view of a SP wave traveling along the interface between a metal with permittivity ϵ_m and a dielectric with dielectric constant ϵ_d. (b) Corresponding magnetic field intensity H of the SP wave in the direction perpendicular to the metal-dielectric interface for two different wavelengths λ [32].

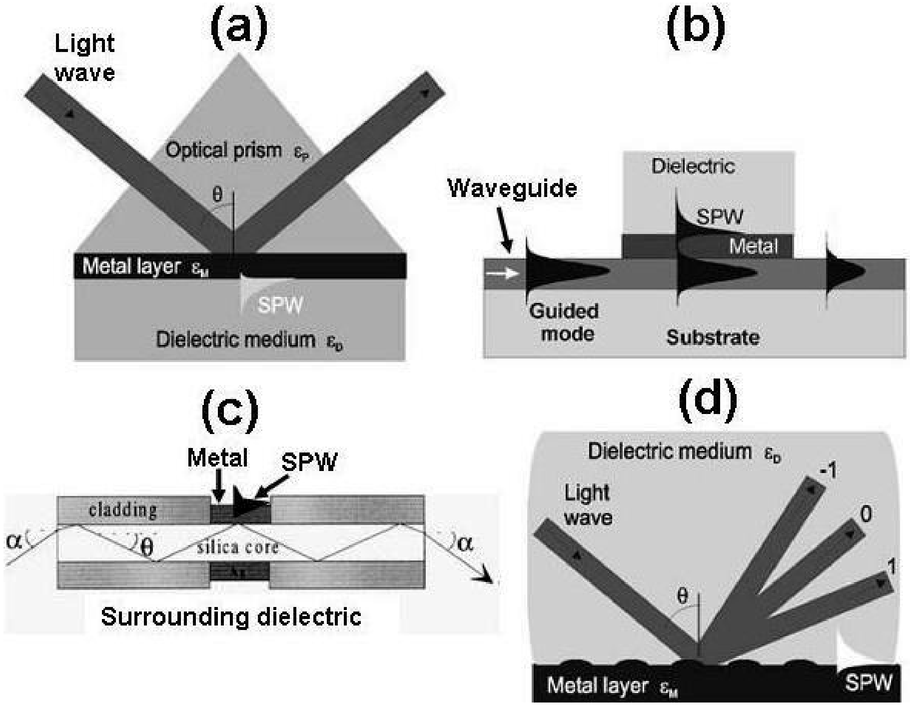

Figure 1.2: Excitation of surface plasmon waves: (a) by a light beam via prism coupling [32], (b) by a guided mode in an optical waveguide [32], (c) by a guided mode in an optical fiber [44] and (d) by light diffraction on a diffraction grating [32].

an SP wave can be excited by diffraction on a grating (Fig. 1.2 (d)). In this case the component of the wave vector of the diffracted waves parallel to the interface can be tuned by changing the period of the grating in order to match the wave vector of a SP wave.

In all these configurations the interaction of a light wave with an SP wave alters characteristics of the light that include amplitude, phase, polarisation and spectral distribution, depending on the analyte refractive index at the sensor surface [5]. Therefore, by measuring the changes of one of these characteristics it is possible to evaluate the changes of the refractive index of the analyte at the sensor surface. Based on which characteristic is measured, SPR sensors can be classified as angle, wavelength, intensity, phase, or polarization modulation interrogation sensors [32]. The following of the chapter is focused on sensors with intensity interrogation (Section 1.4.2). An example of a sensor with wavelength interrogation is presented in Section 1.4.3.

1.3 Materials and Methods

1.3.1 Lithium niobate

Lithium niobate ($LiNbO_3$, LN in brief) [41] is a trigonal single crystal widely used for optical applications such as optical waveguides, modulators and many linear and non-linear optical devices (e.g. devices for laser frequency doubling). It is transparent for wavelengths between 350 and 5200 nm. It is birefringent (characterised by two refractive indexes) and it has excellent acousto-, thermo- and electro-optic properties.

Depending on the cut of the crystal the light experiences different refractive indices and electro-optic coefficients. In the case of a z-cut (optical axis parallel to the direction of the light propagation), the propagating light experiences the extraordinary index that is 2.21 at a wavelength of 633 nm. By applying an electric field between the two x-faces of the crystal the light experiences the r_{22} electro-optic coefficient, which has a value $6.7 \times 10^{-12}\mathrm{mV}^{-1}$. In the case of a x-cut (optical axis of the material perpendicular to the direction of the light propagation), the propagating light experiences the ordinary index that is 2.30 at a wavelength of 633 nm. In this case, by applying an electric field between the two z-faces of the crystal the propagating light experiences the r_{13} electro-optic coefficient, which has a value $8.6 \times 10^{-12}\mathrm{mV}^{-1}$.

LN is a ferroelectric material. Through periodic inversion of its ferroelectric domains it is possible to design periodic nanostructures and to build devices able to double the optical frequency of the light. The interest in using LN to build a SPR sensor comes from its excellent properties, useful to implement novel optical sensor configurations. First, its electro-optic properties may allow for a fine tuning of its refractive index and the corresponding sensing characteristics by simply applying potential difference between two faces of the crystal. Recently, an electro-optically modulated SPR sensor has been demonstrated, providing a high signal-to-noise-ratio by an approach of modulation/demodulation of the refractive index of the waveguide [45]. Second, the opportunity to engineer the ferroelectric domains by the poling technique may allow to produce novel and more sensitive sensors [46]. Last but not least, LN is an excellent material for manufacturing optical waveguides. By proton exchange (technique described in detail in Section 1.3.2), it is possible to fabricate TM only waveguides and to avoid the use of an external polarization control [40].

1.3.2 Proton exchange optical waveguides

The optical waveguides considered in the design of the SPR sensor are waveguides produced on LN by the technique of the proton exchange (PE) [40]. A photolithographically defined mask is deposited on the sample in order to expose to the proton exchange only the desired region of the channel. Next, the sample is immersed in a melt mixture of benzoic acid with a certain percentage of lithium benzoate and brought at temperatures as high as 300 °C for periods of few days. During this time the H^+ ions present in the mixture replace the Li^+ ions present in the surface of the exposed region of the channel (proton exchange). The refractive index of the region of the channel increase at the surface as an effect of the proton exchange and it is able to guide an input light wave.

Figure 1.3 (a) presents a schematic view of a typical waveguide used in the numerical simulations. This waveguide has been designed in order to be single-mode and with low losses. A 3D plot of a typical profile of the refractive index n_{wg} (at 633 nm) of such a channel waveguide is presented in Fig. 1.3 (c). The total increase of the refractive index between the LN waveguide and the LN bulk ($\Delta \mathrm{n}_{wg}$) is about 0.0145. The waveguide is 10 μm wide and about 7 μm deep, in order to guide a single TM mode. Such a waveguide can be produced by a PE process of 4 days at 300 °C in a melt mixture of benzoic acid with a 3% lithium benzoate (α-phase) as a proton source. The corresponding profile of the guided mode is presented in Fig. 1.3 (b).

1.3.3 Simulation tools

The tools used to perform numerical simulations of the SPR sensor are Fimmwave and Fimmprop by PhotonD. Two examples of the graphical interfaces of Fimmwave and Fimmprop are presented in Fig. 1.4 (a) and Fig. 1.4 (b), respectively.

Fimmwave is a fully vectorial waveguide solver based on the film mode matching method due to Sudbo [47–50]. According to this method a structure is modeled by a sandwich of n slices of uniform refractive index. For each slice the vectorial mode solver finds any horizontal or vertical mode order of arbitrary or mixed polarisation. Next, the guided modes are calculated by matching the field distributions at the slice

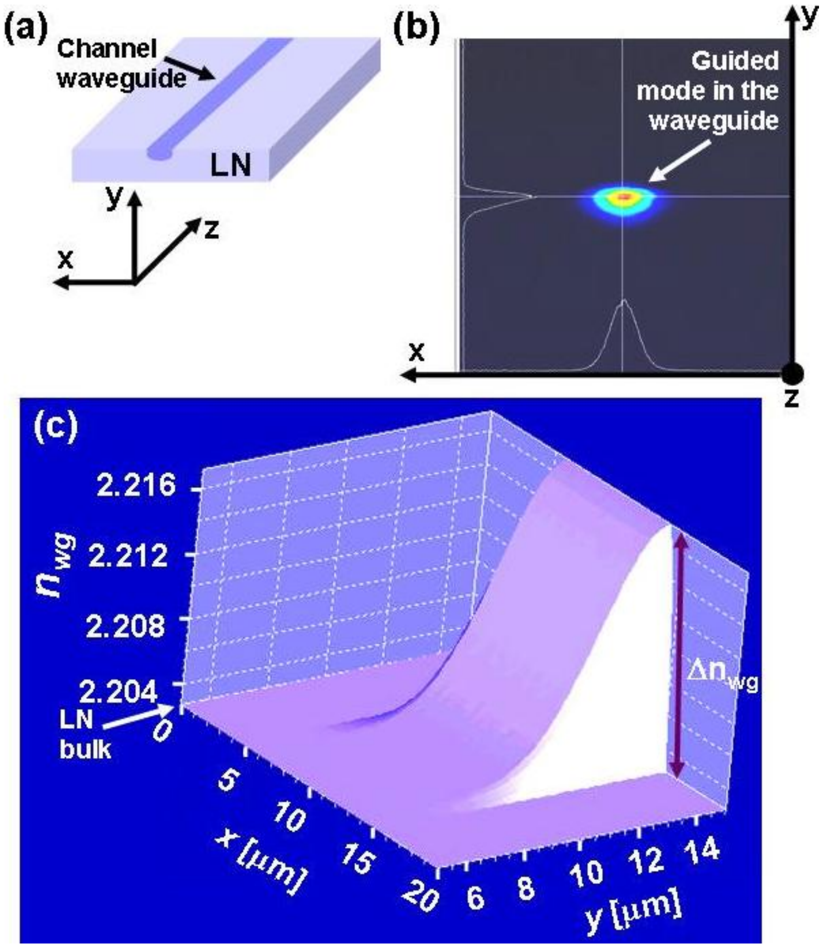

Figure 1.3: Typical waveguide used in the numerical simulations and produced by proton exchange: (a) schematic view of the channel region presenting an higher refractive index; (b) profile of the guided mode; (c) 3D plot of the profile of the refractive index of the waveguide n_{wg} (at 633 nm) along the axis x and y. The waveguide is a 10 μm large LN channel waveguide produced by an α-phase PE process of 4 days at 300 °C.

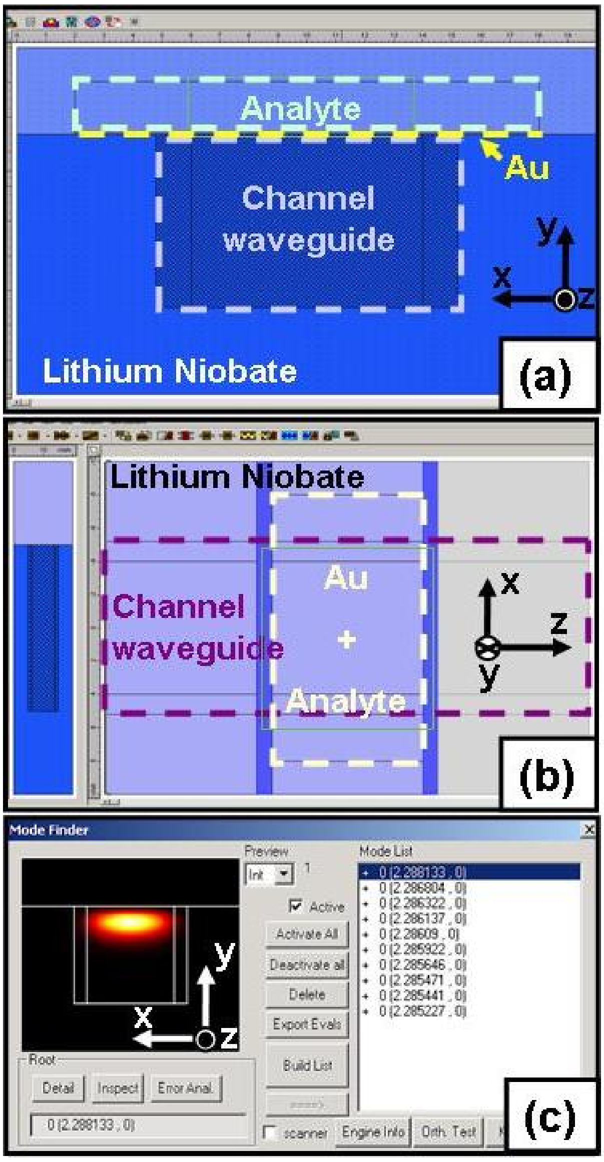

```
0 (2.288133 , 0)
0 (2.286804 , 0)
0 (2.286322 , 0)
0 (2.286137 , 0)
0 (2.28609 , 0)
0 (2.285922 , 0)
0 (2.285646 , 0)
0 (2.285471 , 0)
0 (2.285441 , 0)
0 (2.285227 , 0)
```

```
0 (2.288133 , 0)
```

Figure 1.4: (a) Graphical interface of Fimmwave, showing a cross section of a typical simulated waveguide; (b) graphical interface of Fimmprop, showing a top view of a typical simulated waveguide; (c) window showing the results of the mode solver of Fimmwave; on the left of the window it is possible to see a cross section view of the profile of the guided mode.

interfaces and building coupling matrices between different local modes. The method is generally faster and more accurate than finite element or finite difference methods.

Fimmprop is a 3D bi-directional optical propagation tool integrated with Fimmwave. It simulates the propagation along 3D structures by modelling them as a series of lengths of waveguides (each of uniform cross-section). This approach is advantageous when compared to the algorithm of the beam propagation method. In the latter the propagation mode is solved only for a given optical input profile, while in Fimmprop the propagation mode is solved for all profiles simultaneously.

Two examples of the graphical interfaces of Fimmwave and Fimmprop are shown in Fig. 1.4 (a) and Fig. 1.4 (b), respectively. In particular, Fig. 1.4 (a) shows a cross section view of a typical simulated waveguide as defined in Fimmwave, while Fig. 1.4 (b) shows a top view of a typical simulated waveguide as defined in Fimmprop. The regions of the LN channel waveguide, the Au layer and the analyte layer are highlighted by dashed lines in the images. More details of the simulated waveguides are presented in the following Section 1.4.1. Figure 1.4 (c) shows an example of the results of the mode solver of Fimmwave, including a cross section view of the profile of the guided mode.

1.4 Results and Discussion

1.4.1 Surface plasmon resonance sensor on a lithium niobate proton exchange channel waveguide

In Fig. 1.5 (a) we present the first type of SPR sensor modeled by the module Fimmwave+Fimmprop. It consists of a 10 μm wide and 3 μm deep LN channel waveguide with a total increase of the refractive index of about 0.0145 (see Fig. 1.3 (a)). The typical dimensions of a sample of lithium niobate are 1 cm (width) × 2 cm (length) × 500 μm (thickness). In Fig. 1.5 (b) we present in more detail the sensing window. It consists of a gold film of thickness d_{Au} and length l_{Au} with on top the analyte layer. On top and all around the sensor we assume to have air. The cross section and the top view of such a sensor, as defined in Fimmwave and Fimmprop, respectively, have been shown in Fig. 1.4 (a) and Fig. 1.4 (b), respectively.

The choice of the metal for SPR sensing is critical. The metal must in fact have conduction band electrons capable to resonate with light at a suitable wavelength [5]. As such, its permittivity must have

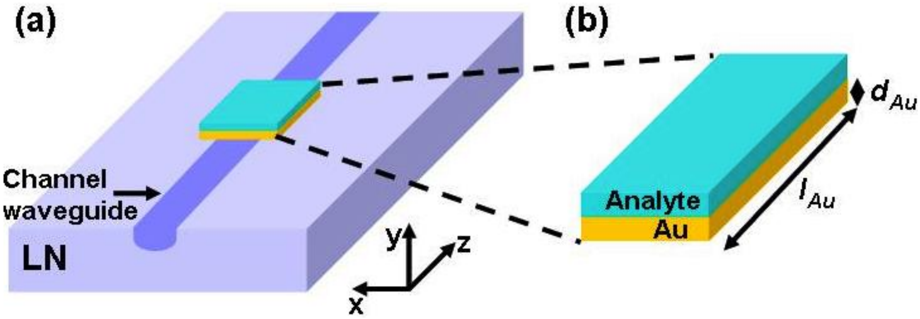

Figure 1.5: (a) SPR sensor studied by numerical simulations. It consists of a 10 μm wide and 3 μm deep LN channel waveguide with a total increase of the refractive index of about 0.0145, as in Fig. 1.3 (c). The sensing window is zoomed in (b). It consists of a gold film of thickness d_{Au} and length l_{Au} with on top the material to analyse (analyte). On top and all around the sensor we assume to have air.

a negative real part and a positive and very small imaginary part, to keep damping to a minimum. This can be concluded from the matching condition in Eq. 1.2 that can be satisfied only if $\mathrm{Re}(\epsilon_m) < -\epsilon_{analyte}$, where $\epsilon_{analyte} = \epsilon_d$. Both silver and gold satisfy this condition. However, gold is preferred for its high degree of stability. It can be exposed to different analytes without suffering of degradation and oxidation. The optical parameters of gold are taken from Ref [51].

In order to study and optimise the SPR response of the sensor, the design parameters such as crystal cut, wavelength of the incident light, thickness and length of the gold film are varied. Note that the results described in the following refer to the fundamental mode of the waveguide since the contributions from the higher modes are found to be negligible.

Either intensity or wavelength interrogations are proposed in Section 1.4.2 and Section 1.4.3, respectively. In the case of intensity interrogation the accuracy of the measurement is deteriorated by any noise or intensity drift [45]. However, this problem can be solved by using particular waveguide configurations such as the y-waveguide discussed in Section 1.6.1. On the other hand, in the case of wavelength interrogation a more complex set-up is required. In particular, a broadband light source and a spectrometer with high resolution are necessary to carry out the sensing measurement with good sensitivity [45].

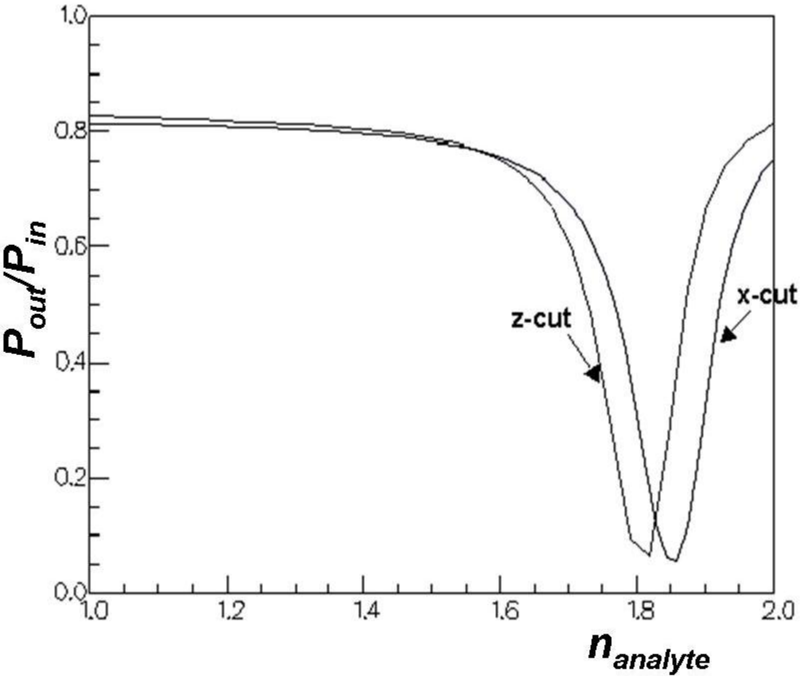

Figure 1.6: Normalised output power P_{out}/P_{in} versus analyte refractive index ($n_{analyte}$) in the SPR sensor schematised in Fig. 1.5 for different LN crystal cut. $\lambda = 633$ nm; $d_{Au} = 50$ nm; $l_{Au} = 2$ mm

1.4.2 Intensity interrogation

In Fig. 1.6 we plot the intensity of the output power (P_{out}) normalised with respect to the intensity of the input power (P_{in}) as a function of the analyte refractive index for LN x- and z-cut. The wavelength of the incident light is 633 nm (He-Ne laser) and the thickness and the length of the gold film are 50 nm and 2 mm, respectively.

For the same conditions of wavelength of the incident light and geometrical parameters of the gold film, the resonance dip is observed at an analyte refractive index (resonance index) of 1.8 and 1.85 for z-cut and x-cut LN waveguides, respectively. In x-cut LN waveguides the refractive index experienced by the input wave is the ordinary refractive index (2.21 at 633 nm, see Section 1.3.1), i.e. lower than the extraordinary refractive index experienced by the input wave in the case of z-cut LN waveguides (2.30 at 633 nm, see Section 1.3.1). From this result we can infer that the resonance index is strongly dependent on the refractive index of the waveguide, since a change of 0.09 in refractive index of the waveguide causes a change of 0.05 of the resonance refractive index.

In Fig. 1.7 we plot the intensity of the output power (P_{out}) normalised with respect to the intensity of the input power (P_{in}) as a function of the analyte refractive index for different wavelengths of the incident light. The thickness and the length of the gold film are 50 nm and 2 mm, respectively. The crystal is z-cut.

Note that different types of lasers are required to introduce the different wavelengths into the waveguide:

- 400 nm (blue-violet range): gas-ion lasers such as Krypton and HeCd lasers;
- 500 nm (green): gas-ion lasers such as Ar lasers;
- 633 nm (red): gas laser He-Ne lasers;
- 750-850 nm (near infrared): solid-state lasers such as Ti:sapphire lasers.

Wavelengths in the range of 400-500 nm do not generate any SPR event, while from 633 nm on the resonance index increases with the wavelength of the incident light. The SPR curve becomes narrower and deeper with a corresponding increase of the sensor sensitivity.

The penetration length of the evanescent field that generates SPR increases with increasing wavelength. Longer wavelengths, i.e. near infrared, can penetrate deeper into the analyte, corresponding to an improvement of sensitivity. However, since most of the reactions that involve a change of the analyte refractive index happen at the sensor surface, we may expect similar sensitivities for wavelengths above 633 nm. Since we want to move to lower refractive indices we choose 633 nm as wavelength of the incident light.

We now move to the design related to the sensing window. In Fig. 1.8 we plot the intensity of the output power (P_{out}) normalised with respect to the intensity of the input power (P_{in}) as a function of the analyte refractive index for different thicknesses (Fig. 1.8 (a)) and lengths (Fig. 1.8 (b)). The wavelength is 633 nm, the crystal is z-cut; for the simulations in Fig. 1.8 (a) the length of the gold film is 2 mm; for the simulations in Fig. 1.8 (b) the thickness of the gold film is 50 nm.

By reducing the thickness of the gold film the resonance index increases and the SPR curve becomes wider and less selective. On the

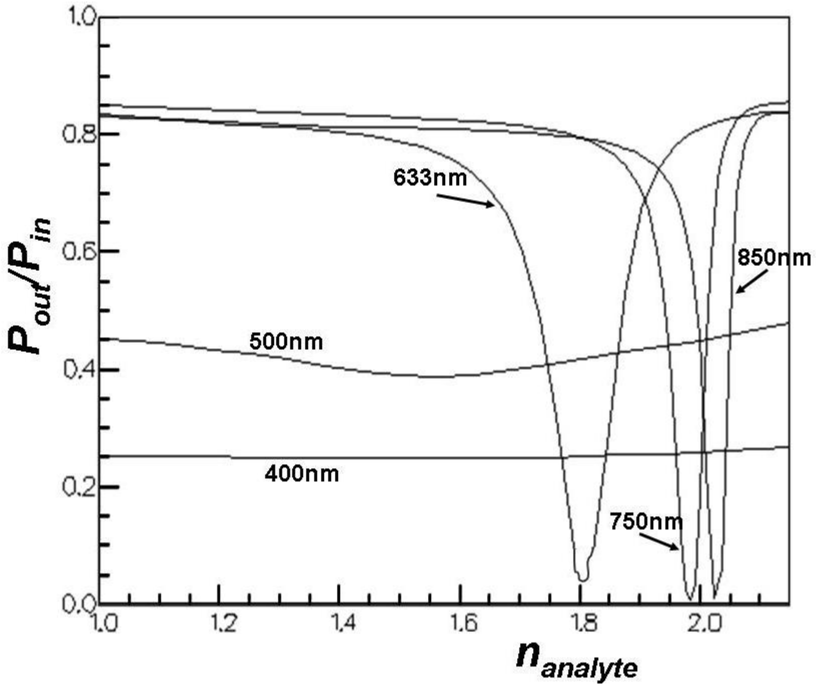

Figure 1.7: Normalised output power P_{out}/P_{in} versus analyte refractive index ($n_{analyte}$) at different wavelengths of the input light. LN-cut = z-cut; d_{Au} = 50 nm; l_{Au} = 2 mm

other hand, if the thickness of the gold film goes above 50 nm, the value of P_{out}/P_{in} increases, thus reducing the index range that is possible to discriminate. Therefore, the best thickness turns out to be 50 nm. By increasing the length of the gold film, the SPR curve spreads out, but the resonance analyte index remains the same. For our applications an interaction length of 2 mm is a good choice. Note that a layer of chromium (Cr) of small thickness (typically between 4 and 7 nm) in between the gold layer and the LN waveguide is required to achieve a good adhesion of gold on top of lithium niobate. Numerical simulations taking into account the presence of such a layer revealed only a slight change of the results described above and they are omitted here.

1.4.3 Wavelength interrogation

In this Section we investigate the alternative of the wavelength interrogation. In Fig. 1.9 we plot the intensity of the output power (P_{out})

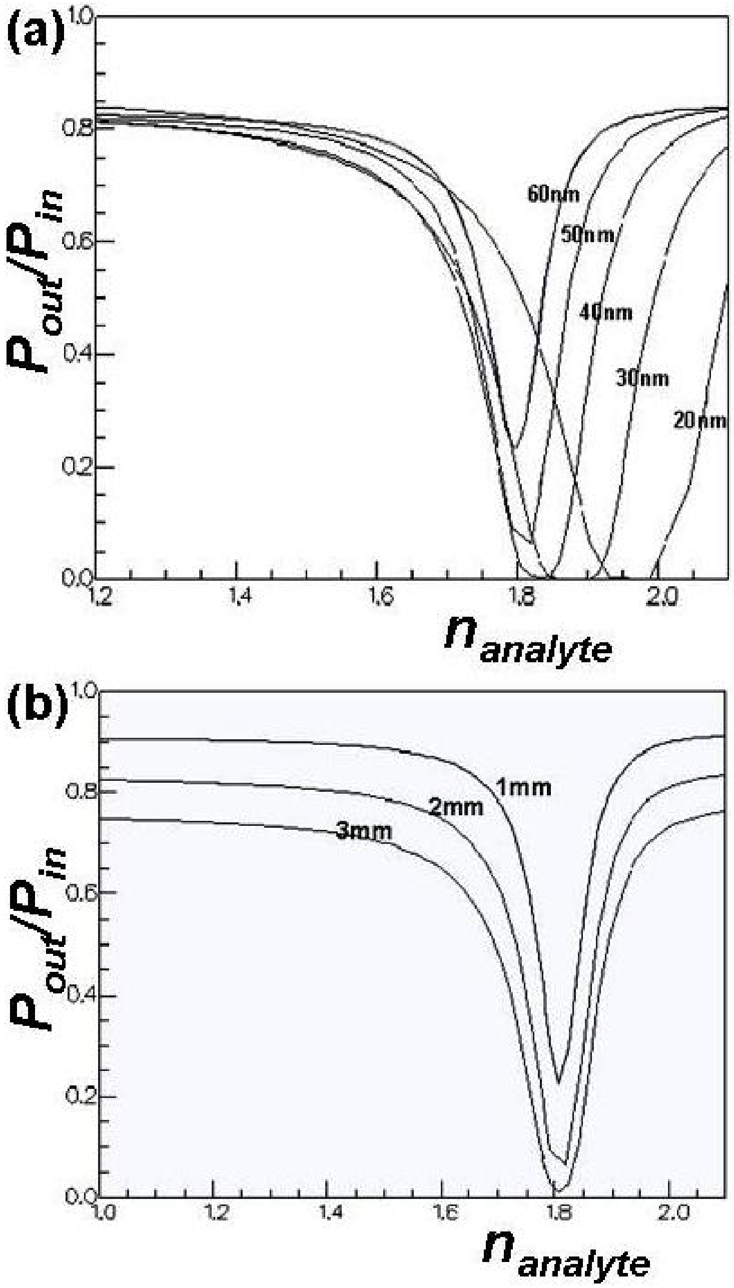

Figure 1.8: (a) Normalised output power P_{out}/P_{in} versus analyte refractive index ($n_{analyte}$) for different thickness of the gold film. LN-cut = z-cut; $\lambda = 633$ nm; $l_{Au} = 2$ mm. (b) Normalised output power P_{out}/P_{in} versus analyte refractive index ($n_{analyte}$) for different length of the gold film. LN-cut = z-cut; $\lambda = 633$ nm; $d_{Au} = 50$ nm

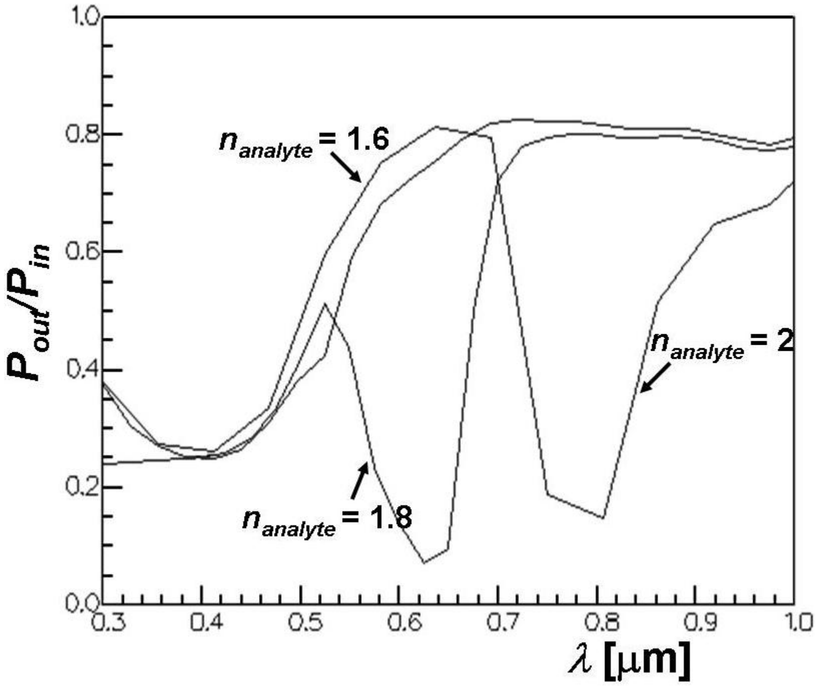

Figure 1.9: Normalised output power P_{out}/P_{in} versus wavelength of the input light (λ) for different analyte refractive index ($n_{analyte}$). LN-cut = z-cut; λ = 633 nm; l_{Au} = 2 mm. The curves appear not continuous because only few data points have been calculated in this case.

normalised with respect to the intensity of the input power (P_{in}) as a function of the wavelength of the input light. Analyte refractive indices of 2, 1.8 and 1.6 are considered.

Only analyte refractive indices in the range of the refractive index of the waveguide generate SPR. For a refractive index below or equal to 1.6 no SPR events are recorded. The SPR curves are broad and not selective when compared to the case of intensity interrogation. Moreover, the setup for wavelength interrogation is more complex since a broadband light source and a spectrum analyser are required to carry out the measurement. As such, the configuration of intensity interrogation is the most convenient and will be taken into account in the following.

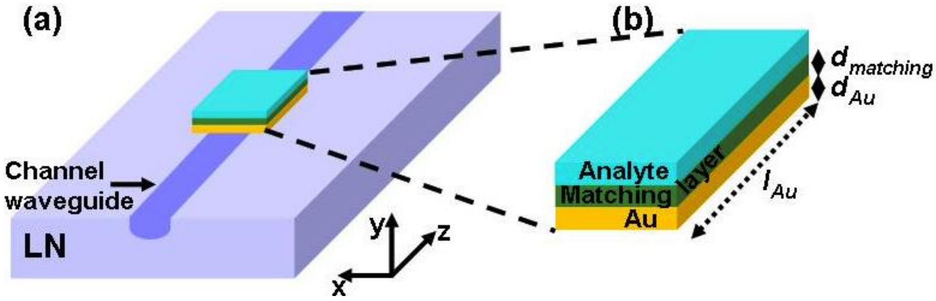

Figure 1.10: (a) SPR sensor with the matching layer between the gold layer and the analyte. It consists of a 10 μm wide and 3 μm deep LN channel waveguide with a total increase of the refractive index of about 0.0145, as illustrated in Fig. 1.3 (c). A zoom-in of the sensing window is shown in (b). It consists of a gold film of thickness d_{Au} and length l_{Au} with on top the matching layer of thickness $d_{matching}$ and the material to analyse (analyte).

1.4.4 Matching layer for surface plasmon resonance tuning

In order to tune the SPR curve in order to analyse different materials and, in particular, aqueous solutions (refractive index of 1.33 at a wavelength of 633 nm), a layer of thickness $d_{matching}$ is added to the previous structure between the gold layer and the analyte, as illustrated in Fig. 1.10. In the following we refer to this extra layer as the matching layer. The introduction of the matching layer allows for tuning of the resonance refractive index because the evanescent field of the plasmon wave penetrates into both the matching layer and the analyte. As such, it is able to sense a suitable index corresponding to a mean value between the refractive index of the matching layer and the refractive index of the analyte.

In order to tune the resonance towards the refractive index of the analyte of interest, while keeping a good sensitivity, we need to properly choose the refractive index and the thickness of the matching layer. By carrying out numerical simulations with different refractive index of the matching layer we observe that with matching layers of refractive index in the range of or lower than the refractive index of the waveguide (2.2100 + 0.0145 in our case) the resonance can be shifted towards lower or higher analyte refractive index, respectively, when compared to the resonance without matching layer. If the refractive index of the

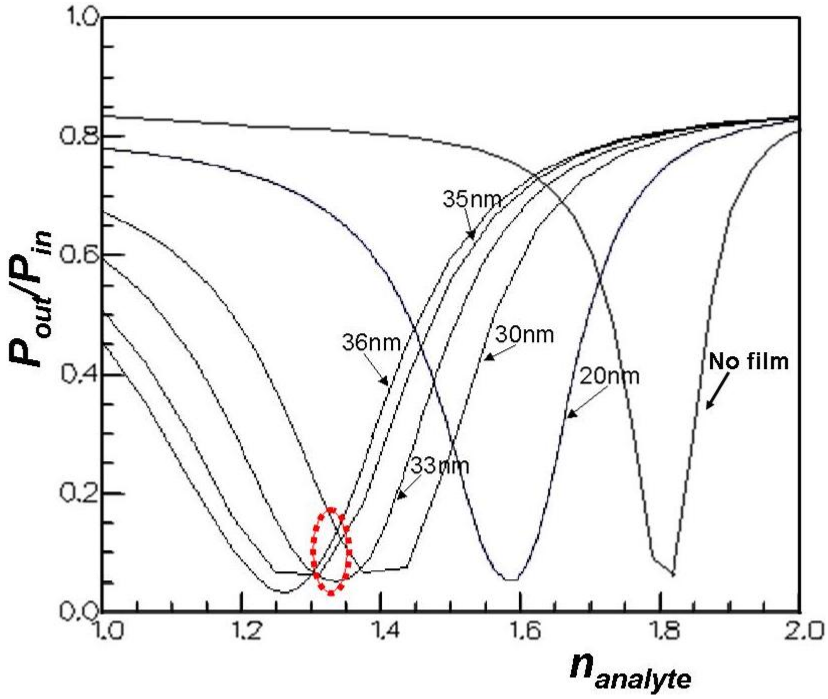

Figure 1.11: Normalised output power P_{out}/P_{in} versus analyte refractive index ($n_{analyte}$) with different thickness of the matching layer $d_{matching}$. LN-cut = z-cut; λ = 633 nm; l_{Au} = 2 mm; d_{Au} = 50 nm. The part of the curve that enables the analysis of aqueous solutions is highlighted by a dotted oval.

matching layer is higher than the refractive index of the waveguide the matching layer becomes the new waveguide and the SPR phenomenon does not occur. To reduce the resonance index we need then to introduce a matching layer with high refractive index but not higher than the refractive index of the waveguide. We then choose a refractive index of the matching layer of 2.2 (suitable materials could be sputtered LN, rutile or some polymers).

In Fig. 1.11 we plot the intensity of the output power (P_{out}) normalised with respect to the intensity of the input power (P_{in}) as a function of the analyte refractive index for different thickness $d_{matching}$ of the matching layer. The refractive index of the matching layer is 2.2. The wavelength of the incident light is 633 nm (He-Ne laser) and the thickness and the length of the gold film are 50 nm and 2 mm, respectively.

A 20 nm thick matching layer already lowers the resonance analyte refractive index to 1.6. By increasing the thickness of the matching layer the resonance is shifted towards lower refractive index but the SPR curves widen and loose sensitivity. However, a 36 nm thick matching layer turns out to allow the analysis of aqueous solutions since the resonance happens at refractive index of 1.3. The part of the resonance curve, which is useful for such analysis, is highlighted by a dotted oval in Fig. 1.11.

If the matching layer is too thick, the SPR curve is not much selective, because the evanescent field fraction that is able to sense the variation of the analyte refractive index is too small. The profile of the magnetic field H for a waveguide with a 36 nm thick matching layer of refractive index 2.2 is shown in Fig. 1.12 (a-b). This is the magnetic field of the first mode guided in the waveguide of Fig. 1.10 at a wavelength of 633 nm, with a gold layer having a thickness of 50 nm and a length of 2 mm. The zoomed view of the region highlighted by a dotted oval in Fig. 1.12 (a) is presented in Fig. 1.12 (b). It shows how the field penetrates into the different layers of the structure, sensing an average refractive index between the refractive index of the analyte and the refractive index of the matching layer. From the image it is clear that the evanescent field that enters into the analyte is only a small fraction of the total evanescent field, that enters into both the matching layer and the analyte. For this reason the sensitivity of the sensor is lower when compared to the sensor without the matching layer.

1.5 Conclusions

In this chapter we proposed a novel SPR sensor built on LN optical waveguides. This sensor was studied and designed by numerical simulations with a module consisting of a mode-matching solver (Fimmwave) and a 3D coupling matrices propagator (Fimmprop).

Our results reveal that the resonance analyte refractive index is always between 1.8 and 2 when we vary some of the design parameters such as LN-cut, wavelength, gold film thickness and length.

The minimum resonance index with a good sensitivity of the sensor is achieved with a wavelength of 633 nm on a LN z-cut PE waveguide with a 50 nm thick and 2 mm long gold film. The resonance index is in this case around 1.8 implying it can be useful to analyse high index oxides or polymer films, but not for aqueous solutions.

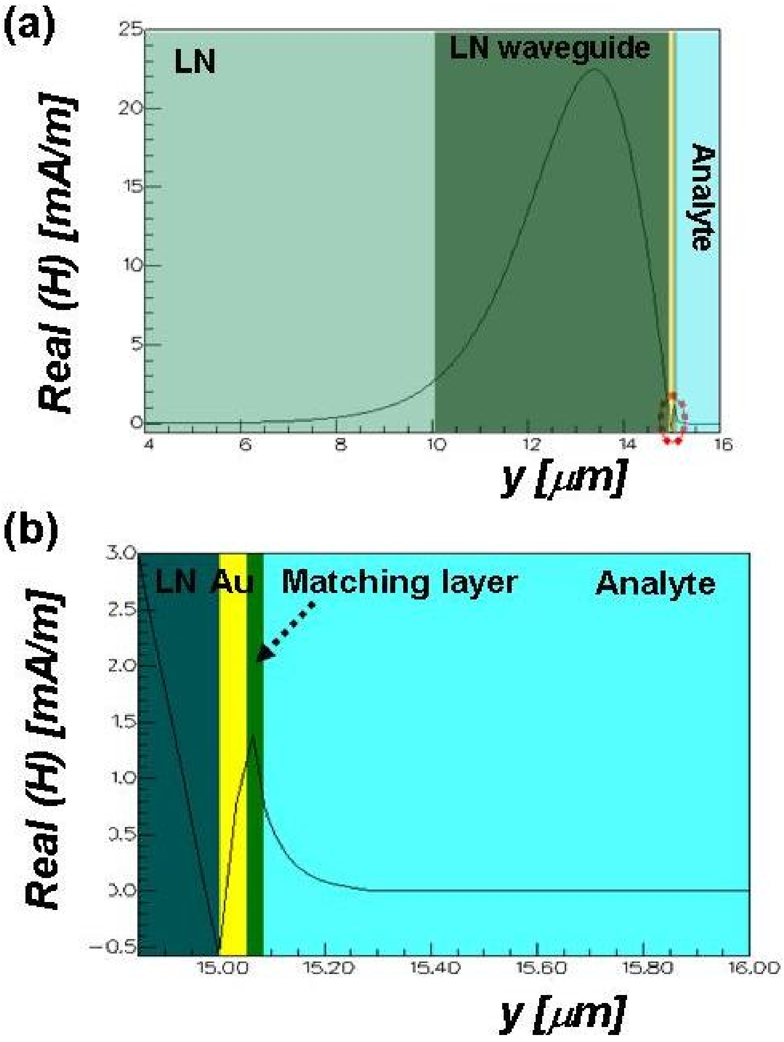

Figure 1.12: (a) Magnetic field intensity H of the fundamental mode of the SPR waveguide with a matching layer having a thickness of 36 nm and a refractive index of 2.2. (b) Zoomed view of the region highlighted by a dotted oval in (a), where the evanescent field of the SPR wave enters into the matching layer and the analyte.

The introduction of a matching layer of suitable thickness and refractive index in between the gold layer and the analyte allows to tune the resonance analyte refractive index. In particular, a resonance refractive index of 1.3 can be achieved with a matching layer with a thickness of 36 nm and a refractive index of 2.2. The resulting sensor loses sensitivity because the evanescent field which is able to enter into the analyte is only a small fraction of the entire evanescent field. However, this sensor is now able to analyse aqueous solutions. This result can be generalised to SPR optical waveguides based on any material. In general it demonstrates that it is always possible to tune the resonance index towards the desired values by adding a matching layer with appropriate thickness and refractive index on top of the metal film. Note that the variation of the SPR curve with the thickness of the metal film and the matching layer indicates another possible application of this sensor, i.e. as monitor of the thickness or the adsorption of thin films on the sensing surface.

The results shown in this chapter are theoretical results. However, they are based on some data obtained from the literature (e.g. the optical parameters of the gold) and some experimental data obtained from previous work carried out in the same group (e.g. data on the PE waveguides). A similar sensor built on a glass substrate, i.e. that does not require the matching layer to sense aqueous solutions, has been experimentally tested by another PhD student from the same group and the results of this work has been published in [52].

1.6 Outlook

In this outlook section we present some preliminary results about the design of SPR sensors based on y-waveguides and we propose some future work to further improve the SPR sensitivity.

1.6.1 Y-waveguides for surface plasmon resonance sensing

SPR sensors arranged on y-waveguides would allow to soften the requirements concerning the laser source stability. Figure 1.13 (a) shows a channel waveguide arranged according to a y-junction optical circuit. The device consists of a substrate of lithium niobate where the y-waveguide can be defined by standard optical lithography combined with the process of proton exchange described in Section 1.3.2. The difference with the waveguide described in the chapter is that in this configuration only one branch is covered by the sensing window (metal layer and analyte) to induce surface plasmon resonance. The other branch is used as reference. The advantage of such a configuration is that it allows to soften the requirements concerning the laser source stability. It in fact makes it possible to do real time measurements of the ratio between the reference output power ($P_{OUT_{ref}}$) and the SPR output power ($P_{OUT_{spr}}$). This way, the common intensity fluctuations due to low stability of the laser source can be excluded.

The design of the y-waveguide involves an accurate design of the opening angle between the two branches of the waveguide in order to not have high losses. Figures 1.13 (b-c) show some first results concerning the design of low losses y-waveguides. In particular, Fig. 1.13 (b) shows an example of Y-waveguide with high losses, while Fig. 1.13 (c) shows an example of Y-waveguide with low losses.

1.6.2 Improvement of the SPR sensitivity

Recently, different configurations have been proposed in order to improve the sensitivity of SPR sensors. As mentioned in the course of the chapter, electro-optically modulated sensors allow to reduce the signal-to-noise ratio and to improve the sensitivity of the sensor [45, 53–55]. Of particular interest are also the ridge waveguides [56] and the waveguides with metal particles instead of the metal layer in the sensing window [57]. In both approaches the sensitivity increases due to an increase of the sensitive surface, i.e. the ridge structure of the waveguide or the curvature of the particles. As future work we suggest to investigate such approaches in order to further improve the sensitivity of the sensors discussed in this chapter.

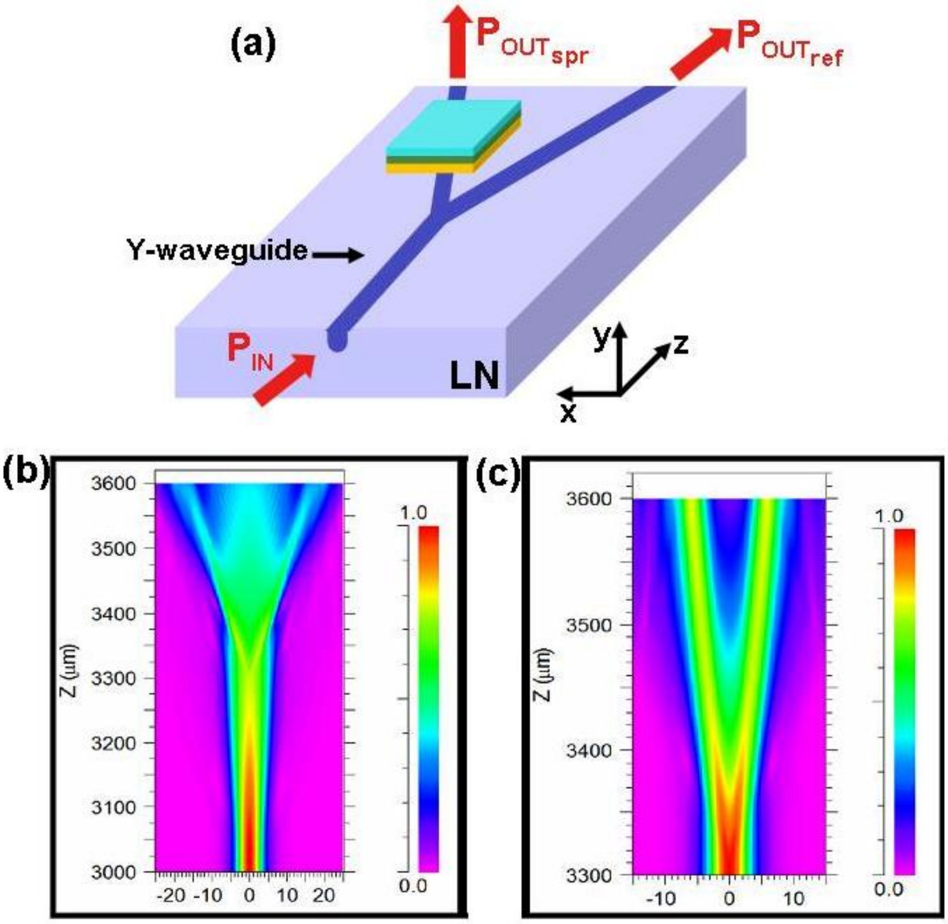

Figure 1.13: (a) Schematic of a SPR sensor arranged on a y-waveguide. One branch is covered by the sensing window (metal layer and analyte) to induce surface plasmon resonance. The related output power is named $P_{OUT_{spr}}$. The other branch is used as reference and the related output power is named $P_{OUT_{ref}}$. (b-c) Examples of y-waveguides with (b) high and (c) low losses.

Part II

Carbon Nanotube Interconnects as Candidates for Sensor Applications

Chapter 2

Growth of Carbon Nanotube Horizontal Interconnects

2.1 Introduction

Carbon nanotubes (CNTs) are extraordinary materials for interconnects and sensing applications [12, 19, 58]. This is due to their unique set of properties, including ballistic charge transport [13], high current-carrying capacity [14], high thermal conductivity [16], high Young modulus [15] and sensitivity to the surrounding environment [59]. In practice, only arc-discharge produced CNTs have the expected extraordinary properties, while CNTs grown by CVD contain many structural defects and behave as diffusive conductors rather than as ballistic conductors [60]. Despite their defective nature, CVD-grown CNTs are more suitable for applications as they can be integrated into silicon based devices by depositing catalyst particles at predefined locations [20]. CVD allows for growth of vertically oriented CNTs using catalyst deposited on planar and patterned substrates [19, 58, 61, 62]. On the other hand, control over horizontal growth is much more challenging. Horizontal CNTs are essential not only for interconnects [19] and sensing applications [59, 63], but also to fabricate transistors [12], memories [64] and nanoelectromechanical systems (NEMS) [65].

One approach to grow CNTs horizontally is to place the catalyst on the sidewalls of vertical structures. This can be done by traditional catalyst deposition methods such as physical vapor deposition (PVD), sputtering or evaporation [58], spincasting [66], and printing [67] or by using sandwich-like structures incorporating either catalyst [8, 68, 69] or silica layers [70, 71]. In the latter case the catalyst is generated in a gas flow of a ferrocene-xylene mixture. Alternatively, horizontal CNTs can be obtained by guiding the growth direction with electric fields [72–77], magnetic fields [78] or gas flow [79–85]. There are mixed opinions about the efficacy of horizontal alignment controlled by a gas flow. For example, Reina *et al.* [82] showed that it was not successful for CNTs shorter than 50 μm. Huang *et al.* [84] demonstrated the need to make CNTs grow away from the substrate at the nucleation stage to be able to control their growth by the gas flow. This was obtained by heating the substrate up to temperatures as high as 900 °C over a short period at the very initial CNT growth stage ("fast-heating" technique). Jin *et al.* [85] showed that low gas flow rates are sufficient to grow horizontally-aligned ultra-long single-walled CNTs (SWNTs). Recently, it was shown that the CNT growth direction can be guided by grooves on SiO_2 substrates [86, 87] or along certain crystallographic directions on quartz substrates [88–90]. Finally and of particular interest for horizontal CNT integration in microelectronics, Hayamizu *et al.* [91] developed a novel post-growth method of transforming vertical SWNT arrays into horizontal arrays, which could then be further patterned to build different devices.

All the techniques described above allow for a good control over CNT placement and growth direction. However, traditional catalyst deposition methods lack selectivity and require further steps to isolate the catalyst at specific locations [58, 66, 67]. Techniques based on sandwich-like structures require agglomeration of the sandwiched catalyst layer with possible damage of the structures [8, 68, 69]. In case of in-situ generated catalyst in the gas flow, silica substrates provide selectivity but are not electrically conductive and thus need to be contacted somehow after growth for electrical characterization [70, 71]. Methods based on forced CNT alignment during-growth [72–85] still need catalyst placement by, e.g., lithography. As a consequence both the catalyst placement and the growth process add degrees of complexity to the device fabrication. Guiding the CNT growth direction by crystallographic orientation [88–90] or patterned substrates [86, 87] obviously only allows to grow in plane CNTs and it is not possible to grow suspended CNTs, which are required for applications such as NEMS devices and are also more advantageous as sensors due to the increase of the sensing area.

This chapter describes a novel growth technique that allows to grow horizontally suspended CNTs connecting metal electrodes. The technique relies on the selective placement of the Ni catalyst nanoparticles on the electrode sidewalls by electrochemical deposition (ECD). Electrochemically deposited catalysts have already been shown to be effective for CNT growth in combination with templates such as anodised (oxidised) aluminum [92, 93] and mesoporous silica films [94], where the catalyst size is controlled by the pore dimensions. This technique has an intrinsic selective nature, since metal deposition only occurs on (semi)conductive surfaces contacted as the cathode. Therefore, when combined with appropriately designed structures, this technique does not require further processing to remove unwanted metal catalyst, as was demonstrated recently for high density CNTs selectively grown inside vias [20–23]. Moreover, the electrochemical deposition method allows for excellent control of the nanoparticle density and size distribution, translating into a similar control over the CNT density and diameter distribution [20–23]. This approach significantly simplifies the fabrication process when compared to the above discussed techniques, since no additional anneal, no forced CNT growth direction nor post-growth processing are required to obtain electrically contacted horizontally suspended CNTs. Moreover, this technique allows to routinely grow CNTs from opposing electrodes with very low resistance values as it will be discussed in the Chapter 3.

This work was carried out during the second and third year of the PhD research. The growth process was developed in the framework of the European project “CarbonCHIP” at IMEC with partners including Intel Ireland that produced the growth test structures. Part of the results of this work has been published in [95] for the conference ISTC/CSTIC2009 and in [96].

The first part of the chapter (Section 2.2) describes the materials and methods used in this work: the growth test structures in Section 2.2.1, the growth method in Section 2.2.2, the ECD technique for the catalyst deposition in Section 2.2.3, the CVD technique for the CNT growth in Section 2.2.4. The techniques used to analyse as-grown CNTs, i.e. scanning electron microscopy (SEM), transmission electron microscopy (TEM), Raman spectroscopy and energy dispersive X-ray spectroscopy (EDX) are presented in Section 2.2.5. In Section 2.3 we present the results related to the ECD catalyst deposition (Section 2.3.1) and the CNT growth (Section 2.3.2), including all details concerning the Raman, TEM and EDX characterisation. The chapter ends with the conclusions in Section 2.4 and outlook in Section 2.5.

2.2 Materials and Methods

2.2.1 Growth test structures

The growth test structures consist of 200 nm thick and 450 nm wide titanium nitride (TiN) electrodes fabricated on p+ top implanted silicon substrates with a 200 nm thick SiO_2 layer. The distance (electrode gap) between the two opposing electrodes varies between 200 nm and 10 μm. The electrodes are connected to a four-point probe pad configuration as illustrated in Fig. 2.1. Only one (configuration A, Figs. 2.1 (a-b)) or both TiN electrodes (configuration B, Figs. 2.1 (c-d)) are connected to the Si substrate via nickel silicide pads formed on the exposed p+ Si substrate as shown in the cross-sectional view of the test structures in Figs. 2.1 (a-c). To allow the electrical characterisation of the CNT interconnects, one of the electrodes in configuration B can be disconnected from the substrate by cutting the "scribe line" shown in Figs. 2.1 (c-d). An electrically insulating 30 nm thick silicon oxynitride (SiON) hard mask covers the top of the electrodes, exposing only the TiN electrode sidewalls during the ECD of the Ni catalyst nanoparticles.

2.2.2 Growth method

The method proposed to grow the CNT interconnects is schematically presented in Fig. 2.2 (a) and Fig. 2.2 (b) for configuration A and B, respectively. The Ni catalyst nanoparticles are deposited by ECD. A Ni^{2+} electrolyte solution is in contact with the top of the sample and either a constant voltage or a constant current are applied for a certain time between the solution and the substrate (Fig. 2.2 (a.i) and Fig. 2.2 (b.i) for configuration A and B, respectively). As a result, the ions present in the solution reduce to their metallic form of Ni nanoparticles on the sidewalls of the electrodes connected to the substrate: one electrode in configuration A (Fig. 2.2 (a.ii)) and both electrodes in configuration B (Fig. 2.2 (b.ii)). The details of the ECD technique for catalyst deposition are described in Section 2.2.3.

Next, CNTs are grown from the Ni catalyst nanoparticles by CVD. In configuration A CNTs grow from one electrode towards the opposite one (Fig. 2.2 (a.iii)), while in configuration B CNTs grow from both

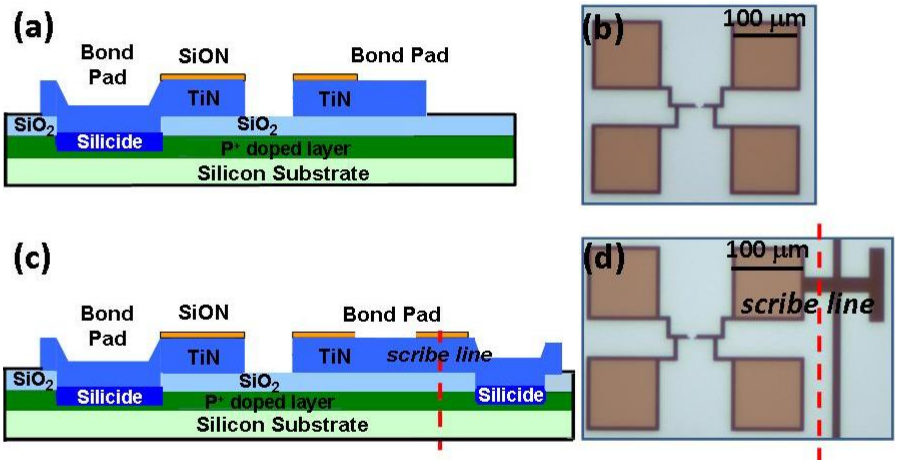

Figure 2.1: Schematic view of the growth test structures (a and c) showing the different layers (Si substrate, p+ implanted layer, 200 nm SiO_2, 200 nm TiN and 30 nm SiON) and optical top-view images (b and d) showing the layout of the 100 μm × 100 μm bond pads connected to the 450 nm wide electrodes in the center. In configuration A (a and b) only one of the TiN electrodes is connected to the Si substrate via a silicide pad. In configuration B (c and d) both TiN electrodes are connected to the Si substrate because the opposite bond pad is connected to an additional TiN/silicide/p+Si contact made through the oxide layer adjacent to the bond pad. This second electrode can be disconnected afterwards for the electrical tests by cutting the “scribe line” as indicated by the dashed line in c and d.

electrodes (Fig. 2.2 (b.iii)). The details of the CVD technique for CNT growth are described in Section 2.2.4.

2.2.3 Electrochemical deposition

Nickel catalyst nanoparticles are electrodeposited on TiN using the setup schematically presented in Fig. 2.3. Electrical contact to the backside of the sample (Si substrate) is made using InGa eutectic and the sample is pressed on a copper plate. A glass tube (O-ring area of 1.43 cm^2) is clamped onto the substrate. The TiN growth test structures are incorporated as working electrode into this small volume (2-3 ml) 3-electrode electrochemical cell together with a small Ag/AgCl/3 M NaCl reference electrode (0.21 V vs. standard hydrogen electrode (SHE)) and a Pt wire

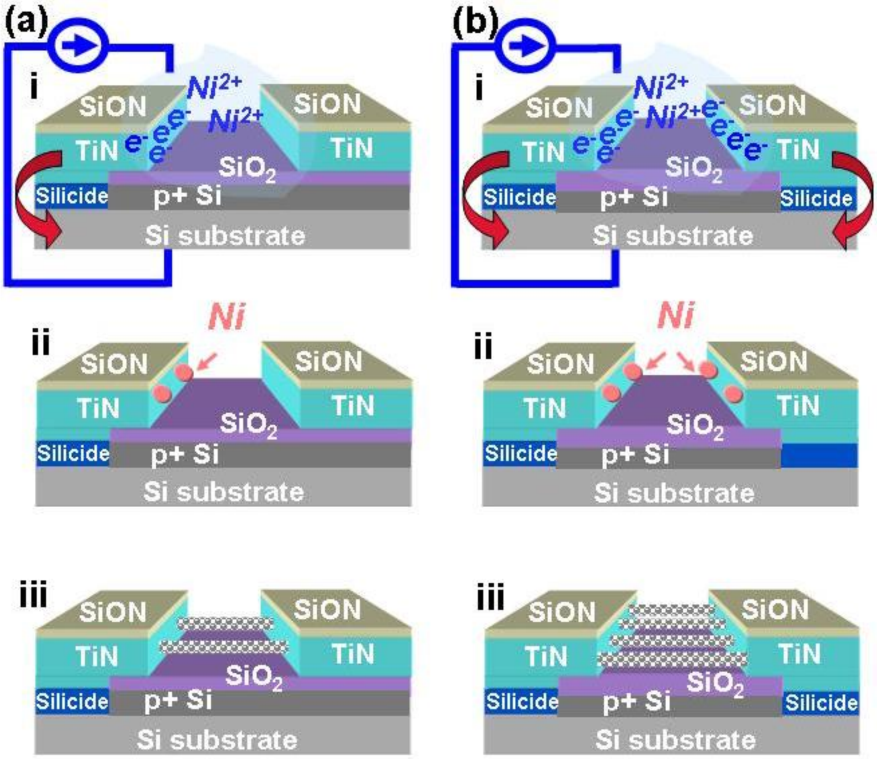

Figure 2.2: Schematic view of the growth method for (a) configuration A (one electrode-substrate connection) and (b) configuration B (two electrode-substrate connections). In (a.i) and (b.i) we illustrate the ECD of the Ni catalyst nanoparticles. A Ni^{2+} electrolyte solution is in contact with the test structures and a certain amount of electric current is forced to flow between the substrate and the electrolyte. In (a.ii) and (b.ii) the ions in the solution reduce to their metallic form of Ni nanoparticles on the sidewalls of the electrodes connected to the substrate: one electrode in configuration A and both electrodes in configuration B. In (a.iii) and in (b.iii) CNTs grow by CVD from the Ni catalyst nanoparticles from one electrode towards the opposing electrode in configuration A and from both opposing electrodes in configuration B.

as counter electrode. The reference electrode is placed into a 1 ml pipet point that works as "Luggin capillary" (it defines a precise sensing point for the reference electrode near the working electrode). The Ni solution is a $Ni(NH_3)_6^{2+}$ electrolyte solution prepared by following a similar procedure to that previously reported in the Refs. [20–23]. It consists of 0.01 M $Ni(NO_3)_2$, 1 M NaCl, and 1 M NH_4Cl with the pH adjusted to 8 by adding small volumes of NH_4OH, turning from green to blue as a result of the formation of the nickel-ammonia complex $Ni(NH_3)_6^{2+}$. Prior to deposition the samples are cleaned with 3 wt.% NH_4OH for 3 minutes to remove any polymer residues, followed by immersion in 0.25 wt.% HF for 1 minute to remove the native surface oxide on TiN. The electrode potential is controlled by a Autolab PGSTAT30 or PGSTAT100 potentiostat (Metrohm-Ecochemie), referred to as "P" in Fig. 2.3, which is operated by GPES software. Cyclic voltammetry measurements are carried out in order to estimate the reduction potential of the electrolyte solution. Either potentiostatic (constant potential of the working electrode with respect to the reference electrode) and galvanostatic (constant current between the working electrode and the counter electrode) methods are used for electrochemical deposition. After electrodeposition the InGa is carefully removed from the backside with cotton swabs soaked in 1.2 M HCl.

2.2.4 Chemical vapor deposition

CNTs are grown from the electrodeposited Ni catalyst nanoparticles by CVD. In a typical experiment sample pieces of 2 × 2 cm^2 are placed in the centre of a 200 mm Si carrier wafer and transferred from a chamber at room temperature and under vacuum condition (10^{-5} Torr) to a plasma enhanced (PE) CVD reactor (Oxford Instruments PECVD). The samples are allowed to adjust to the heater temperature for 1 minute. Next 10/150/600 sccm of $C_2H_2/H_2/Ar$ is allowed to flow into the chamber and stabilized at 4 Torr for periods of up to 1 hour. The substrate temperature is maintained between 620-640 °C as this provides optimum growth conditions. Note that this temperature is less than the set temperature (700 °C) due to the heat loss between the location where the temperature is measured and the sample itself.

A schematic view of the PECVD reactor is shown in Fig. 2.4. The reactor has a top shower gas inject. A radio frequency plasma (13.56 MHz) can be activated between the top and the bottom electrode. A vacuum pump allows to keep the vacuum during the transfer of the

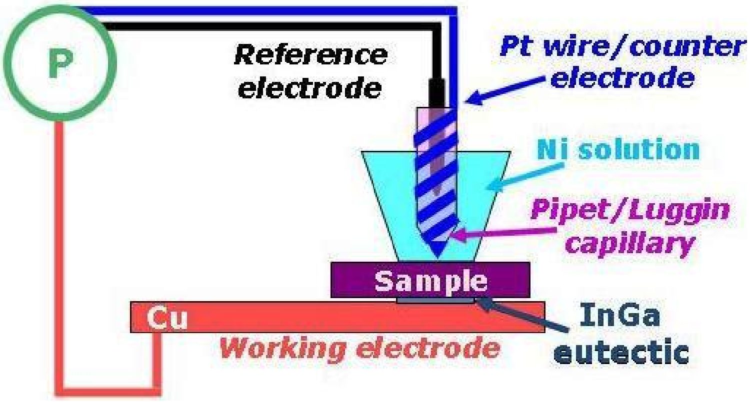

Figure 2.3: Setup for electrochemical deposition: the sample is pressed on a copper plate with InGa eutectic in between to assure a good ohmic contact. A glass tube containing the Ni electrolyte solution is clamped onto the substrate. A Ag/AgCl/3 M NaCl reference electrode and a Pt wire counter electrode are incorporated into this electrochemical cell. The reference electrode is placed into a pipet point that works as "Luggin capillary".

sample into the chamber and before entering the gas. The walls of the chamber are water cooled.

2.2.5 Microscopy and spectroscopy techniques for sample analysis

In this section we present the techniques used to characterise the samples after catalyst particle deposition and CNT growth.

Scanning electron microscopy

In order to image the Ni catalyst nanoparticles after deposition and the CNTs after growth, the samples are examined with scanning electron microscopy (SEM, FEI, NOVA 200) with the possibility to detect secondary electrons. In a typical measurement the accelerating voltage of the electron beam is 6.5 kV with a 3 nm spot size.

Transmission electron microscopy

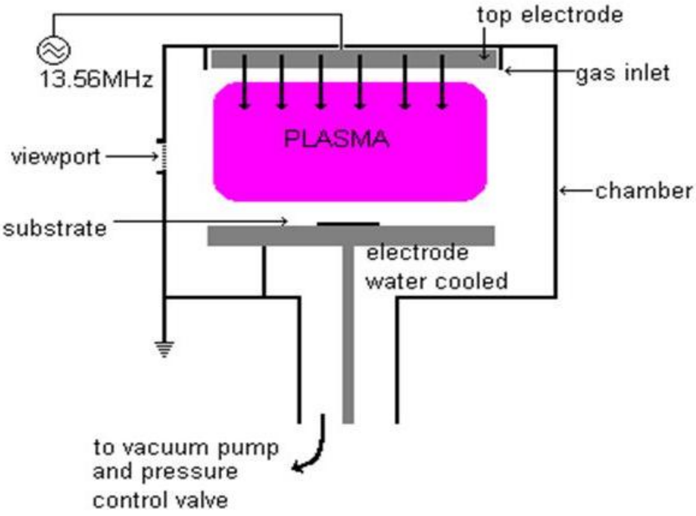

Figure 2.4: Schematic view of the PECVD reactor. The reaction gas enters from the top of the chamber with a shower inject. A radio frequency plasma (13.56 MHz) can be activated between the top and bottom electrodes present in the chamber. The walls of the chamber are water cooled.

In order to investigate the CNT graphitic structure and how the CNTs grow, the samples are examined with transmission electron microscopy (Tecnai F30 ST, FEI) at 200 kV to avoid damaging the CNTs during the TEM observation. A first approach to prepare the sample to the TEM analysis is carried out directly on the growth test structures with CNTs. A first cap layer of glass is grown by low temperature CVD to protect the sample surface from the successive processes. A second cap layer of Platinum (Pt) is deposited by ion-beam on top of the glass layer. Next, the thickness of the specimen is reduced to 10-15 μm by focused ion beam (FIB) lift-out to be then glued on the TEM grid and imaged. A second approach to prepare the sample to the TEM analysis is carried out on CNTs removed from the growth test structures. CNTs are removed from the substrate by 10 minutes sonication in ethanol. Next few droplets of the ethanol solution with CNTs is deposited on the TEM grid for imaging.

Raman spectroscopy

In order to evaluate the quality of the CNTs and the eventual presence of SWNTs, the samples are analysed by Raman spectroscopy. Raman spectra are collected using a multi wavelength spectrometer (Jobin-Yvon Labram HR, 0.3 cm^{-1} resolution). The excitation wavelength is 457.8 nm for a laser output power of 75 mW. The measurement is carried out with an integration time of 1800 s. The analysed spectral range includes the radial breathing mode and the D and G wavelengths.

Energy dispersive spectroscopy

Energy dispersive X-ray spectroscopy (EDX) is carried out in conjunction with SEM in order to analyse the elements present on the growth test structures after catalyst placement and CNT growth. The EDX experiments are performed with an Oxford Instruments INCA Energy 350 Microanalysis system including a 30 mm^2 INCA PentaFET-x3 Si(Li) detector. The resolution of this system is better than 133 eV at Mn Kα for count rates up to 4000. The measurements are typically performed with 5 mm working distance, beam intensity adjusted to give 2000 counts per second, and a data collection time of 10 minutes.

2.3 Results and Discussion

2.3.1 Catalyst deposition

The ECD technique combined with our test structures is successful in depositing Ni catalyst nanoparticles selectively on the sidewalls of the TiN electrodes connected to the substrate, as illustrated in Fig. 2.5. Indeed, Ni deposition occurs only on those electrodes that have a direct electrical contact to the Si substrate. Since the SiON hard mask layer on top of the TiN electrodes blocks the current flow, the nanoparticles are formed only on the exposed TiN sidewalls.

In Fig. 2.6 we present a typical cyclic voltammetry measurement carried out in order to evaluate the reduction potential of the electrolyte solution. The forward scan (F) reveals a current increase starting at -1.2 V (reduction potential, indicated by a dashed arrow in the inset of Fig. 2.6). When the applied potential is reversed (reverse scan R), it

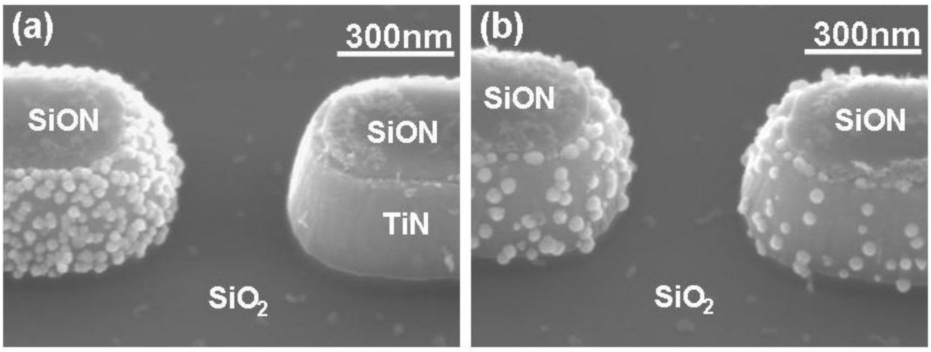

Figure 2.5: Tilted (45°) SEM images of Ni catalyst nanoparticles electrodeposited on the sidewalls of TiN electrodes in (a) configuration A (only the left electrode is connected to the substrate), ECD parameters: U = -1.5 V vs. Ag/AgCl, t = 50 ms and in (b) configuration B, 400 nm gap spacing, ECD parameters: U = -1.3 V vs. Ag/AgCl, t = 80 ms. In both images the electrode gap is 400 nm.

reaches the potential that reoxidizes the product formed in the previous reduction (oxidation potential). As an effect a positive current peak is recorded at around -0.3 V (indicated by a dotted arrow in the inset of Fig. 2.6). This measurement indicates that the potential able to deposit Ni nanoparticles from the electrolyte solution needs to be more negative than -1.2 V.

In general, by controlling the applied potential U, an excellent control over the nanoparticle density N_p is obtained as illustrated in Fig. 2.7 (a). Typical SEM images of the particles deposited on the electrodes for applied potentials of -1.25 V, -1.3 V and -1.5 V are presented in Figs. 2.7 (b), (c) and (d), respectively. N_p varies from around 10^9 to around 10^{11} particles cm^{-2} for an applied potential between -1.25 V and -1.50 V. The nanoparticle density increases slowly for even more negative potentials and saturates at 3×10^{11} particles cm^{-2} around -2 V. For such density and an average particle size of 25 nm, the interparticle distance is approximately 15 nm.

Note that the slight difference in the nanoparticle density between the left and right electrode in Fig. 2.5 (b) (same applied potential) is due to a larger resistive path (i.e. smaller effective electrode potential)

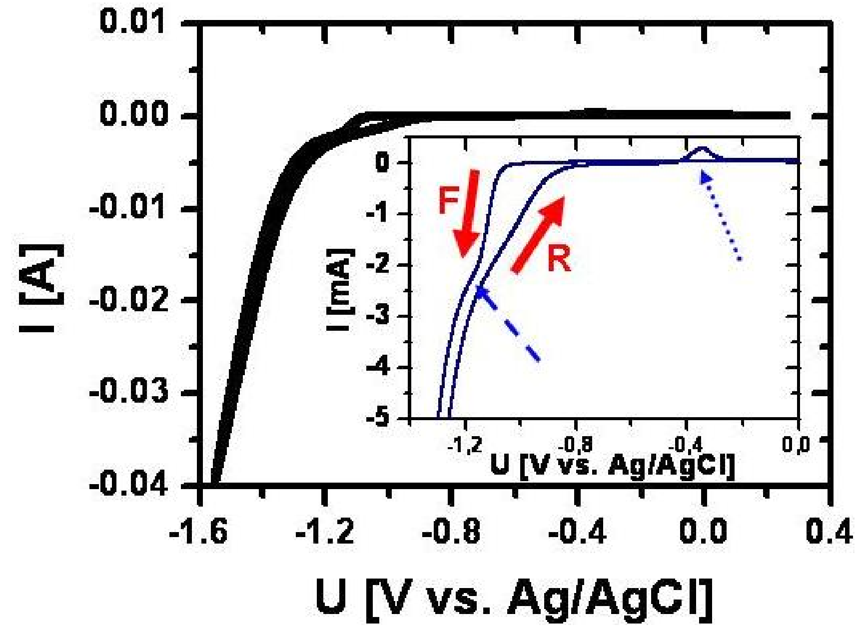

Figure 2.6: Cyclic voltammetry measurement.

for the electrode connected to the substrate by the "scribe line" (longer and more resistive path).

By controlling the deposition time t an excellent control over the nanoparticle average size d is obtained as illustrated in Fig. 2.8 (a). Typical SEM images of the particles deposited on the electrodes for deposition times of 10 ms, 20 ms and 50 ms are presented in Figs. 2.8 (b), (c) and (d), respectively. For an applied potential of -1.3 V ($N_p \sim 10^{10}$ particles cm^{-2}) the average nanoparticle size increases from 16±4 nm to 30±4 nm for deposition times between 10 and 100 ms. This trend agrees very well with the theoretical relationship between particle size d and ECD time t (derived from Faraday's law and the Cottrell equation for diffusion limited growth [22]):

$$d = {\frac{2nFD^{1/2}C_b}{\sqrt{\pi}KN_p}}^{1/3} \times t^{1/6}, \tag{2.1}$$

where $n = 2$ is the number of electrons involved in the reaction, $F = 96487\ \mathrm{C\ mol^{-1}}$ is Faraday's constant, $D = 0.66\times10^{-5}\ \mathrm{cm^2 s^{-1}}$ is the diffusion coefficient of Ni^{2+} ions at infinite dilution and at 25 °C [97],

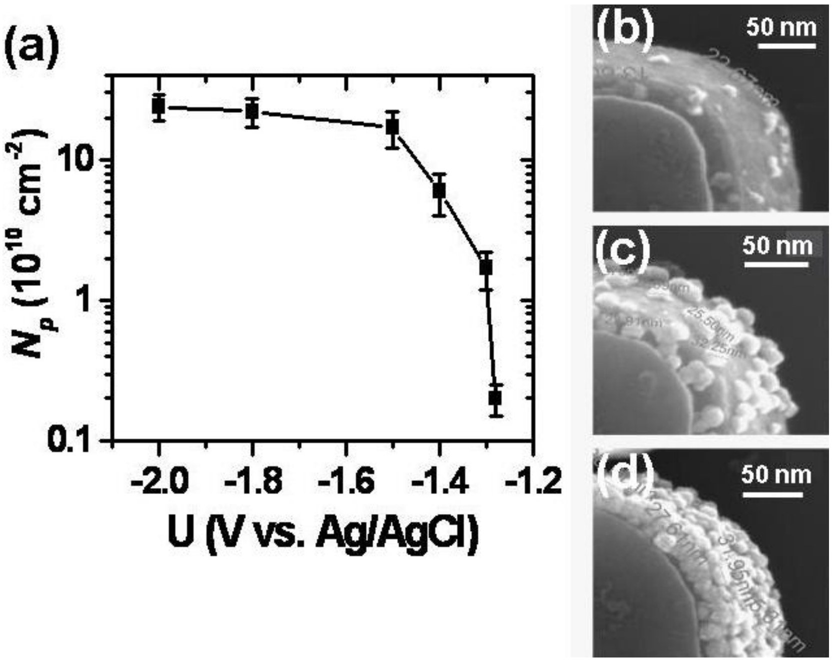

Figure 2.7: (a) Nanoparticle density (N_p) as estimated from SEM images versus applied potential (U) for a constant ECD time of 50 ms. SEM images of nanoparticle deposition for an applied potential of (b) -1.25 V, (c) -1.3 V and (d) -1.5 V.

$C_b = 1\times10^{-5}$ mol/cm^3 is the bulk concentration (concentration of the reducible analyte), $K = 7.65\times10^3$ C cm^{-3} is a constant valid for hemispherical Ni nanoparticles.

Non-uniformities in the nanoparticle average size and density are observed due to local differences in the effective potential, as already observed in Fig. 2.5 (b), and in the Ni^{2+} ions flux, which results in a variation of the current density from one point to the other [97]. A higher concentration of particles is typically found at the SiON-TiN boundaries, while larger particles are found at edges, which is consistent with the fact that nucleation of particles is expected to be favored at defect sites and edges [97]. These non-uniformities do not affect the conclusions of our work; nonetheless, they have to be considered when ECD is proposed to deposit particles on particular geometries or large areas, where the current density considerably varies from point to point.

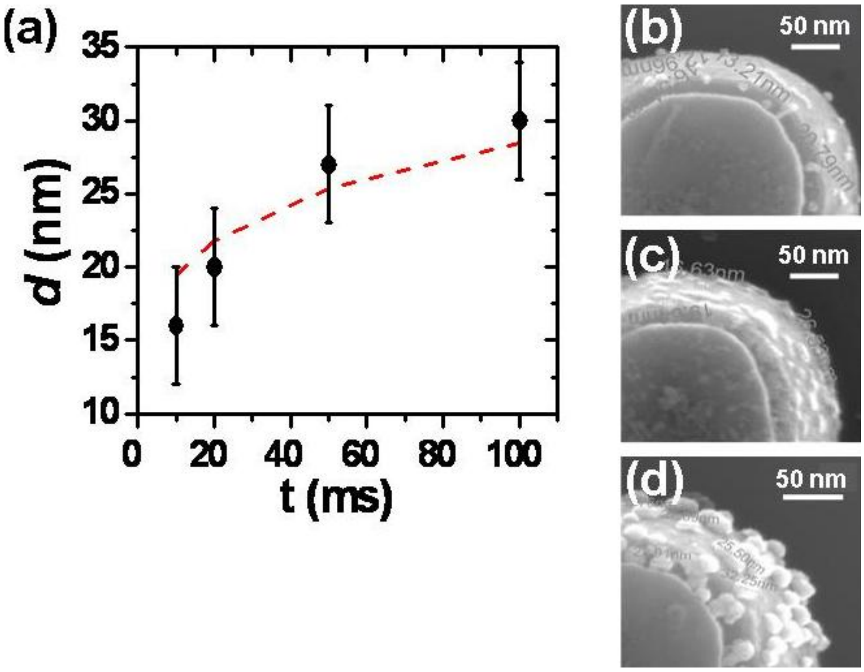

Figure 2.8: (a) Nanoparticle average size (*d*) as estimated from SEM images versus deposition time (*t*) for a constant applied potential of -1.3 V. For comparison the predicted trend according to the Eq. 2.1 is indicated as well (dashed line). SEM images of nanoparticle deposition for deposition times of (b) 10 ms, (c) 20 ms and (d) 50 ms.

2.3.2 Carbon nanotube growth

Horizontally suspended CNTs are grown from the nanoparticles on the electrode sidewalls with good control of diameter and density, corresponding to the nanoparticle average size and density, respectively. Typically, Ni particle diameters of 16-30±3 nm result in CNT diameters of 18-30±4 nm. A similar one-to-one relationship between ECD catalyst size and CNT diameter has been reported in vias [23]. Concerning the nanoparticle density, we find that a limited number of nanoparticles do not result in the nucleation of CNTs and remain visible on the electrode sidewalls. This is likely due to the absence of a pre-growth treatment. Note that for ECD particles in vias all nanoparticles do yield CNTs after plasma pretreatment [23]. However, in our case plasma treatment results in some resputtering of Ni, leading to parasitic CNT growth on the “blank” electrodes of configuration A and is therefore omitted.

In Fig. 2.9 we present SEM images of CNTs grown from Ni catalyst nanoparticles on the TiN sidewalls for configurations A (Fig. 2.9 (a)) and B (Fig. 2.9 (b)). CNTs grow only from one electrode in configuration A and from both electrodes in configuration B, as expected from the selective ECD Ni catalyst placement. Note that the CNTs grow from the sidewalls of the complete electrode structure, including the contact pads, since nanoparticles are deposited all around the exposed sidewalls of the TiN structure. In a limited number of samples carbon deposits are observed on top of the electrodes (Fig. 2.9 (a)). Deposits are found as well on reference structures that are not subjected to ECD and are introduced in the CVD chamber in the absence of a carbon source. They originate from contamination resulting from previous runs, even though the CVD chamber was regularly cleaned using an oxygen plasma.

In configuration A CNTs grow from the catalyst nanoparticles deposited on one electrode and contact the opposing electrode with the CNT outermost shell only (Fig. 2.9 (a)). Details of the CNT base, which grows from the catalyst particles, and the CNTs landing on the TiN electrode surface are shown in Fig. 2.10 (a) and Fig. 2.10 (b), respectively. In configuration B CNTs grow simultaneously from both electrodes, now electrically connecting the electrodes also by a contact between the outermost shells of two CNTs (Fig. 2.9 (b)). An example of such a contact is shown in Fig. 2.10 (c). More details about the different contact scenarios and their role in the electrical performance of the CNT interconnects are provided in the following chapter.

By decreasing the growth temperature from 640 °C down to 480 °C (sample temperature) the CNT growth worsens. Less and shorter CNTs grow at 550 °C and only few curly and very short CNTs grow at 480 °C. The reduction of the growth temperature results in a reduction of the number of particles that are able to nucleate CNTs. At the lower temperatures CNTs grow much slower according to an Arrhenius type dependence of the growth rate on the growth temperature. The growth rate is estimated to be around 165±15 nm/minute at 640 °C. From the values of the growth rates at different temperatures an Arrhenius activation energy around 0.33±6 eV/atom is calculated, which is consistent

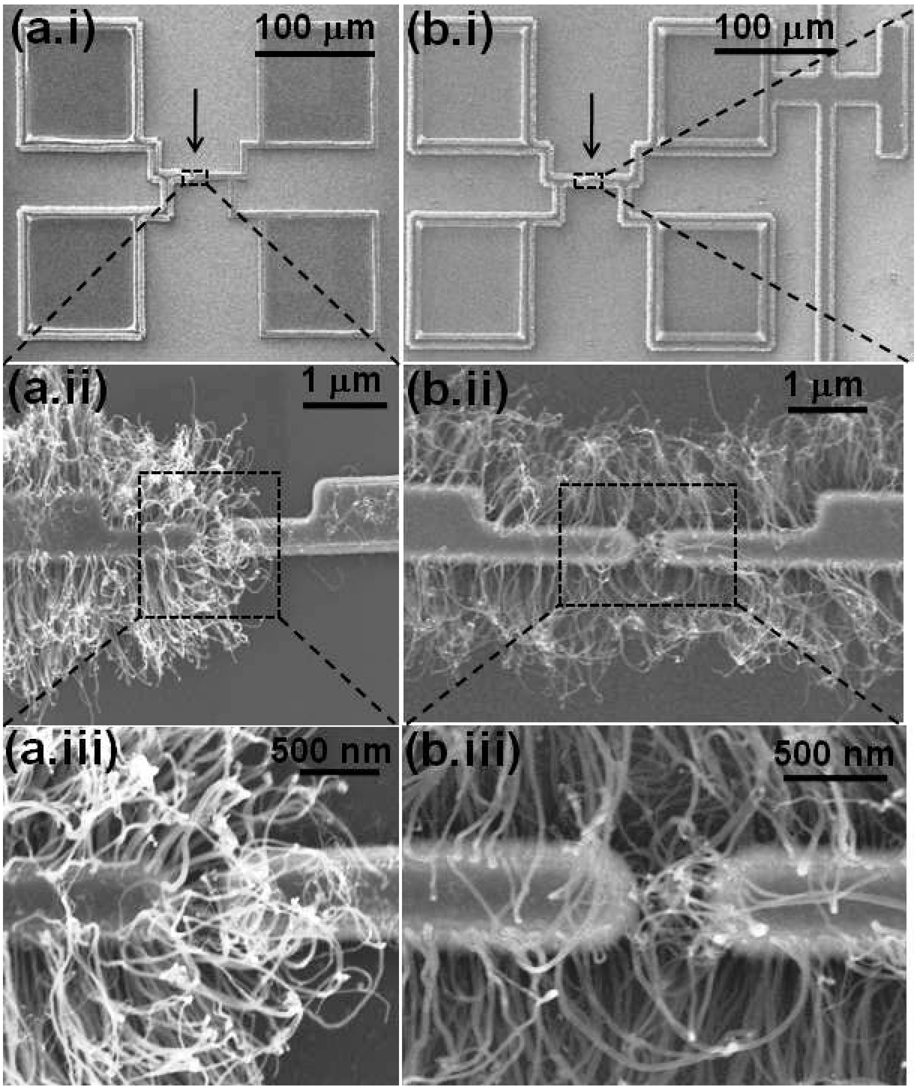

Figure 2.9: SEM top-view images of TiN electrodes after CNT growth for (a) configuration A and (b) configuration B. (a.i and b.i) Low magnification view showing the four large contact pads and the connections to the center electrodes. CNTs grow along the sidewalls of the left electrode in configuration A and along the sidewalls of both electrodes in configuration B, including the areas around the connecting leads and contact pads. Detail of CNTs bridging the 400 nm electrode gap for (a.ii and a.iii) configuration A and for (b.ii and b.iii) configuration B.

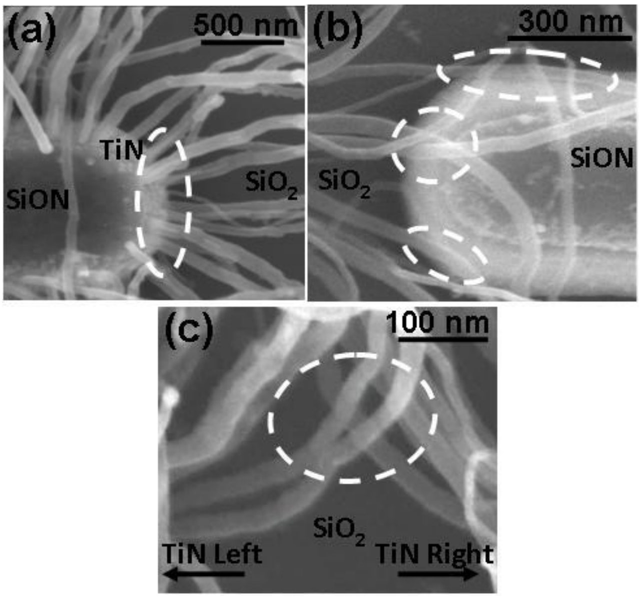

Figure 2.10: Details of the different contact scenarios for CNT interconnects: (a) base of CNTs grown from a TiN electrode, (b) CNTs landing on the opposing electrode for configuration A, and (c) touching contacts between CNTs for configuration B. In this image, the left and right TiN electrodes are out of view and are indicated by black arrows as identified from lower magnification images. Contact regions are marked by white dashed ellipses.

with the diffusion of C atoms on a Ni surface [98]. The reduced growth rate at lower temperatures reduces the length and the alignment of the CNTs, that tend to have a curly shape.

By increasing the growth time for a fixed growth temperature of 640 °C the CNT length increases. However, CNTs grow parallel to the substrate up to lengths of the order of 2 μm (15 minutes growth time at 640 °C) as illustrated in Fig. 2.11 (a). For longer growth times, the CNTs curl back towards the electrode structures with total lengths up to 5 μm after 30 minutes growth (Fig. 2.11 (b)). The bending is likely to be a result of the curving of the electrode sidewalls (see Fig. 2.5) in combination with the higher concentration of Ni particles that are typically found at the SiON-TiN boundaries (as already discussed in Section 2.3.1, electrochemical nucleation is favored at defect sites and edges [99]). CNTs would then bend due to the van der Waals attrac-

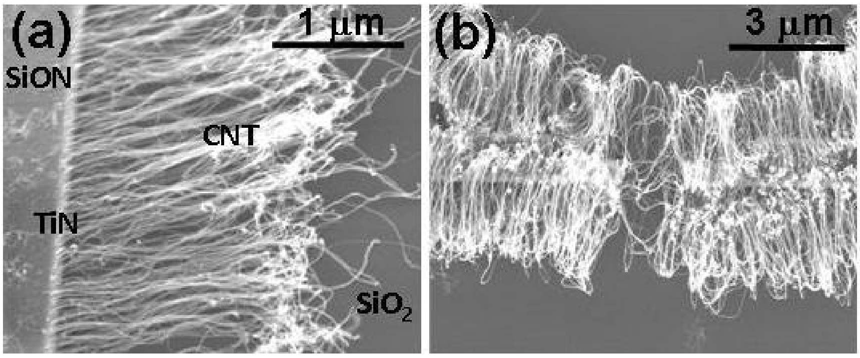

Figure 2.11: SEM images of CNTs grown from TiN sidewalls: (a) straight 2 μm long CNTs at the edge of a large contact pad (45° tilted view); (b) curled-back CNTs around two opposing electrodes for configuration B with 2 μm electrode gap.

tion towards the higher density of CNTs that grow from the SiON-TiN boundary regions.

In a recent report [100] it has been argued that van der Waals interactions between CNTs and an adjacent structure can be strong sufficiently to alter the CNT growth direction. This explanation appears to be not valid for our configuration, as CNTs grow parallel to the substrate up to 2 μm and can no longer experience Van der Waals attraction induced by the electrode they grow from. In our structures the slightly curved sidewalls would lead to a fanning out of the CNTs when no interaction exists between the CNTs. In reality, CNTs tend to bundle by van der Waals attractive forces F_{vdW} that, in the case of two identical parallel cylinders, i.e. two CNTs, are given by

$$F_{vdW} = A\frac{Ld^{1/2}}{16h^{5/2}}, \tag{2.2}$$

where d and L are the diameter and the length of the CNTs, respectively, h is the distance between two neighboring CNTs (inversely proportional to the CNT density), and A is the Hamaker constant of the material [101]. Since the Van der Waals force F_{vdW} is stronger when the CNT length L and the CNT density ($\propto 1/h$) increase and a higher CNT density is present near the top of the structures (at the SiON-TiN boundaries), the CNTs start to curl back when their length increases above a certain value. Note that the Van der Waals force F_{VdW} also increases also with the CNT diameter d. An increase of the bending should

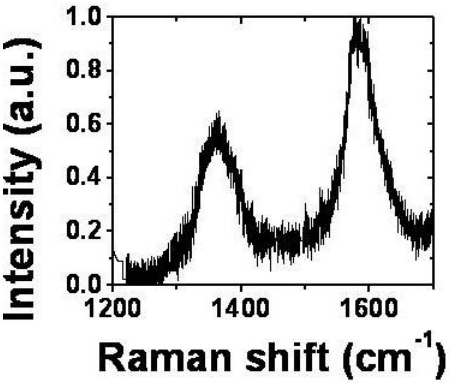

Figure 2.12: Raman spectrum measured at an excitation wavelength of 457.8 nm for the sample of Fig.2.11 (a).

therefore be observed for increasing CNT diameter. Such a dependence is not observed because the CNT bending is also inversely proportional to the CNT Youngs modulus that increases with the CNT diameter.

In order to evaluate the quality of as-grown CNTs Raman spectroscopy measurements are carried out. Figure 2.12 presents the Raman spectrum corresponding to the sample in Fig. 2.11. A Raman active E_{2g} mode at 1587 cm^{-1} characteristic of graphitic sheets (G-band) is present. A sharp well-defined G-band indicates that the walls of the tubes mainly consist of sp^2 bonded carbon with a high degree of order. A second Raman signal at 1365 cm^{-1} (D-band) is also present and arises from disorder within the carbon lattice and from amorphous carbon species formed during the CVD growth process. The D/G intensity ratio of about 0.6 indicates CNT purity comparable to the highest quality CNTs that can be produced using thermal CVD [102]. No significant radial breathing mode activity is detected that indicates the absence of SWNTs.

The CNTs grown from our test structures are also characterised by EDX. Figure 2.13 demonstrates how the elemental maps look like in general for the growth test structures. An SEM image of the structure and the related EDX intensity chart are presented in Fig. 2.13 (a) and Fig. 2.13 (b), respectively. It is possible to clearly see the CNTs in the carbon map of Fig. 2.13 (c) and the Ni particles in the nickel map of Fig. 2.13 (f). These particles are either particles that did not nucleate

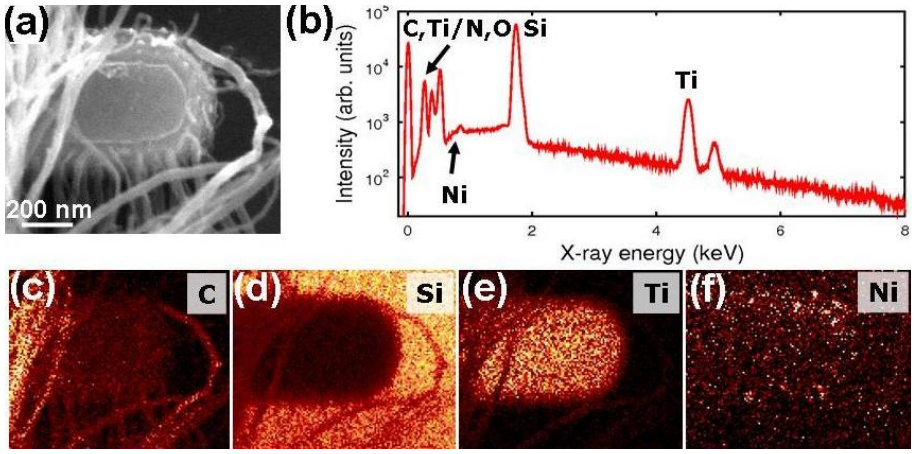

Figure 2.13: (a) SEM top view image of CNTs that grow from one electrode of the growth test structures; (b) EDX intensity chart of the sample in (a); EDX elemental maps of (c) C, (d) Si, (e) Ti and (f) Ni.

CNTs or particles present at the base of the CNTs, indicative of a base type growth. Note that the X-ray detector is located at the top-right position in these images, implying that signals arising from particles on the bottom wall are shadowed by the growth test structures and the resulting contrast is lower than on the top surface.

Figure 2.14 presents an EDX measurement on a wider region, which now includes two opposing electrodes (configuration A). The EDX spectra are collected on three different regions of the SEM image in Fig. 2.14 (a) and are plotted together in Fig. 2.14 (c). Even if in the elemental map of Ni (Fig. 2.14 (b)) the right electrode shows some contrast, comparison of the spectra reveals that this is caused by an elevated background noise and there is no Ni peak in the spectrum. This result confirms the selectivity of the ECD catalyst deposition that occurs only on the electrodes connected to the substrate (left electrode in Fig. 2.14 (b)).

Figure 2.15 (a) presents a TEM cross section view of CNTs grown from the sidewalls of the electrodes in the growth test structures. The sample is first covered with a glass cap layer and a platinum cap layer. Next, it is thinned by FIB lift-out as described in Section 2.2.5, to be then glued on the TEM grid and imaged. The glass cap layer does not

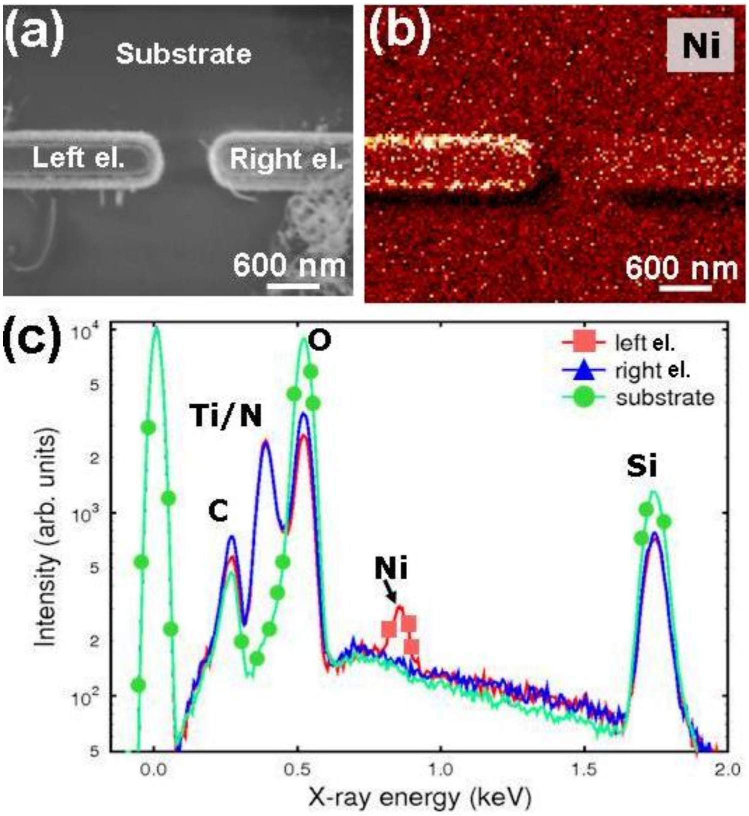

Figure 2.14: (a) SEM top view image, (b) EDX Ni map and (c) EDX intensity chart for configuration A.

penetrate in between the CNTs. Many defects due to doping implantation are visible at a shallow depth in the Si substrate. About 2 μm long CNTs grow suspended and parallel to the substrate (Fig. 2.15 (b)). Catalyst nanoparticles are mostly present on the electrode sidewalls. They have a conical shape and contain twin defects. Other particles with elongated shapes are embedded in the CNTs or present at their tips. This indicates the coexistence of base and tip growth (Fig. 2.15 (c-e)). A speckled contrast is clearly visible at the surface of the CNTs due to Pt from the second cap layer that penetrates through the non-closed CVD glass layer (Fig. 2.15 (f-h)). Some CNTs look to be amorphous and graphene structure is visible only in few CNTs, most likely due to the damage induced by the FIB preparation.

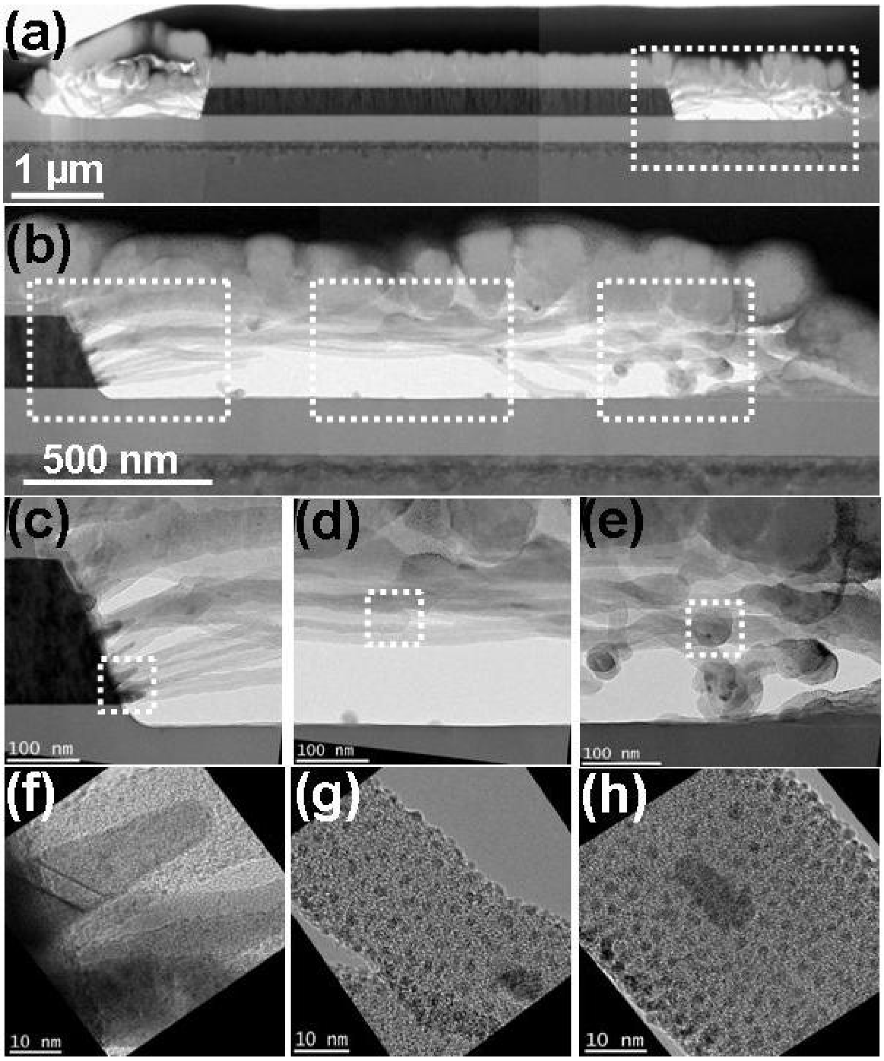

Figure 2.15: TEM cross section view of CNTs grown from the sidewalls of the electrodes in the growth test structures. (a-b) Low and (c-h) high magnification view.

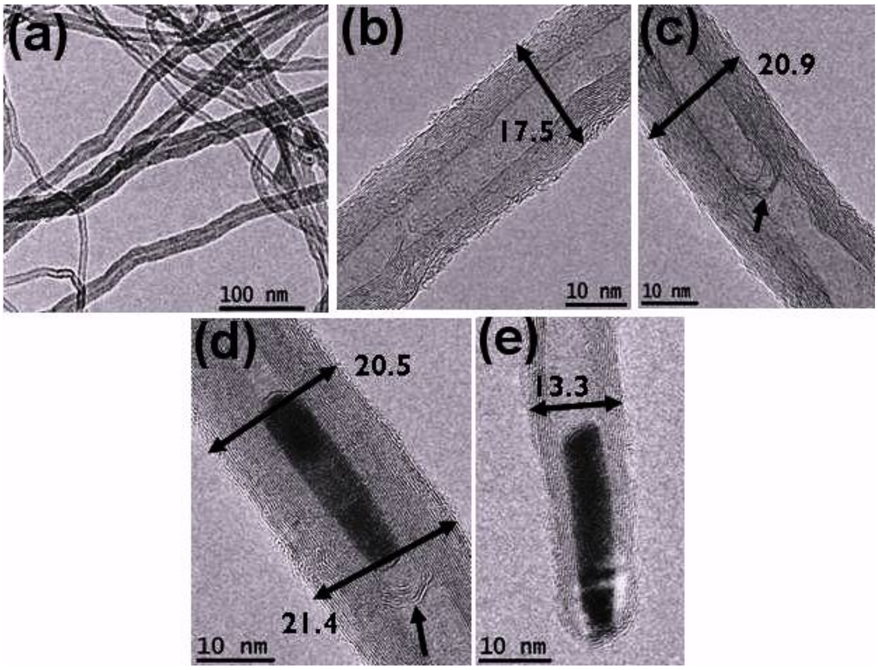

Figure 2.16: TEM images of CNTs removed from the substrate by sonication in ethanol and deposited on the TEM grid: (a) low magnification view of a hole on the TEM grid; (b) Multi-walled structure of a CNT; (c) MWNT with a kink indicated by an arrow; (d) MWNT with a kink indicated by an arrow and an internal elongated Ni particle; (e) MWNT with a elongated Ni particle present at its tip or base.

The above described approach does not allow to analyse the CNT graphitic structure due to the damage induced by the FIB preparation. This information can be obtained by imaging CNTs sonicated and dispersed in ethanol, as illustrated in Fig. 2.16. Note that this measurement relies on CNTs grown from catalyst particles deposited on a non-patterned TiN substrate with the same growth conditions used for the growth test structures. This other type of sample is preferred because the number of CNTs is higher than in the case of CNTs grown from our growth test structures. This way, the density of CNTs present in the ethanol solution is high and CNTs can be easily found on the TEM grid (Fig. 2.16 (a)).

CNTs are multi-walled (MWNTs) with diameters ranging from 13 nm to 21 nm and increasing with the number of walls (Fig. 2.16 (c-d)). In few cases a layer of amorphous carbon is observed around the CNT outermost shell and it owes to the CVD growth process. Elongated crystalline catalyst particles are observed inside the CNTs (Fig. 2.16 (d)). Some of these particles are clearly at the top or bottom of CNTs (Fig. 2.16 (e)) but it is not possible to distinguish between the top and bottom part of the CNTs once they are deposited on the carbon grid. In general their graphitic structure appears to be of the highest quality that can be obtained using thermal CVD.

2.4 Conclusions

In this chapter we described a novel method to grow CNT horizontal interconnects. ECD is demonstrated to be an effective method to selectively deposit nickel catalyst nanoparticles on non-planar conducting surfaces. The ECD selectivity is confirmed by EDX analysis. A high control of the density (up to 3×10^{11} particles cm^{-2}) and average size (15-30 nm) of the catalyst particles is demonstrated. This control is directly translated into a similar control over the CNT density and diameter.

Horizontally suspended CNTs are grown by CVD from one TiN electrode towards the opposing electrode or from both opposing electrodes. Different types of electrical contacts are created between the TiN electrodes and they will be described in detail in the following chapter.

CNTs grow parallel to the substrate up to lengths of the order of 2 μm. For longer growth times, they curl back towards the electrode structures due to the van der Waals attraction resulting from the higher density of CNTs that grow from the top regions. This finding suggests that bending phenomena may become a problem when considering CNTs for long (over 2 μm) horizontal interconnects. Electrodes thicker than the electrodes present in our growth test structures may be able to push forward the CNT horizontal alignment, since the sidewall curvature, which is inevitable because of the limits of the lithographic process, would then be reduced.

CNTs grown by our CVD method have a D/G ratio of 0.6, indicating they are of the highest quality that can be obtained using thermal CVD. TEM analysis shows we grow MWNTs that present residual catalyst particles along their length or at their tip or base.

Our approach can be applied as a route towards future horizontal interconnects and different nanoelectronic devices that rely on CNT electrical interconnects such as chemical sensors and NEMS devices.

2.5 Outlook

In this outlook section we present some preliminary results about a novel method for CNT y-junction growth and we propose some future work to further develop this method.

2.5.1 Growth of carbon nanotube y-junctions

The possibility to produce CNT Y and X junctions is important for electronic, optical and mechanical applications. Such junctions are difficult to create because only CNTs with the same chirality [103] and diameter [104] are demonstrated able to join. Moreover, this joining can occur at defect sites (vacancies, dangling bonds) that need to be created, for example, by Joule heating [104] or by electron beam irradiation [103, 105]. Alternatively, junctions between CNTs can be produced by depositing catalyst nanoparticles on the CNTs (primary CNTs) and growing new CNTs (secondary CNTs) from these catalyst nanoparticles [106–109]. However, the deposition of catalyst nanoparticles on the CNTs typically requires the presence of defects on the CNT surface formed, e.g., by oxidation [109] or doping [108]. In general, the attempts of growing CNTs from CNTs were not very successful and only short, defective and with small diameters secondary CNTs could be grown from the primary CNTs [106, 107, 109].

The method that we suggest to further investigate in this section is based on the iteration of the CNT growth method described in this chapter and is schematically presented in Fig. 2.17 (a) for the growth test structures described in Section 2.2.1. Note that this method can be also extended to the growth test structures used for CNT vertical growth in vias [23], as described in Fig.2.17 (b).

The Ni catalyst nanoparticles are deposited by ECD and the CNTs are grown by CVD as already demonstrated (Fig. 2.17 (a.i) and Fig. 2.17 (a.ii) for the horizontal growth, Fig. 2.17 (b.i) and Fig. 2.17 (b.ii) for the vertical growth). Next, another step of ECD is carried out and the CNTs, now incorporated with the substrate as working electrode, are decorated by Ni nanoparticles (Fig. 2.17 (a.iii) for the horizontal growth and Fig. 2.17 (b.iii) for the vertical growth). Finally, from the decorative Ni nanoparticles new CNTs are grown by CVD from the primary CNTs. Note that in the second step of ECD, the particles are deposited also in the free spaces between the CNTs so that the primary CNT growth is also iterated.

In Figs. 2.18 we present some preliminary results of the proposed method. In particular, in Figs. 2.18 (a) and (b) we present the CNTs grown from the horizontal growth test structures and decorated by Ni nanoparticles. Ni nanoparticles with diameters up to 50 nm decorate the CNTs most likely at the defect sites.

Figures 2.18 (c), (d) and (e) show some preliminary results on the growth of CNTs from CNTs. In particular Fig. 2.18 (c) shows a SEM image of particles that are not able to nucleate secondary CNTs while they rather diffuse into the tubes and appear covered by carbon onions. A similar metal-CNT interface dynamic has been observed in the Ref. [110] as produced by the high temperatures induced by Joule heating. In this case the temperature that cause the diffusion of the particles into the CNTs is the growth temperature of the secondary CNTs ($\sim$750 °C). Figs.2.18 (d) and (e) show two examples of y-junctions grown by the proposed method.

The proposed method does not require the formation of defects on the primary CNTs to deposit the catalyst nanoparticles. The nucleation of the ECD nanoparticles is in fact favored at the defect sites [97] that are already present along the CNTs grown by CVD. Moreover the selectivity of the method is kept as the particles decorate only the CNTs that grow from the electrodes electrically connected to the substrate

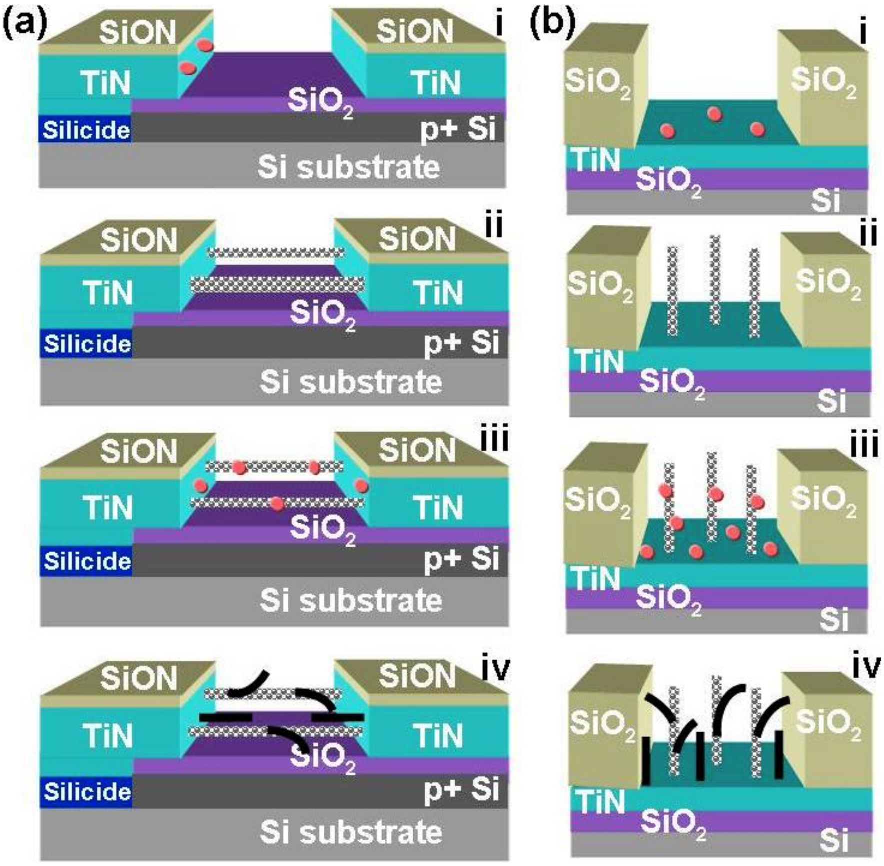

Figure 2.17: Schematic view of the CNT y-junctions growth method for (a) the growth test structures for horizontal growth described in Section 2.2.1 (configuration A) and for (b) the growth test structures used for CNT vertical growth in vias and described in the Ref. [23]. (a.i)-(b.i) The Ni catalyst nanoparticles are deposited by ECD. (a.ii)-(b.ii) The primary CNTs are grown by CVD. (a.iii)-(b.iii) Another step of ECD is carried out and the CNTs are decorated by Ni nanoparticles. (a.iv)-(b.iv) Secondary CNTs are grown from the primary CNTs by CVD from the decorative Ni nanoparticles used as new catalyst.

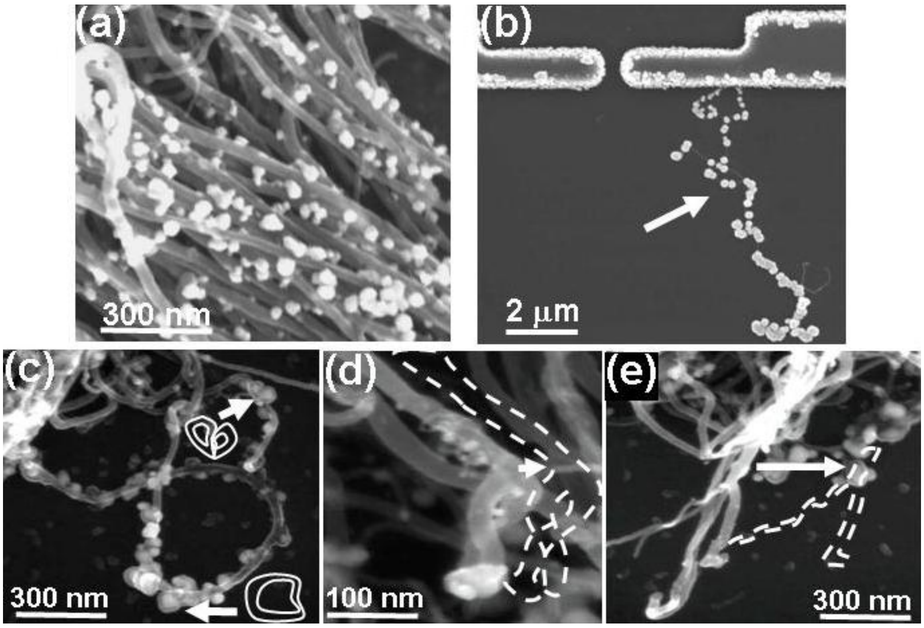

Figure 2.18: SEM images of Ni catalyst nanoparticles that decorate the CNTs grown (a) from the pads of the horizontal growth test structures and (b) from one of the electrodes connected to the substrate in an example of configuration B. SEM images of the growth of secondary CNTs from the primary CNTs: (c) particles that are not able to nucleate secondary CNTs while they rather diffuse into the tubes and are covered by carbon onions; (d-e) CNT Y-junctions.

(Figs.2.18 (b)). As future work we suggest to further investigate the proposed method. In particular for CNT growth in vias this method could lead to an increase of the CNT density as it allows to iterate also the primary growth. The role of the growth temperature on the secondary CNT growth and the electrical properties of such y-junctions could be also interesting to study.

Chapter 3

Electrical Characterisation of Carbon Nanotube Horizontal Interconnects

3.1 Introduction

The production of CNT electrical interconnects is extremely important to replace copper in integrated circuits and for sensing applications. One of the bottlenecks to produce reliable CNT electrical interconnects is the lack of control over the CNT growth, in particular for CNT horizontal interconnects. This issue was discussed in Chapter 2 and a novel method for horizontal CNT growth was proposed. Another bottleneck to implement CNTs as reliable interconnects is discussed in this chapter. This is the very high CNT-metal contact resistance (up to the MΩ range [94, 111]), in particular for contacts realized without any post-growth treatment such as annealing. The high contact resistance dominates the overall CNT interconnect performance and overwhelms the intrinsic outstanding CNT properties. The high contact resistance is usually attributed to the different CNT-metal work functions and wettability [112], to the poor contact between the CNTs and the metal that is comparable to a metal-insulator-metal junction [113], as well as to the oxidation of the metal surface [114].

To date many different approaches have been proposed in order to solve the issue of the contact resistance: thermal annealing [115, 116], Joule heating induced contact annealing [110, 117–120], electron beam induced deposition of amorphous carbon at the CNT-metal interface [121], ultrasonic nanowelding [122], use of metals with high carbon bonding capability or tendency to form carbide composites by annealing [123], and “electrochemical pinning” of CNTs on the contacts [124]. Though effective to reduce the CNT-metal contact resistance, most of the proposed techniques have the drawback of being “one interconnect at a time” procedures and cannot be scaled up. Only thermal annealing may allow for up scaling. Unfortunately, this technique submits the electronic devices to an additional high temperature (up to 800 °C [115]) treatment, while present back-end complementary metal-oxide-semiconductor (CMOS) technology only allows maximum temperatures of 450 °C, in order to preserve the mechanical integrity of the low dielectric constant materials.

This chapter proposes a novel effective and scalable solution. In particular, it suggests replacing CNT-metal contacts by CNT-CNT contacts that are demonstrated to have a considerably lower resistance. First, we show that the growth method proposed in the Chapter 2 allows to electrically connect opposing TiN electrodes with electrode gaps of up to 5 μm. CNT interconnect resistances as low as 40 Ω are measured for the smallest electrode gap (200 nm) and CNTs grown from both opposing electrodes (configuration B, see Chapter 2). Next, in order to evaluate the role of the different contact scenarios, the growth method is extended to low density CNT growth. The CNT interconnects are characterised qualitatively by using Kelvin probe force microscopy (KPFM) [24] and quantitatively by electrical measurements. When two CNTs grow from opposing electrodes and touch each other with their outermost shells we find that the corresponding contact resistivity is about 14 $\Omega\mu\text{m}^2$, one order of magnitude smaller than the contact resistivity of a CNT touching the TiN surface with its outermost shell. On the other hand, the contact resistance of a CNT grown from a Ni catalyst particle deposited on a TiN electrode is negligibly small when compared to the above mentioned contact resistances. Since the proposed growth method allows to create CNT-CNT contacts with a contacting yield (number of contacts out of the number of CNTs growing from the electrodes) of up to 90%, it may provide a scalable alternative to obtain low resistance CNT horizontal interconnects.

The reported work was carried out during the third and the fourth year of the PhD research activities. It was developed in the framework of the European project CarbonCHIP at IMEC and continued at the KULeuven, Laboratory of Solid-State Physics and Magnetism. Part of the reported results have been submitted to the journal “Carbon”.

The first part of the chapter (Section 3.2) describes the used materials and methods, i.e. the four probe electrical measurements in Section 3.2.1 and the atomic force microscopy (AFM) and KPFM measurements in Section 3.2.2. Section 3.3 gives the results related to the electrical characterisation of high density CNT interconnects (Section 3.3.1). Next, the growth of low density CNT interconnects (Section 3.3.2) is introduced, which allows to perform reliable KPFM measurements (Section 3.3.3) and four probe electrical measurements (Section 3.3.4) to evaluate the increase of the resistance with the length of the CNT conduction path (Section 3.3.5), the contact resistances (Section 3.3.6) and the related specific contact resistivities (Section 3.3.7). The chapter ends with some final remarks about the locations of the CNT breakdown induced by Joule heating (Section 3.3.8) and the contacting yield (Section 3.3.9), the conclusions (Section 3.4) and the outlook for further research (Section 3.5).

3.2 Materials and Methods

3.2.1 Four probe electrical measurements

After CNT growth four probe electrical measurements are carried out on the growth test structures described in Chapter 2. The measurement tool is a semi-automated microprober system (SUSS Microtech PA300) where four 12 μm (end diameter) tungsten tips are connected to four source measuring units (SMUs) of a Semiconductor Parameter Analyzer (Agilent 4156C). An optical image of a typical four probe measurement carried out on the growth test structures is presented in Fig. 3.6 (a).

Four probe measurements are performed according to the electri-

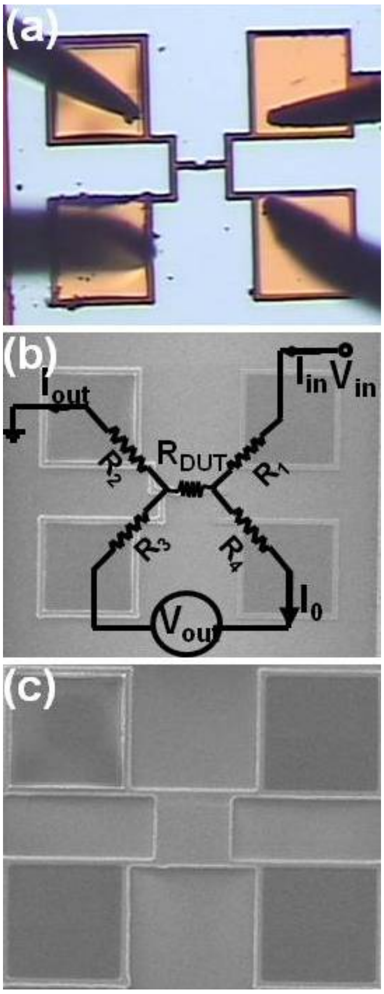

Figure 3.1: (a) Optical image of the four probes for measuring the growth test structures; (b) electric scheme of four probe measurement on the growth test structures; (c) Reference structure (TiN sheet) connected to four pads to measure the TiN resistivity.

cal scheme that is superimposed on the SEM image of the growth test structure in Fig. 3.6 (b). The resistances R_1, R_2, R_3 and R_4 are the resistances of the TiN connections between the pads and the device under test formed by the CNT interconnects in series with the TiN electrodes. A voltage is applied between two pads (V_{in}), while the current that flows through the CNT interconnects (I_{out}) and the voltage between the other two pads (V_{out}) are measured. This way, the resistances of the TiN connections R_1-R_4 are excluded from the total measured resistance of the device under test R_{dut} (see figure) because the current I_0 through the voltmeter is null. The TiN resistivity is about 10^{-4} Ωcm, as measured on a reference structure (TiN sheet) located on the same sample and represented in Fig. 3.6 (c). From this value the series resistance of the TiN electrodes is estimated to be around 100 Ω. The CNT interconnect resistance is obtained by subtracting this value from the total measured resistance. During the measurements the substrate is grounded and kept at room temperature. In a typical measurement the voltage is ramped from -1 V up to 1 V at a scan rate of 0.02 V/s.

3.2.2 Atomic force and Kelvin probe force microscopy measurements

AFM and KPFM measurements on the current carrying CNT interconnects are performed in air using a Dimension 3100 scanning probe microscope (Veeco Instruments Inc.) equipped with commercial probes (Nanosensors). For the KPFM experiments that involve charging effects the microscope operates in a dry nitrogen atmosphere in order to avoid charge leakage due to the adsorbed surface water layer. A schematic view of the setup is presented in Fig. 3.2. A cantilever with a sharp tip (probe) at its end is used to scan the sample surface. When the tip is brought close to the sample surface, forces between the tip and the sample result in a deflection of the cantilever according to Hooke's law. The deflection is measured by a laser beam reflected from the top surface of the cantilever into a photodetector. A feedback system acts on a piezoelectric tube to tune the distance and keep constant the force between the tip and the sample. The resulting map of the tube extension represents the topography of the sample.

In a typical AFM/KPFM measurement the data are taken in the

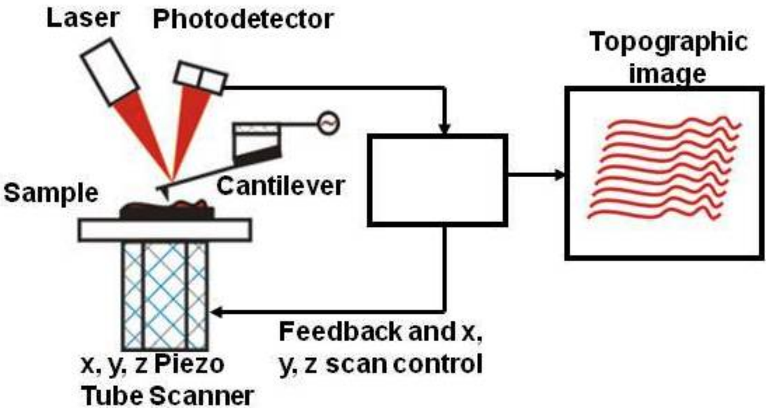

Figure 3.2: Schematic view of the AFM setup.

"lift mode" using two consecutive passes along each scan line. During the first pass AFM topographical data are acquired in "tapping" mode with the tip bias voltage set to zero. Then the tip is raised to the "lift" scan height (typically 20-100 nm) and a second scan is performed while maintaining a constant tip-sample separation and probing the local potential distribution based on the Kelvin probe method [125]. During the measurements a bias voltage of 1 V is applied between the TiN electrodes. Note that reliable KPFM measurements on sample regions that include the electrodes are possible only at lift heights that exceed the electrode thickness (200 nm). Consequently, the spatial resolution of the KPFM images of sample areas that include the electrodes is low when compared to the images taken on regions that do not include the electrodes (see below, Figs. 3.8 (c)-(d)). The local potential profiles of the current carrying CNTs are corrected by subtracting the background potential, which results from the electric field emanating from the thick TiN electrodes.

Charge injection (Section 3.5) into the CNTs is achieved by modifying the scanning parameters for a few ($\sim$8) scan lines during the second pass: decreasing the tip-sample distance ($\sim$ 20 nm), increasing the ac tip bias amplitude (1-5 V) and choosing the proper ac tip bias phase.

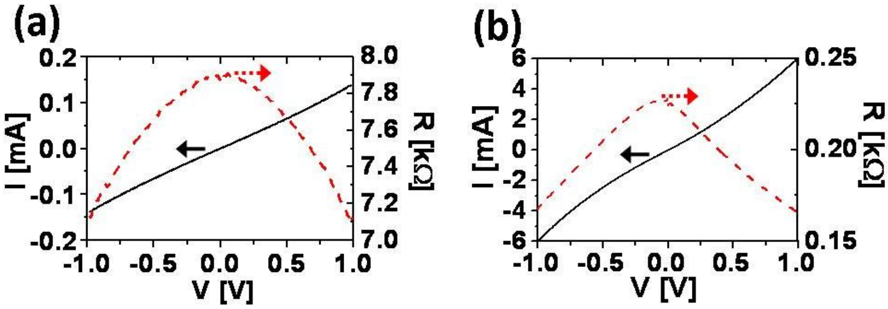

Figure 3.3: Current-voltage (I-V) and resistance-voltage (R-V) curves obtained from four probe measurements of CNT interconnects across 400 nm TiN electrode gaps in (a) configuration A and (b) configuration B. The voltage is scanned from -1 V up to 1 V at a scan rate of 0.02 V/s with voltage intervals of 2 mV at room temperature. CNT length is 5 μm; CNT diameter is 25±3 nm.

3.3 Results and Discussion

3.3.1 Electrical characterisation of high density carbon nanotube interconnects

The CNTs grown with the method proposed in Chapter 2 easily bridge electrode gaps up to 2 μm in configuration A and 5 μm in configuration B, as confirmed from the electrical measurements. In the latter case the contacts are almost exclusively by CNT entanglement, as most CNTs cannot reach the opposing electrode due to their bending that starts at CNT lengths exceeding 2 μm. However, in few cases the connection of the TiN electrodes is achieved also across 5 μm electrode gaps in configuration A due to a direct contact by one single CNT.

In Figs. 3.3 (a)-(b) we present current-voltage (I-V) and corresponding resistance-voltage (R-V) curves obtained from four probe measurements of CNT interconnects in configuration A and B, respectively. The examples refer to a 400 nm electrode gap.

The CNTs exhibit metallic behavior at room temperature, as expected for MWNTs with diameters around 25 nm [126]. In most cases a potential barrier appears to be present at low voltages and the resistance decreases with increasing applied voltage. The resistance decrease can be linked to the electronic transport through the contact regions. In particular, a thin native oxide layer on the TiN may hinder charge transfer to the CNTs. As such, each contact between CNTs and TiN mimics a metal-insulator-metal (MIM) tunnel junction [113] and opposes a barrier [127] to the current transport. The presence of a tunneling barrier is also supported by the fact that the I-V characteristics become more Ohmic after consecutive I-V sweeps, indicating that a Joule heating induced annealing [118, 120] is able to (partially) remove the original potential barrier, improving the contact quality.

In Fig. 3.4 we compare the resistance of the CNT interconnects at 0.5 V for the different electrode gaps in configurations A and B for high density (10^{11} particles cm^{-2}) and long (5 μm after 30 minutes growth) CNTs. For the 0.2-1 μm electrode gaps of configuration A and the 0.2-2 μm electrode gaps of configuration B electrical connection is obtained in all cases (20 measurements on 5 different samples). For the 2 μm electrode gap in configuration A and the 5 μm electrode gap in configuration B 11 structures are electrically connected out of 20 investigated structures. For the 5 μm electrode gaps in configuration A only 5 out of 20 structures are able to electrically connect the electrodes.

The resistance ranges between 80 Ω and 30 kΩ in configuration B and between 1 kΩ and 150 kΩ in configuration A, for electrode gaps between 200 nm and 5 μm. Since the electrical connection of the 5 μm electrode gap is rare in configuration A (see above), the measured resistance of 150 kΩ is believed to be the resistance for one single CNT connecting the TiN electrodes. This resistance value is in good agreement with that measured by Nihei *et al.* [128] under similar conditions: i.e. 135 kΩ for one 30 nm diameter MWNT connecting a 5 μm Ni-Ti electrode gap.

The resistance follows approximately a $R \propto (l_{gap})^{2.5}$ behavior. The increase in resistance with increasing electrode gap is due to three contributions:

- the decrease of the number of interconnects with the length of the gap since less CNTs are able to contact the opposing electrode

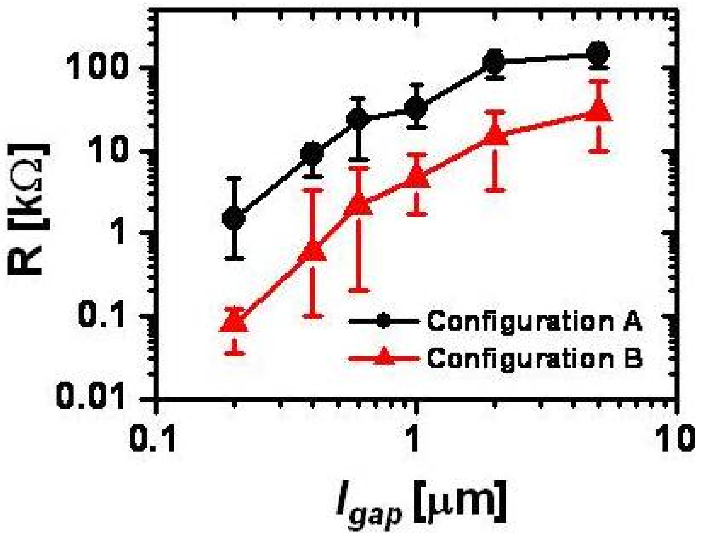

Figure 3.4: Resistance (R) at 0.5 V for CNT interconnects versus electrode gaps (l_{gap}) for configurations A and B. The results are an average of 20 measurements on 5 different samples for each gap and configuration. In the case of the 2 μm gap in configuration A and the 5 μm gap in configuration B, the results are an average of the 11 measurements that resulted in electrical contact. In the case of the 5 μm electrode gap in configuration A, the results are an average of the 5 measurements that resulted in electrical contact.

when the length of the gap increases;

- the increase of the CNT resistance with the CNT length [129];
- the increase of the contact resistance with the length of the gap; as schematically illustrated in Fig.3.5, for the same CNT length the CNT segment available for contacting the opposing electrode l_{cont} decreases when the electrode gap l_{gap} increases. This corresponds to an increase of the related contact resistance.

The last contribution appears to be the least significant since in the two configurations, where the types of contact are different, the increase of the resistance with the length of the gap follows the same law. Since we expect a $R \propto l_{gap}$ behavior for the increase of the resistance with the CNT length [129], we can conclude that the number of CNT interconnects increases as l_{gap}^2. CNTs grow from both electrodes in configu-

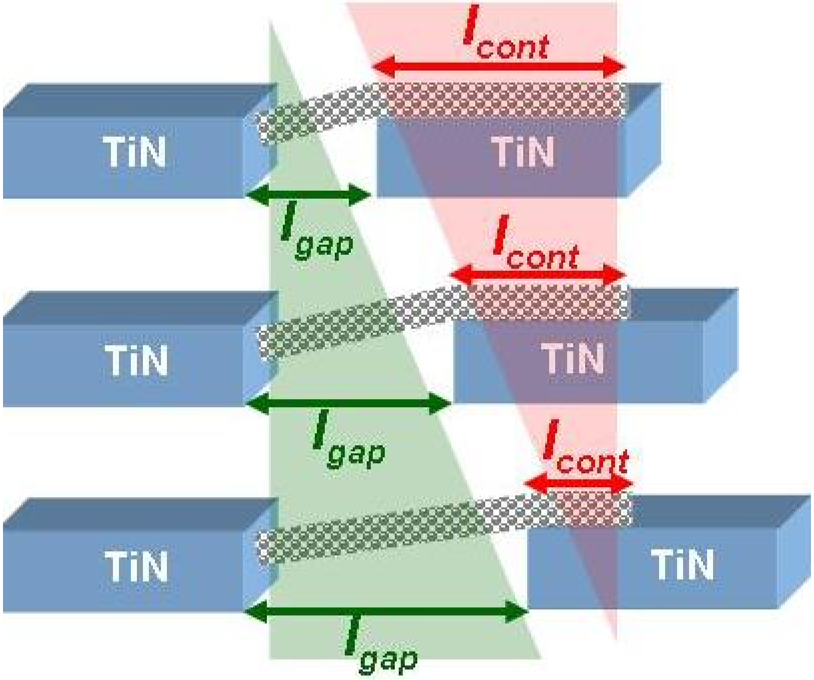

Figure 3.5: Schematic view of a CNT interconnect: for the same CNT length when the electrode gap l_{gap} increases the CNT segment that is able to contact the opposing electrode l_{cont} decreases.

ration B, which therefore has about twice as much CNT interconnects as configuration A. Consequently, one would expect configuration B to have approximately half the resistance of configuration A. Surprisingly, CNT interconnect resistances are about one order of magnitude lower for configuration B than for configuration A. This can be explained by the availability of two parallel electrical paths: one path created by the direct contact of the CNTs to the opposing TiN electrode and one path created by the contact between CNTs growing from opposing electrodes. More details about the different contacts are given in Section 3.3.2.

A record low value of 40 Ω is measured for a 200 nm gap spacing in configuration B. To our knowledge, only Cao *et al.* [71] could connect 50 μm spaced SiO_2 pillars (50 μm × 50 μm) by so many CNTs to obtain resistances as low as 100 Ω. In our case the electrode gap (200 nm vs.50 μm) as well as the “electrode tip area” (0.14 μm^2 compared to 2500 μm^2) are much smaller. We define the “electrode tip area” as the area of the electrode tip adjacent to the electrode gap and labeled by a dashed line in Fig. 3.6 (b).

Low resistance values could be obtained in our case because of the high number of contacts created. With an electrode tip area (see Fig. 3.6 (b)) of 0.14 μm^2 and a particle density of 2×10^{11}cm^{-2}, we are able to grow up to (0.14 μm^2)$\times$(2×10^{11}cm^{-2})=280 CNTs per electrode. As mentioned, two parallel electrical paths are available in configuration B: one path created by the direct contact of the CNTs to the opposing TiN electrode and one path created by the contact between CNTs growing from opposing electrodes. If we consider only the contribution of the latter electrical path, the 280 contacts between CNTs growing from opposing electrodes would correspond to a resistance of 11 kΩ per contact, about double the quantum resistance of 6.5 kΩ.

3.3.2 Low density carbon nanotube interconnects and contact scenarios

In order to evaluate the role of the different contact scenarios for configuration A and B, the method proposed in Chapter 2 is extended to the growth of low density CNT interconnects. An ECD potential ranging from -1.30 V up to -1.35 V results in low density Ni catalyst particle deposition (from $3\pm2\times10^9$ cm^{-2} up to $10\pm3\times10^9$ cm^{-2}, respectively). With such Ni particle densities and a surface of the electrode tip of 0.14 μm^2 (area labeled by the dotted red line in Fig. 3.6 (b)), it is possible to grow from 4 up to 14 CNTs from each electrode. However, out of 4-5 CNTs growing from one electrode, e.g., for a 400 nm electrode gap, only 1-2 CNTs are able to contact the opposing electrode. The CNT growth alignment is in fact worse than in the case of high density CNTs, since van der Waals forces between low density CNTs are negligible. Consequently, the contacting yield is reduced when compared to the case of high density CNTs [96]. The ECD time allows to control the average diameter of the Ni particles between 16 and 30 nm for growth times ranging between 10 and 100 ms, respectively [96]. Multiwalled CNTs (MWNTs) grow by CVD with diameter corresponding to the Ni particle diameter. Typically, Ni particle diameters of 16-30±3 nm result in CNT diameters of 18-30±4 nm, respectively.

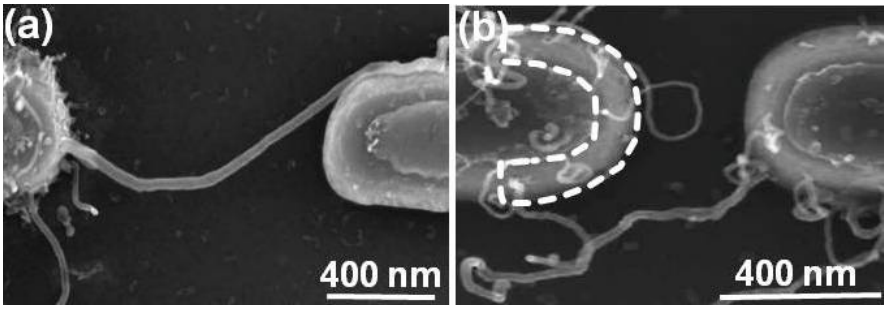

Figure 3.6: SEM top view images of single CNT interconnects for (a) configuration A (1 μm electrode gap) and (b) configuration B (400 nm electrode gap). In (b) the "electrode tip area" is labeled by a dashed line.

Fig. 3.6 presents two examples of single CNT interconnects for configuration A (Fig. 3.6 (a)), where one CNT grows from the left electrode and touches the right electrode, and for configuration B (Fig. 3.6 (b)), where two CNTs grow from opposing electrodes and touch each other in between the electrodes.

SEM and corresponding schematic views of the contact types created in the two configurations are presented in Fig. 3.7. When the CNTs grow from the particles deposited on the TiN electrodes, a strong bonding between their base with diameter d_{CNT} (Fig. 3.7 (b)) and the TiN electrodes is created (type 1 contact, Figs. 3.7 (a)-(b)). The type 1 contacts are present both for configuration A and for configuration B. When the CNTs grow from one electrode towards the opposing electrode (configuration A), they provide electrical contact by touching with their outermost shell the TiN surface over a contact length l_{cont} (type 2 contact, Figs. 3.7 (c)-(d)). When the CNTs grow from both electrodes (configuration B), they provide electrical contact also by touching each other with their outermost shells (type 3 contact, Figs. 3.7 (e)-(f)). The type 3 contacts are present only for configuration B. Note that the type 2 contacts can be present for both configurations. However, in the experiments described in the following we adapt the CNT length in configuration B in order to have only type 3 contacts.

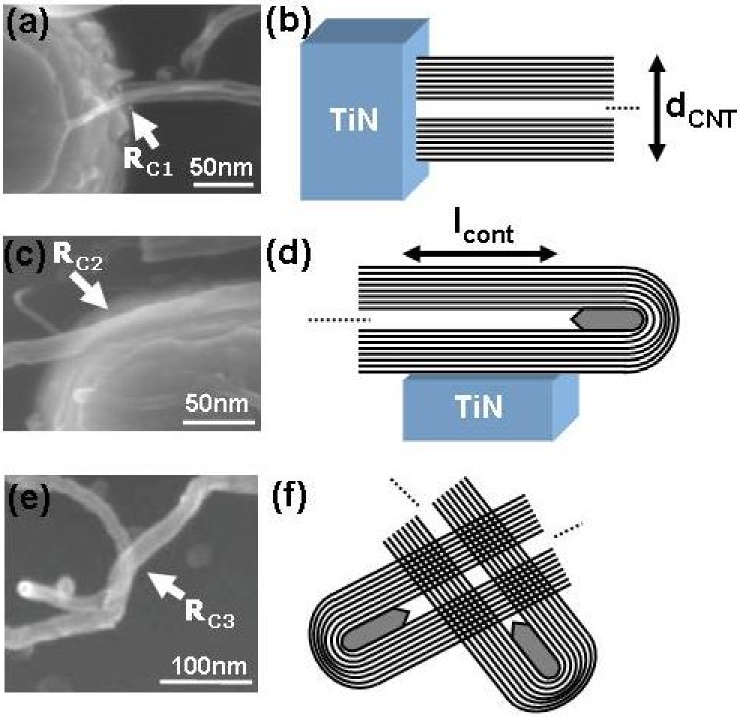

Figure 3.7: SEM and corresponding schematic view of a type 1 contact ((a) and (b)) with contact resistance R_{C1}, a type 2 contact ((c) and (d)) with contact resistance R_{C2} and a type 3 contact ((e) and (f)) with contact resistance R_{C3}. A lower magnification view for the latter type of contact, which includes the electrodes, was already presented in Fig. 3.6 (b).

3.3.3 Kelvin probe force microscopy measurements of low density carbon nanotube interconnects

With the aim of better understanding the local electrical properties of our CNT interconnects we first perform KPFM measurements. A representative example of such a measurement for configuration B is presented in Fig. 3.8. The SEM, AFM and KPFM images of the device are presented in Figs. 3.8 (a), (b) and (c), respectively. The larger scale, low resolution KPFM image (Fig. 3.8 (c)) clearly indicates that the electic potential along the CNT interconnects drops in the central region in between the electrodes (corresponding to a type 3 contact) rather than at the type 1 contacts.

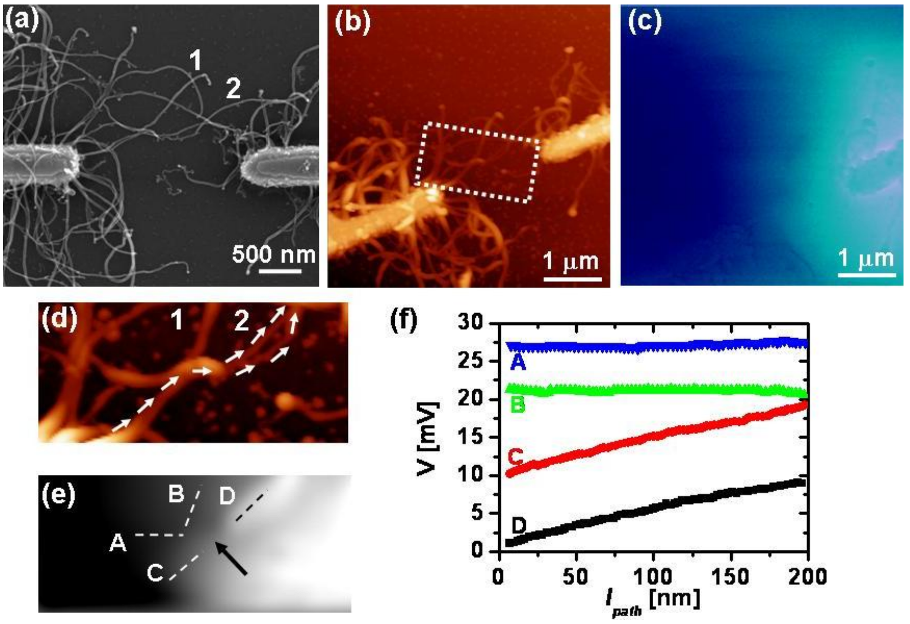

Figure 3.8: Low magnification SEM (a), AFM (b) and KPFM (c) images of an example of current carrying CNT interconnects in configuration B. The electrode gap is 2 μm. Higher magnification AFM (d) and KPFM (e) images of the rectangular area labeled by the white dotted line in (b). (f) The electric potential profiles of the CNTs in (d) and (e). The electrostatic background potential originating from the thick TiN electrodes has been subtracted. White arrows in (d) indicate the "CNT conduction path".

Fig. 3.8 (d) is a zoomed-in AFM image of the area labeled by the dotted rectangle in Fig. 3.8 (b). The corresponding KPFM image in Fig. 3.8 (e) reveals more clearly that the electric potential considerably drops at the type 3 (CNT-CNT) contact (indicated by a black arrow). To verify whether the current is running through this contact we present in Fig. 3.8 (f) the local KPFM potential profiles along the CNTs. The profiles C and D indicate that the electric potential drops uniformly along the two crossed CNTs. On the other hand, the profiles A and B indicate that the other CNTs are at equipotential. These results demonstrate that the two crossed CNTs are carrying current according to the white arrows in Fig. 3.8 (d), and that the potential drop at the type 1 contacts is much smaller than the potential drop at the type 3 contacts.

3.3.4 Electrical characterisation of low density carbon nanotube interconnects

In order to evaluate the contribution of the different contacts to the total interconnect resistance for the two configurations, a simple electrical model is developed. First, “the CNT conduction path” is defined as the path that the current follows to flow between the two opposing TiN electrodes. In configuration A (Fig. 3.9 (a)) the CNT conduction path is formed by one single CNT growing from one electrode and contacting the opposing one. In configuration B (Fig. 3.9 (c)) the CNT conduction path is formed by part of two CNTs growing from opposing electrodes and contacting each other somewhere in the middle of the electrode gap. Note that in both configurations the actual length of the CNT conduction path (l_{path}) is longer than the electrode gap length (l_{gap}) due to the bending of the CNTs and is different from the length of the CNT itself (l_{CNT}). In Section 3.3.1 it was not possible to point out this difference because the high density of CNT interconnects did not allow to appreciate it. In that case the length of the CNT conduction path l_{path} was then assumed equal to the electrode gap length l_{gap}.

We define the following resistances:

- R_A, the resistance of a single interconnect in configuration A (Fig. 3.6 (a));
- R_B, the resistance of a single interconnect in configuration B (Fig. 3.6 (b));
- R_{path}, the resistance of the “CNT conduction path”, dependent on l_{path}, as defined above for the two configurations (Figs. 3.9 (a)-(c));
- R_{C1}, the resistance of the type 1 contact (Figs. 3.7 (a)-(b));
- R_{C2}, the resistance of the type 2 contact (Figs. 3.7 (c)-(d));
- R_{C3}, the resistance of the type 3 contact (Figs. 3.7 (e)-(f)).

An equivalent circuit for the total resistances R_A and R_B can be constructed as illustrated in Fig. 3.9 (b) and in Fig. 3.9 (d), respectively.

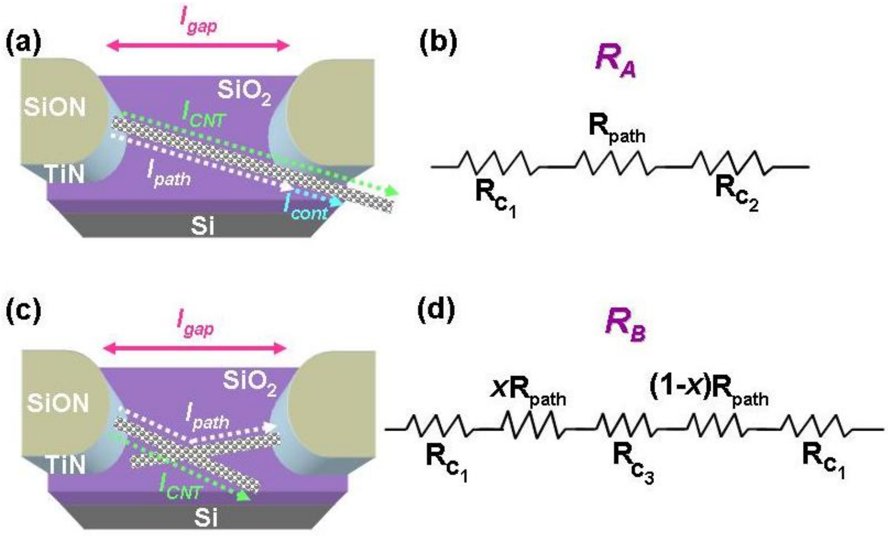

Figure 3.9: Schematic top view images of a single interconnect in configuration A (a) and in configuration B (c). Equivalent electric circuits for the corresponding total resistance R_A (b) and R_B(d). R_{path} is the resistance of the "CNT conduction path"; R_{C1}, R_{C2} and R_{C3} are the type 1 contact resistance, the type 2 contact resistance and the type 3 contact resistance, respectively, as indicated in the SEM images of Figs. 3.7 (a), (c) and (e). As highlighted in (a) and (c) l_{CNT} is the CNT length, while l_{path} is the CNT conduction path length and l_{gap} is the electrode gap length.

The resistance R_A is given by

$$R_A = R_{C1} + R_{path} + R_{C2}, \tag{3.1}$$

while R_B is given by

$$R_B = 2R_{C1} + R_{path} + R_{C3}. \tag{3.2}$$

In Fig. 3.10 we plot the resistances R_A and R_B measured at a low voltage (0.1 V), where only the outermost shell is likely to contribute to the conduction, and no shell-to-shell tunneling is expected [130]. The CNT samples for which the results are shown are prepared with Ni catalyst ECD at -1.30 V for either 100 ms or 10 ms. This results in CNTs with diameters of 30±3 nm (Fig. 3.10 (a)) and 18±3 nm (Fig. 3.10 (b)), respectively. The CNT length is adapted to the electrode gap by changing the growth time. To evaluate R_A a constant CNT length (1.2±0.1

μm for a 10 minutes growth time) is considered for all electrode gaps. To evaluate R_B the tubes are made shorter (from 150 nm up to 650 nm for a growth time ranging from 1 to 4 minutes), in order to enable electrical contact by type 3 contacts and to avoid the formation of type 2 contacts.

R_A ranges from 50 kΩ to 160 kΩ for CNT diameters of 30±3 nm and lengths of the CNT conduction path from 200 nm up to 1 μm. Higher values of R_A between 90 kΩ and 220 kΩ are obtained for CNT diameters of 18±3 nm. On the other hand, R_B ranges between 25 kΩ and 50 kΩ and between 40 kΩ and 80 kΩ for similar CNTs.

Extrapolation to $l_{path} = 0$ for a CNT diameter of 30±3 nm results in a contact resistance corresponding to $R_{C1} + R_{C2} = 50\pm11$ kΩ for configuration A and $2R_{C1} + R_{C3} = 16 \pm 7$ kΩ for configuration B. For a CNT diameter of 18±3 nm the contact resistances are $R_{C1} + R_{C2} = 92\pm8$ kΩ for configuration A and $2R_{C1} + R_{C3} = 45\pm7$ kΩ for configuration B. The KPFM measurements reveal that R_{C1} is much smaller than R_{C3}. Note that the error on the resistance values derives from the data fitting.

Since R_A is always larger than R_B, it is possible to conclude that R_{C3} is smaller than R_{C2} and that R_{C1} is much smaller than both R_{C2} and R_{C3}. If we neglect R_{C1}, the resulting contact resistances are $R_{C2} = 50\pm11$ kΩ and $R_{C3} = 16\pm7$ kΩ for a CNT diameter of 30±3 nm, and $R_{C2} = 92\pm8$ kΩ and $R_{C3} = 45\pm7$ kΩ for a CNT diameter of 18±3 nm.

3.3.5 Increase of the resistance with the length of the carbon nanotube conduction path

Both R_A and R_B increase with l_{path} (Fig. 3.10). For configuration B the variation of R_B is the result of the increase of R_{path} with l_{path} since R_{C3} can be assumed to remain constant within the indicated error bars. We are in fact dealing with a cross contact between two CNTs with roughly the same diameter. The contact area can be estimated as d_{CNT}^2 and it does not vary with varying l_{path}. The increase of R_{path} with l_{path} can be determined from the slope of R_B vs. l_{path}, providing a value of 29±9 kΩ/μm and 32±12 kΩ/μm for a CNT diameter of 30±3 nm and

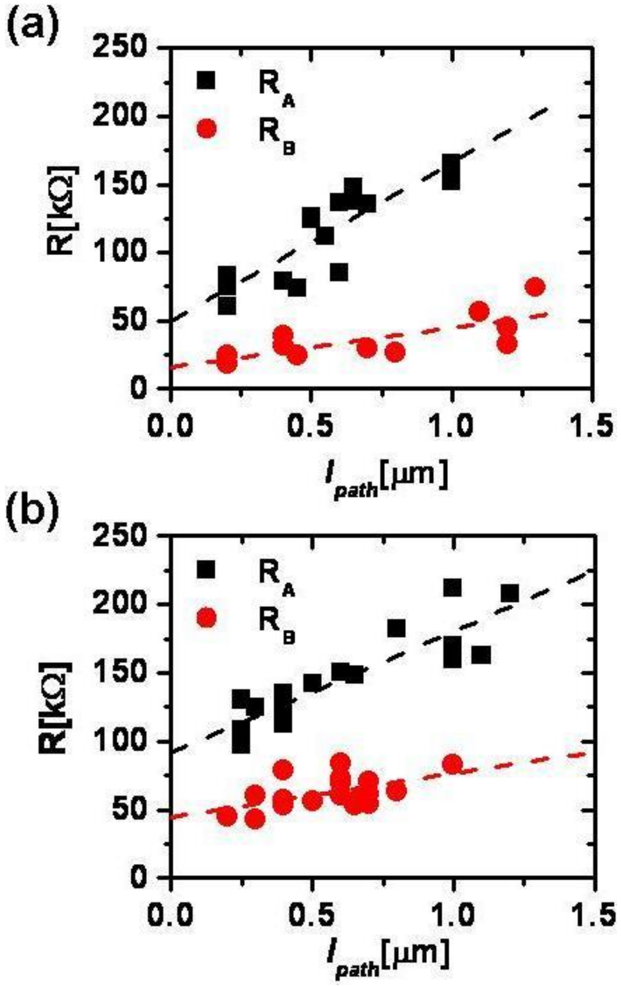

Figure 3.10: R_A and R_B versus length of the CNT conduction path (l_{path}) for CNT diameters of 30±3 nm (a) and 18±3 nm (b). The data are inferred from electrical measurements and SEM images. The resistance is measured at 0.1 V. CNT length (l_{CNT}) in the case of R_A is 1.2 μm for all lengths of the "CNT conduction path" (l_{path}), while in the case of R_B it is varied between 150 and 650 nm to allow electrode interconnection by type 3 contacts only.

18±3 nm, respectively. These values are higher when compared to the values for the single-walled CNTs (SWNTs) grown by CVD (ranging from 6 kΩ/μm [131] to 12 kΩ/μm [132]), and they are also higher than for the MWNTs grown by CVD (20 kΩ/μm [133]). Note that our CNTs are grown at a temperature of 640 °C, i.e. considerably lower than the temperatures used in the Ref. [133] (temperatures as high as 850 °C) that are known to produce higher quality CNTs.

The slope of R_A vs.l_{path} is larger than the slope of R_B vs.l_{path} (Fig. 3.10), while for the same experimental conditions the increase of R_{path} with l_{path} is expected to be the same for the two configurations. The reason for this discrepancy is that, as already discussed in Section 3.3.1, if we keep l_{CNT} constant and we increase l_{gap}, l_{cont} decreases (Fig. 3.5) and, consequently, R_{C2}. Finally, R_A increases with l_{path} because of the increase of R_{path} and also because of the increase of R_{C2} with l_{gap}.

3.3.6 Contact resistances

The contact resistance R_{C1} is the smallest resistance of the investigated contact resistances, as demonstrated by our KPFM measurements (Fig. 3.8). While R_{C1} results from a strong bonding between the CNT and the TiN, R_{C2} and R_{C3} are rather weak tunneling types of contact [113] between one CNT and the TiN or between two CNTs, respectively. R_{C3} is smaller than R_{C2} for all investigated CNT diameters. Two CNTs that share the same graphene band structure yield a lower potential barrier contact than a CNT with a metal [134]. However, TiN has a high carbon-metal “cohesive strength” when compared , e.g., to gold or palladium [135]. This property is considered responsible of the quality of the carbon-metal contact [135] that, consequently, is expected good for a TiN-CNT contact. Most probably the oxidation of the metal surface adds an oxide barrier between the CNT and the TiN surface, increasing R_{C2}.

3.3.7 Specific contact resistivities

Since the contact resistance is inherently dependent on the contact area, we need to evaluate the specific contact resistivity ρ_C to compare different types of electrical contacts, independent of the contact area. ρ_C is defined as:

$$\rho_C = R_C \times A_C, \tag{3.3}$$

where A_C is the contact area. If we assume for R_{C3} a contact area equal to the square of the CNT diameter, we obtain a specific contact resistivity ρ_{C3} = 14±6 $\Omega\mu$m^2 for a CNT diameter of 30±3 nm and ρ_{C3} = 15±2 $\Omega\mu$m^2 for a CNT diameter of 18±3 nm. In the case of R_{C2} it is more difficult to estimate the contact area, which we assume to be equal to $l_{cont} \times d_{CNT}$, because the contact length is difficult to infer from the SEM images. We therefore focus on the particular contact in Fig. 3.7 (c), which results from a single CNT interconnect in configuration A with an l_{path} of 1.2 μm (not shown in the image). In this case the contact corresponded to a much larger contact area (around 30 × 200 nm^2 = 6000 nm^2) than in a typical case, making it easier to infer its size from the SEM image. The total measured resistance R_A at 0.1 V is in this case 60±1 kΩ i.e. lower than for the results presented in Fig. 3.10 (a) for the same l_{path}, because of the larger contact area. From our data we can infer that R_{path} for an l_{path} of 1.2 μm is 29±9 kΩ/μm × 1.2 μm = 35±11 kΩ. The contact resistance is then given by 60±1 kΩ - 35±11 kΩ = 25±12 kΩ, with a corresponding specific contact resistivity ρ_{C2} = 150±72 $\Omega\mu$m^2. For comparison, the specific contact resistivity of a CNT on a gold-titanium pad was estimated in Ref. [136] to be 600 $\Omega\mu$m^2 and in Ref. [133] to be 1000 $\Omega\mu$m^2.

3.3.8 Breakdown locations

The breakdown of the CNT interconnects under electrical stress sheds further light on the role of the contacts. The power, which is locally produced by Joule heating, varies proportionally to the corresponding local resistance R as I^2R, where I is the current flowing through the CNT. When carrying out electrical measurements up to breakdown conditions (at 2-3 V) [95], CNTs are observed to fail either at the type 2 contact or along the CNTs, most probably near defects present along CNTs grown by CVD [137, 138]. Interestingly, we never observe failure at a type 3 or a type 1 contact. This result confirms that the type 2 contact has the highest local resistance when compared to the other contacts. More details on the CNT breakdown induced by Joule heating are presented in the Chapter 4.

3.3.9 Contacting yield

For configuration B it is possible to grow high density CNTs from opposing electrodes in order to form many CNT-CNT electric contacts in parallel. This way, the total CNT interconnect resistance is reduced when compared to the case of growth from one electrode only (configuration A) since the higher resistance CNT-metal contacts are replaced with lower resistance CNT-CNT contacts.

Resistance values in the order of 100 Ω for a 200 nm electrode gap are measured for configuration B. Taking into account an R_B value around 25 kΩ, it is possible to estimate the total number of contacts: 25 kΩ/100 Ω = 250. With an electrode tip area (area labeled by a dashed line in Fig. 3.6 (b)) of 0.14 μm^2 and a particle density of 2×10^{11}cm^{-2}, we should be able to grow up to 0.14 μm^2 $\times$ 2×10^{11}cm^{-2} = 280 CNTs per electrode, corresponding to a maximum of 280 CNT-CNT contacts. We can therefore conclude that we are able to create high density CNT-CNT contacts with a contacting yield as high as 250/280 = 90%. Note that this is only a rough estimate, since many direct contacts of the CNTs on the opposing TiN electrodes exist in parallel to the CNT-CNT contacts when we consider high density CNT interconnects. For clarity Fig. 3.11 (a) and Fig. 3.11 (b) extend the electric model valid for single CNT interconnects (Fig. 3.9 (b) and Fig. 3.9 (d)) to the case of high density CNT interconnects for configuration A and B, respectively, by defining the following:

- n_a is the total number of contacts in configuration A,
- n_b is the number of direct contacts (CNTs growing from one electrode and reaching the opposing electrode) in configuration B,
- m_b is the number of CNT-CNT contacts in configuration B.

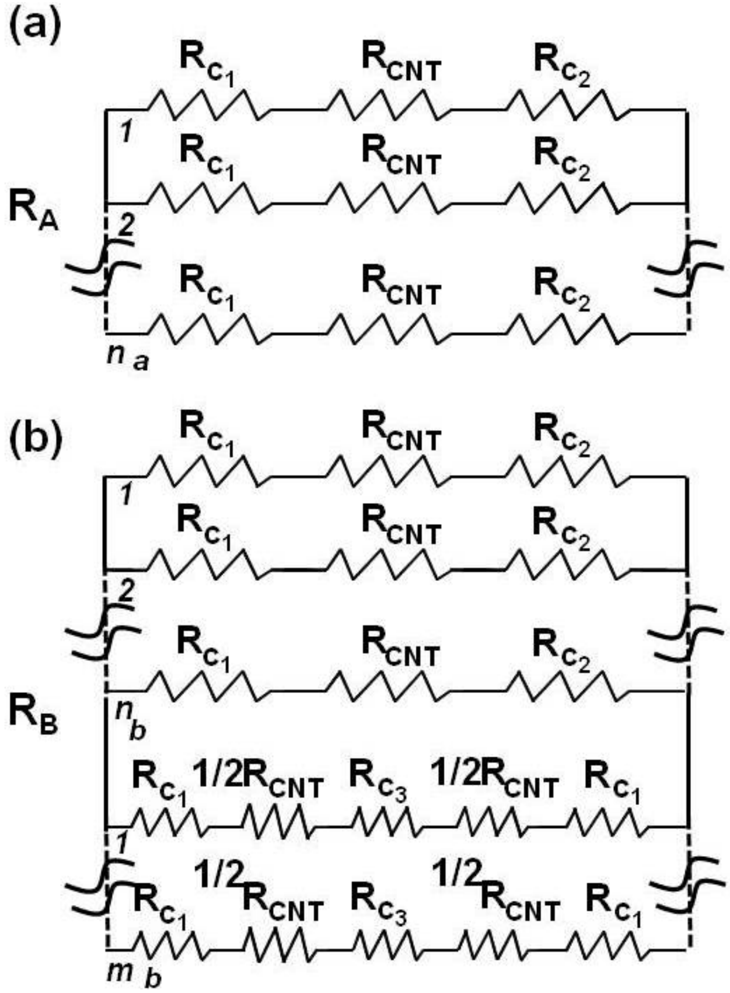

Figure 3.11: Equivalent electric circuits for the resistances of high density CNT interconnects in (a) configuration A and (b) configuration B. R_{path} is the resistance of the CNT conduction path; R_{C1}, R_{C2} and R_{C3} are the type 1 contact resistance, the type 2 contact resistance and the type 3 contact resistance, respectively, as indicated in the SEM images of Figs. 3.7 (a), (c) and (e). n_a is the total number of contacts in configuration A, n_b is the total number of contacts in configuration B and m_b the number of CNT-CNT contacts in configuration B.

3.4 Conclusions

The horizontally suspended CNTs grown with the method described in Chapter 2 were demonstrated to be able to connect electrode gaps up to 5 μm. Lower resistance values are measured for smaller electrode gaps (200-600 nm) both due to a higher number of contacts and an increase in resistance with increasing CNT length. A record low value of 40 Ω is measured in the case of a 200 nm electrode gap for configuration B.

Electrical measurements carried out on low density CNT interconnects allow to evaluate the specific contact resistivity of two CNTs touching each other with their outermost shells. This resistivity of 14±6 $\Omega\mu\text{m}^2$ is one order of magnitude lower than the specific contact resistivity of a CNT touching with its outermost shell the TiN surface (150±72 $\Omega\mu\text{m}^2$).

KPFM imaging of the CNT interconnects prove that the contact resistance of a CNT grown from catalyst particles electrodeposited on the TiN electrodes is much smaller than the resistances of the other two types of contacts.

A CNT-CNT contacting yield of up to 90% is demonstrated in the case of 200 nm electrode gaps for configuration B. This result indicates that the proposed growth method can be very effective in order to form low resistance CNT horizontal interconnects.

3.5 Outlook

In this outlook section we present some preliminary results about the formation of molecular junctions between CNTs and about scanning probe microscopy measurements carried out on in plane CNTs.

3.5.1 Molecular junctions between carbon nanotubes

In all considered cases in this chapter the type 3 contacts are cross-contacts between the CNT outermost shells. However, in few cases we

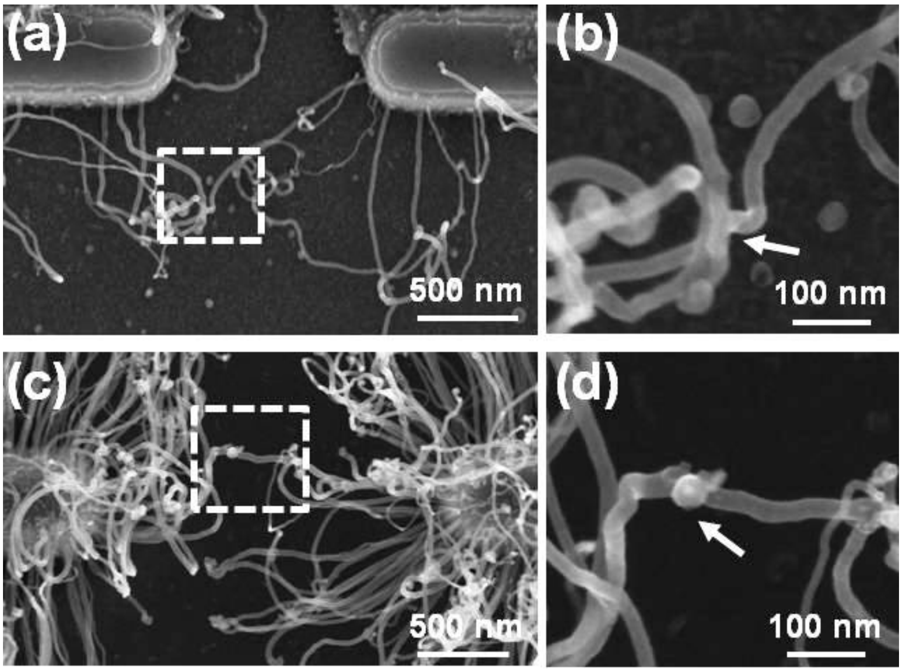

Figure 3.12: (a)-(c) CNTs grown from opposing electrodes and joining in between the electrodes. (b) and (d) are zoomed in images of the regions highlighted by the dashed squares in (a) and (c), respectively.

do observe a joining of the CNTs rather than a CNT-CNT cross-contact. Two examples are presented in Fig. 3.12. The CNTs grow from opposing electrodes (configuration B) and they appear to join in the regions highlighted by dashed squares in Fig. 3.12 (a) and Fig. 3.12 (c), that indicate the position of the zoomed images in Fig. 3.12 (b) and Fig. 3.12 (d), respectively.

From the SEM images it is hard to conclude that joined CNTs create molecular junctions and higher resolution TEM investigations are required. Two CNTs were previously demonstrated to join by electron beam induced welding [105] or current induced Joule heating [104]. Alternatively, junctions between CNTs have been produced by growing CNTs from CNTs [106]. Such contacts may further reduce the interconnect resistance since they should form junctions with a negligible contact resistance [106]. Although our results presented in this chapter demonstrate that the type 3 contact resistance is at this point already sufficiently low to be used for interconnect applications, the possibility to join the CNTs more firmly is of interest to further explore.

3.5.2 Scanning probe microscopy measurements of "in plane" carbon nanotubes

The study of the CNT electronic properties carried out by scanning probe microscopy (SPM) is very important and useful for interconnects and sensor applications. Through such a study it is possible to map the spatial distribution of the electric fields [139] and the charges along the CNTs [140]. However, the SPM approach is quite difficult when investigating the CNTs grown by our method introduced in Chapter 2, due to the pronounced height variations of the structures. CNTs grow in fact suspended from 250 nm thick TiN-SiON electrodes and they bend when their length exceeds 1-2 μm, reaching heights up to 1.4 μm (AFM data).

In Fig. 3.13 we present an example of AFM (Fig. 3.13 (a)) and electrostatic force microscopy (EFM) images (Fig. 3.13 (c)) taken on a sample with 5 μm long and bended CNTs. The EFM potential profile reveals a drop somewhere in between the electrodes (Fig. 3.13 (d)), but the pronounced topography of the CNTs (up to 1.4 μm, Fig. 3.13 (b)) makes it impossible to acquire higher resolution images because the reliable EFM measurements are possible only at large lift heights that exceed the topographic height variations of the CNTs.

In Fig. 3.14 we present an example of SPM images taken on "in plane" CNTs grown by CVD at the University of Cambridge with the method described in Ref. [141]. In particular, in Fig. 3.14 (a) we present a KPFM image taken after charge injection for a 220 μm long SWNT. In Fig. 3.14 (b) we present the AFM image of the region that is labeled in Fig. 3.14 (a) by a dashed square. The substrate is a Si substrate with a 200 nm SiO_2 top layer.

Despite the low magnification of the image, the details of the KPFM image of the ultralong "serpentine" CNT can be clearly recognised. The dark color of the CNT indicates that the delocalisation of the injected

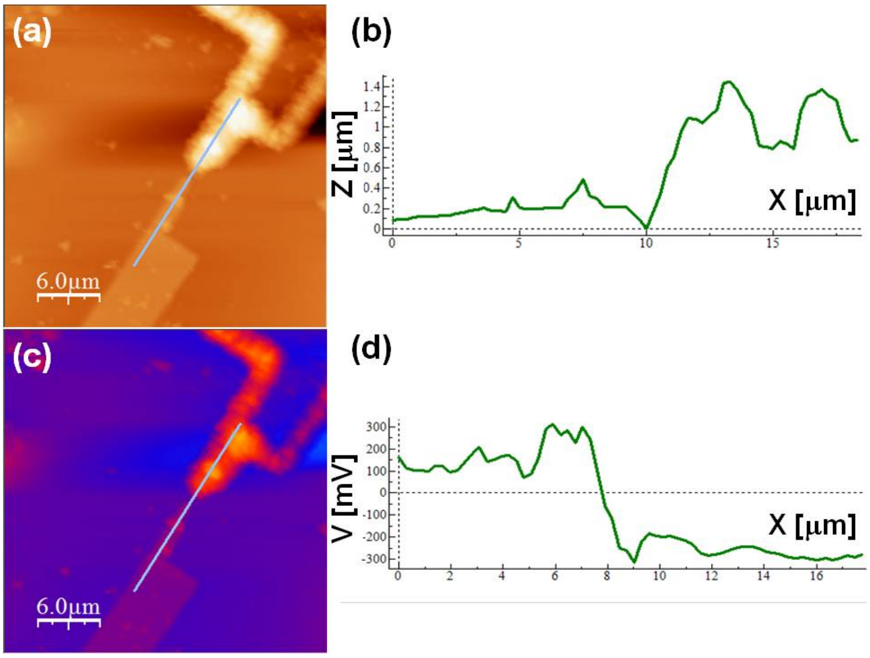

Figure 3.13: Low magnification AFM (a) and EFM (c) images of CNT interconnects for configuration A with CNT lengths around 5 μm. The topographic height Z and the potential profile V presented, respectively, in (c) and (d) are acquired correspondingly to the line drawn in (a) and (c).

charge occurs along the whole length of the 220 μm long SWNT. The potential profile along the white dashed line is shown in the inset of Fig. 3.14 (a). The full width at half minimum (FWHM) of the KPFM signal of the charged CNT is around 400 nm, i.e. considerably wider than the apparent diameter of the SWNT shown in the topography image (inset of Fig. 3.14 (b)). The discrepancy between the KPFM signal and the AFM topography is due to the vertical component of the spatial electrostatic field at a tip-surface distance of 50 nm.

Mapping the electrostatic field distribution above the CNT interconnects provides valuable information about the capacitance between the interconnects and the substrate. However, KPFM measurements without or with charging injection are very challenging to carry out on the CNTs grown by the growth method proposed in Chapter 2, as evidenced by the results of Fig. 3.13. Although suspended CNTs are more suitable

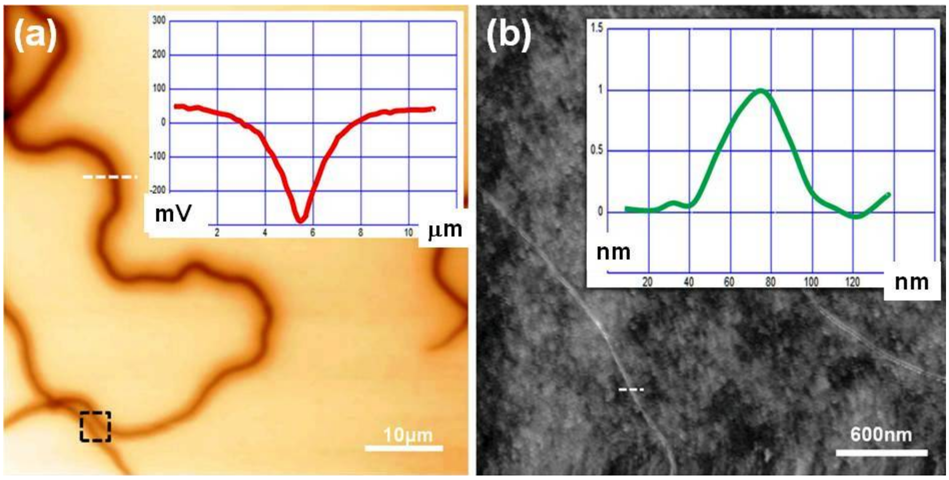

Figure 3.14: (a) KPFM image of a ultralong SWNT after charge injection. The inset in (a) shows the potential profile measured along the white dashed line in (a). (b) AFM image of the region labeled in (a) by a dashed square. The inset in (b) shows the topography profile measured along the white dashed line in (b).

than "in plane" CNTs for applications such as NEMS based sensors, to reliably investigate the properties of CNTs with SPM "in plane" CNTs should be preferred for future investigations.

Chapter 4

Joule Heating Induced Breakdown of Carbon Nanotube Horizontal Interconnects

4.1 Introduction

Beside the electrical properties of CNT interconnects, also their thermal and electro-thermal properties are of great interest for electronics applications and NEMS and sensing applications.

About the electronics applications, the high current densities that the CNTs can carry before breaking down [17] combined with their high thermal conductivity [16] make them interesting, as already discussed, to replace copper interconnects and to reduce the heat-removal issues in CMOS back-end technology [129]. The Joule heating produced by the current flow along the CNTs has been used to improve the electrical contact between the CNTs and the metal electrodes [110, 118, 126] or to create junctions between CNTs [104, 126]. On the other hand, the electrical breakdown of CNTs induced by inhomogeneous Joule heating has been proposed to tailor the diameter of the CNTs and hence also their conductance [142], or to engineer CNT based bearings [143] and switches [144].

About the NEMS and sensing applications, recently, CNTs have been proposed as building blocks for NEMS that convert the thermal energy produced by the current flow along the CNTs into mechanical energy [145–149]. CNTs, with their one-dimensional tubular shape and their concentric shells, offer many advantages for this type of devices: high degree of miniaturization [12], a unique natural track for motion [145], low inter-shell friction [144].

Maximum current densities from 10^6 A/cm^2 [150] to 10^8 A/cm^2 [13] and thermal conductivities from 25-200 W/mK [137, 151] to 3000-3500 W/mK [16, 152] have been measured for CNTs grown by CVD. They have been observed to break down because of inhomogeneous Joule heating at the middle of the CNT [153, 154], at the contact to the metal electrodes [138, 155] or at defect sites [137, 138]. The different results are related to the different quality of the CNTs, the different measurement techniques [16, 156, 157] and the different ways the CNTs have been contacted. Note that in most cases CNTs have been contacted after their growth by lithographic patterning and this may alter their structure and properties when compared to CNTs that have not been treated after their growth [158]. A detailed understanding of the thermal and electrical properties of CNTs grown by CVD is still lacking, while this understanding is essential to be able to use the CNTs for interconnects and NEMS and sensing applications.

In Chapter 2 we introduced a method that allows to selectively place catalyst nanoparticles by electrochemical deposition (ECD) on the sidewalls of TiN electrodes and grow by CVD horizontal CNTs suspended between these electrodes [95, 96]. This method was demonstrated in Chapter 3 to be very powerful to electrically characterise as-grown CNT interconnects without any need for post-growth contacting [96, 159]. In this Chapter we investigate the breakdown of the CNT interconnects induced by Joule heating under atmospheric pressure as well as under high vacuum (10^{-5} mbar) conditions. The ECD described in Chapter 2 to deposit the Ni catalyst particles on the metal electrodes is repeated after CNT growth in order to decorate the CNT interconnects by Ni nanoparticles. The melting of these particles under vacuum after Joule heating induced CNT breakdown reveals that the CNTs reach temperatures exceeding the Ni melting temperature (around 1500 °C). The use of metal nanoparticles to estimate the temperature increase produced by current flow along the CNTs has first been proposed in Ref. [160]. Other techniques used for the same purpose are scanning thermal microscopy [156] and Raman spectroscopy [161]. The ECD decoration technique, relying on electrochemical deposition in combination with our specific electrode configurations [96], allows to selectively deposit Ni particles only on the CNT interconnects. From the breakdown conditions the electrical and thermal properties of the CNT interconnects can be evaluated. A study of the electrical and thermal properties of CNTs by means of their breakdown was carried out before for CNTs produced by arc-discharge [17], by laser condensation at 1200 °C [162] and by CVD at high temperatures [163]. In all cases the CNTs were contacted after their growth. To our knowledge, this is the first time that such a study is performed for CNTs without any post-growth contacting and grown by CVD at lower temperatures (around 600 °C).

The results of this chapter demonstrate that as-grown CNTs are able to carry powers up to 0.6 mW under vacuum, three times higher than under atmospheric pressure, with a maximum current density ranging from 10^6 A/cm^2 up to 10^8 A/cm^2 and a thermal conductivity up to 200 W/mK at room temperature. Our study provides new insight into the electrical characterisation and the electrical breakdown of the CNTs and indicates that the proposed growth method produces CNTs with good properties for interconnects and NEMS applications.

This work was carried out during the third and fourth year of the PhD research activities that are the subject of the present thesis. The research was done at IMEC and at the KULeuven, Laboratory of Solid-State Physics and Magnetism. Part of the results of this work will be submitted for a journal publication.

The first part of the chapter (Section 4.2) describes the methods that were used in addition to the methods already described in the previous chapters: the electrical measurements under vacuum conditions in Section 4.2.1 and the electrochemical decoration of CNTs in Section 4.2.2. In Section 4.3 we discuss the results related to the electrical breakdown of the CNTs (Section 4.3.1), the breakdown locations as inferred from SEM images (Section 4.3.2), the electrochemical decoration of the CNT interconnects for thermal sensing (Section 4.3.3), the electrical and thermal properties as derived from the breakdown conditions of the CNT interconnects under vacuum and atmospheric pressure (Section 4.3.4) and the contact improvement after “electrical stress” under vacuum conditions (Section 4.3.5). The chapter ends with the conclusions in Section 4.4 and the outlook in Section 4.5.

4.2 Materials and Methods

4.2.1 Electrical measurements under atmospheric pressure and high vacuum conditions

Electrical measurements are carried out with the four probe method described in Chapter 3. Here, in order to enable the electrical characterisation of the interconnects under vacuum conditions, a vacuum probe station (Janis cryostat St-100-2DCPRB) is used. Four 12 μm (end diameter) tungsten tips are connected to four source measuring units (SMUs) of a Semiconductor Parameter Analyzer (Agilent 4156C) in a semi-automated microprober system (SUSS Microtech PA300). During the measurements the substrates are maintained at ground voltage and room temperature either under atmospheric pressure or under high vacuum (10^{-5} mbar) conditions. In a typical measurement the voltage is scanned from 0 V up to 5 V at a scan rate of 5 mV/s with voltage intervals of 5 mV.

4.2.2 Electrochemical decoration of carbon nanotubes

For CNT decoration Ni nanoparticles are electro-deposited on the CNTs after their growth using a procedure similar to the procedure used for Ni catalyst deposition (see Chapter 2). A galvanic method (constant current) is used, omitting the reference electrode. In a typical experiment the applied current ranges between -40 mA and -80 mA for deposition times from 0.5 s to 1 s. The current required for Ni deposition as well as the ECD times are higher when compared to the catalyst deposition on the growth test structures due to the increase of the deposition area, which now includes the outermost surface of the CNTs.

4.3 Results and Discussion

4.3.1 Electrical measurements up to breakdown

In Fig. 4.1 we present typical four probe I-V and related R-V measurements carried out up to electrical breakdown for CNT interconnects in configuration A (Fig. 4.1 (a) and Fig. 4.1 (c)) and in configuration B (Fig. 4.1 (b) and Fig. 4.1 (d)) under atmospheric pressure and for electrode gaps ranging from 200 nm up to 5 μm. The CNT diameters are 25±3 nm. The number of CNT interconnects is high and difficult to infer from SEM investigations.

At applied voltages from 2 V up to 4 V the current considerably drops and the resistance increases up to an open circuit state. Note that in Fig. 4.1 (b) and in Fig. 4.1 (d) the curves stop when the breakdown just begins to make the images clear. As discussed in Chapter 3, the resistance increases when increasing the electrode gap due to a lower number of contacts and the increase of the CNT resistance with increasing CNT length. On the other hand, the resistance of the CNT interconnects for configuration A is one order of magnitude higher than the resistance for configuration B. As demonstrated in Chapter 3, this is mostly due to a lower contact resistance of the CNT-CNT contacts, which are present in configuration B, when compared to the resistance of the CNT-metal contacts, which are present in configuration A.

In order to investigate in more detail the breakdown of the CNT interconnects, the number of CNTs connecting the electrodes is reduced by reducing the density of the catalyst nanoparticles deposited by ECD (Chapter 2) and the electrical characterisation is carried out under atmospheric pressure and under vacuum conditions. In Fig. 4.2 we present typical four probe I-V measurements carried out up to breakdown for CNT interconnects in configuration A (Fig. 4.2 (a) and Fig. 4.2 (c)) and in configuration B (Fig. 4.2 (b) and Fig. 4.2 (d)), under atmospheric pressure (Fig. 4.2 (a-b)) and high vacuum (10^{-5} mbar) condi-

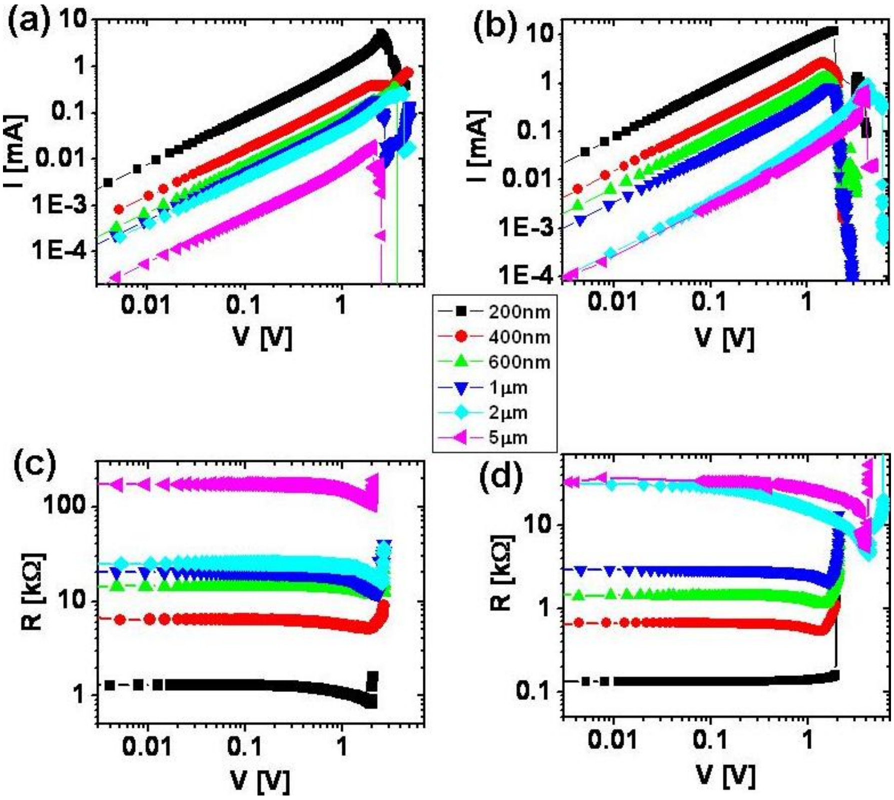

Figure 4.1: Four probe I-V ((a) and (b)) and R-V ((c) and (d)) measurements of CNTs interconnects in configuration A ((a) and (c)) and configuration B ((b) and (d)) for electrode gaps ranging from 200 nm up to 5 μm. The voltage is scanned from 0 up to 5 V at a scan rate of 5 mV/s with voltage intervals of 5 mV at room temperature and under atmospheric pressure.

tions (Fig. 4.2 (c-d)). The CNT diameters are in this case 18±4 nm. The number of CNT interconnects ranges from 1 to 20, depending on the electrode gap and configuration.

When increasing the voltage, the current slightly increases as expected for not perfectly ohmic contacts between CNTs and metal. At applied voltages from 1.5 V up to 3 V the current markedly drops and the resistance significantly increases up to an open circuit state. The CNTs break down due to inhomogeneous Joule heating along their length. The breakdown locations are identified by SEM inspections and are discussed in Section 4.3.2.

In both configurations the current decreases sometimes in a step-like fashion (Fig. 4.2 (c) and Fig. 4.2 (d) but also in [95]). or more gradually like in Fig. 4.2 (b). From literature we know that MWNTs do not break down in the continuous manner typical of electro-migration in metal wires, but via sequential current steps, which indicate the breakdown of individual shells [17]. In our case the steps observed may also correspond to the consecutive breakdown of individual MWNTs interconnecting the electrodes, since only the outermost shells are likely to be conducting. On the other hand, the more continuous variation of the current after breakdown observed in Fig. 4.2 (b) may result from the different contact types.

The CNT interconnects are generally observed to be able to carry higher electrical powers under atmospheric pressure than under vacuum conditions. More details about this aspect and the electrical and thermal properties of the CNT interconnects as inferred from their breakdown conditions are provided in Section 4.3.4.

Before breakdown and at applied voltages ranging from 2 V to 3 V, a sudden increase of current (Fig. 4.2 (c)) from 0.25 mA up to 0.35 mA is observed for configuration A under vacuum. If we stop the measurement and repeat the scan, the resistance appears lowered and coincident to the resistance recorded after the current increase. A similar smooth rise in current has been reported in Ref. [162]. This has been attributed to the structural annealing induced along the CNTs by Joule heating. The CNTs improve their conductance as a result of the thermal annealing produced by the current flow. However, this does not explain the ab-

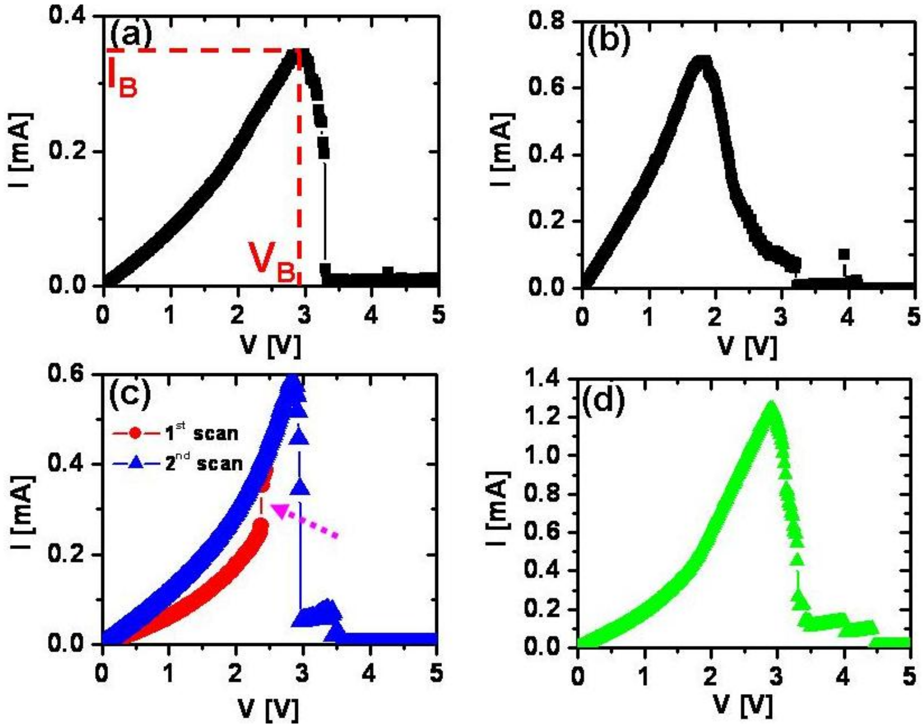

Figure 4.2: Four probe I-V measurements of CNT interconnects: (a) 400 nm electrode gap in configuration A, under atmospheric pressure; (b) 1 μm electrode gap in configuration B, under atmospheric pressure; (c) two consecutive scans for a 1 μm electrode gap in configuration A, under high vacuum conditions (10^{-5} mbar); (d) 1 μm electrode gap in configuration B, under high vacuum conditions (10^{-5} mbar). The voltage is scanned from 0 up to 5 V at a scan rate of 5 mV/s with voltage intervals of 5 mV at room temperature.

sence of such a phenomenon for configuration B and under atmospheric pressure. More details about this resistance improvement are given in Section 4.3.5.

4.3.2 Breakdown locations

In Fig. 4.3 we present some examples of few CNTs interconnecting TiN electrodes in configuration A (Fig. 4.3 (a) and Fig. 4.3 (b), Fig. 4.3 (c) and Fig. 4.3 (d)) and in configuration B (Fig. 4.3 (e) and Fig. 4.3 (f)) before (Fig. 4.3 (a), Fig. 4.3 (c) and Fig. 4.3 (e)) and after (Fig. 4.3 (b), Fig. 4.3 (d) and Fig. 4.3 (f)) the breakdown of CNTs induced by Joule heating. Note that for these examples the ECD potentials range from -1.35 V to -1.4 V in order to deposit low density Ni catalyst nanoparticles (between $10\pm3 \times 10^9$ particles cm^{-2} and $5\pm1 \times 10^{10}$ particles cm^{-2}) and grow low density CNTs. In configuration A (Fig. 4.3 (a)), CNTs grow from one electrode (type 1 contact, indicated in Fig. 4.3 (a), see Chapter 3) and contact the opposing electrode with their outermost shell (type 2 contact, indicated in Fig. 4.3 (a), see Chapter 3). In configuration B (Fig. 4.3 (e)), they grow from both electrodes, interconnecting the electrodes also by a contact between the CNT outermost shells (type 3 contact, indicated in Fig. 4.3 (e), see Chapter 3). In configuration A the CNTs are observed to breakdown at the middle of the CNT (CNT half length, Fig. 4.3 (b)) or closer to the type 2 contact (Fig. 4.3 (d)). In configuration B they break down somewhere along the conduction path formed by the CNTs, most likely at defect sites [137](Fig. 4.3 (f)).

It is well known that the flow of electrical current produces Joule heating along the CNTs. When the CNTs are suspended between two electrodes the heat can be removed only through the contacts to the electrodes if we neglect the heat removal via the surrounding environment [164]. Note that the latter contribution is negligible when we refer to measurements carried out under vacuum while it is more significative when considering measurements carried out under atmospheric pressure. If the two contacts are similar, the heat is equally removed via both of them. The resulting temperature profile along the CNTs is parabolic with the maximum temperature at the CNT half length [164], where the CNTs are observed to break down. In the case of our CNT interconnects the type 1 and 2 contacts in configuration A are electrically

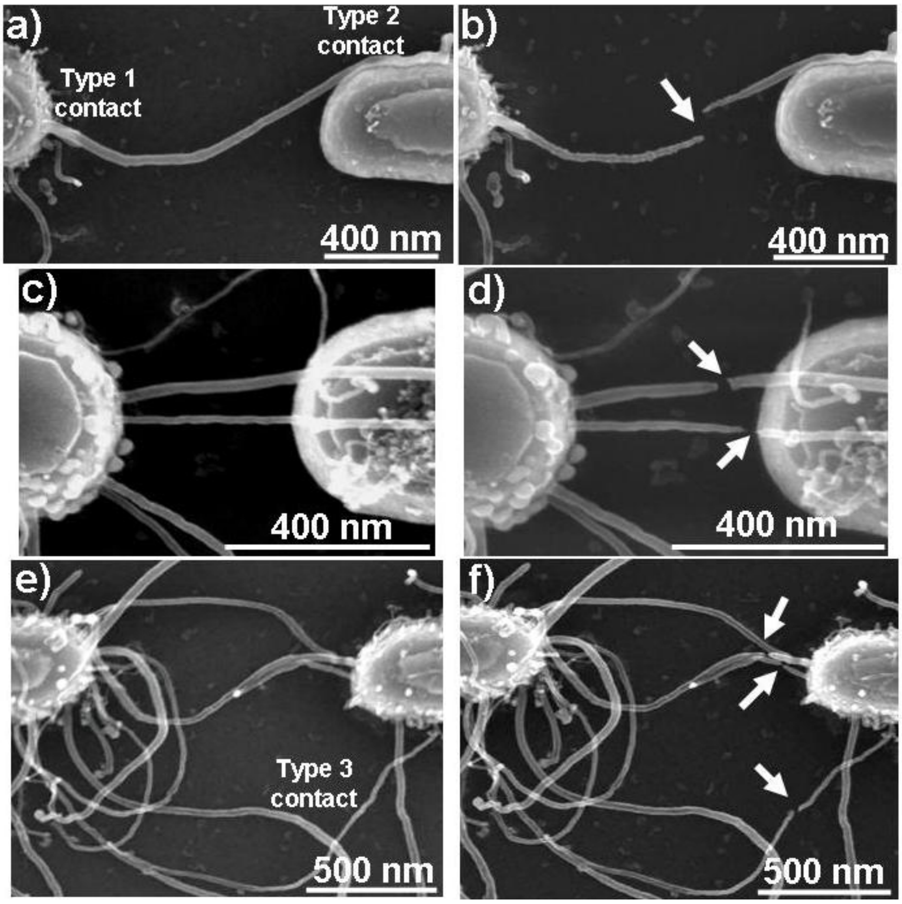

Figure 4.3: SEM top-view images of CNTs interconnecting TiN electrodes in configuration A ((a) and (b), (c) and (d)) and configuration B ((e) and (f)), before ((a), (c) and (e)) and after ((b), (d) and (f)) the breakdown induced by Joule heating. The electrode gaps are 1 μm in (a) and (b),(e) and (f), and 400 nm in (c) and (d). The breakdown locations are marked by arrows. The type 1 and 2 contacts are indicated in (a) for configuration A; the type 3 contact is indicated in (e) for configuration B.

different since the type 2 contact has the highest specific contact resistivity [159] (see Chapter 3). This most likely also corresponds to a difference between the two thermal contact resistances. If the type 2 contact area is large, like in the example of Fig. 4.3 (a), the two contact resistances are more similar, implying that the CNT can remove heat more equally through both of them; the highest temperature is reached at the CNT half length (middle of the electrode gap), where the CNTs are observed to break down (Fig. 4.3 (b)). On the other hand, if the type 2 contact area is small, like in the example of Fig. 4.3 (c), the highest resistive contribution results from the type 2 contacts. The highest temperature is reached in the vicinity of the type 2 contacts, where the CNTs are observed to break down (Fig. 4.3 (d)). In configuration B (Fig. 4.3 (e)) the contacts are more symmetrical because the CNTs grow in a similar way from both opposing electrodes and connect them by type 3 contacts, which are demonstrated to be lowly resistive [159] (see Chapter 3). In this configuration the breakdown locations most likely correspond to defect sites (Fig. 4.3 (f)).

4.3.3 Carbon nanotube decoration for temperature sensing

In order to study the behavior of the CNT interconnects at breakdown, the CNTs are decorated with Ni particles to be used as local thermometers. In Fig. 4.4 (c) we present an example of one CNT interconnect after electrochemical decoration of Ni particles before (Fig. 4.4 (a)) and after (Fig. 4.4 (c)) the electrical measurement carried out under high vacuum (10^{-5} mbar) conditions (Fig. 4.4 (b)). The electrode gap is 600 nm wide. Before the electrical measurement (Fig. 4.4 (a)) a CNT with a diameter of 12 nm connects the two opposing TiN electrodes. The CNT grows from the left electrode (type 1 contact) and contacts the right electrode with its outermost shell (type 2 contact). Eight particles of diameters ranging from 20 to 35 nm decorate the tube. Note that after electrochemical decoration Ni particles are also re-deposited on the electrodes, both connected to the substrate, since this is an example of configuration B. During the electrical measurement (Fig. 4.4 (b)) a first breakdown event is recorded at a current of 0.14 mA and a corresponding voltage of 11 V. A second consecutive electrical scan shows that a contact is still present although the resistance is higher than in the first scan. The final breakdown event is observed at a voltage of 17.5 V and a current of 75 μA. After the electrical measurement the Ni particles appear to have melted and merged into bigger particles. The type 2 contact appears to be improved (dashed arrow), but the CNT interconnect is broken at two locations (Fig. 4.4 (c)).

The sequence of events caused by the current flow is schematically presented in Fig. 4.4 (d-f). Before the electrical measurement (Fig. 4.4 (d)) we distinguish a group of four particles (group of particles 1, GP_1), another group of two particles (group of particles 2, GP_2) and two single particles (particle 1 and particle 2, P_1 and P_2). During the electrical measurement the particles melt and move as indicated by solid arrows in Fig. 4.4 (e). In particular, the groups of particles GP_1 and GP_2 melt and merge because of their close proximity, while the single particles P_1 and P_2 turn around the tube axis. P_2 is also slightly displaced towards the left electrode. After the electrical measurement (Fig. 4.4 (f)) the particle groups GP_1 and GP_2 appear to have merged into two bigger particles with a different shape.

The highest temperature along the CNT interconnect is reached in the region between the middle of the electrode gap and the highly resistive type 2 contact. In this region the groups of particles GP_1 and GP_2 are completely melted, which indicates that the temperature was higher than the Ni melting temperature (1455 °C). On the other hand, the temperature at the type 1 contact is lower since the heat can be removed through a more reliable contact to the electrode. In this region, the particles P_1 and P_2 melt only locally at the interface with the CNT and move around the CNT.

P_2 slightly moves towards the colder left electrode, driven by either the thermal [145, 154] or the electrical gradient [148]. Internal [146, 149] and external [145] loads have been observed to move in a similar way along the CNTs at the current flow.

After the first electrical scan (Fig. 4.4 (b)) the interconnect breaks down probably at the location indicated by “a” in Fig. 4.4 (e). Electrical contact is still present since the second scan records a current flow. This is likely due to a path of melted Ni (grey path indicated by “a” in Fig. 4.4 (e)), which allows electrical continuity but is not clearly

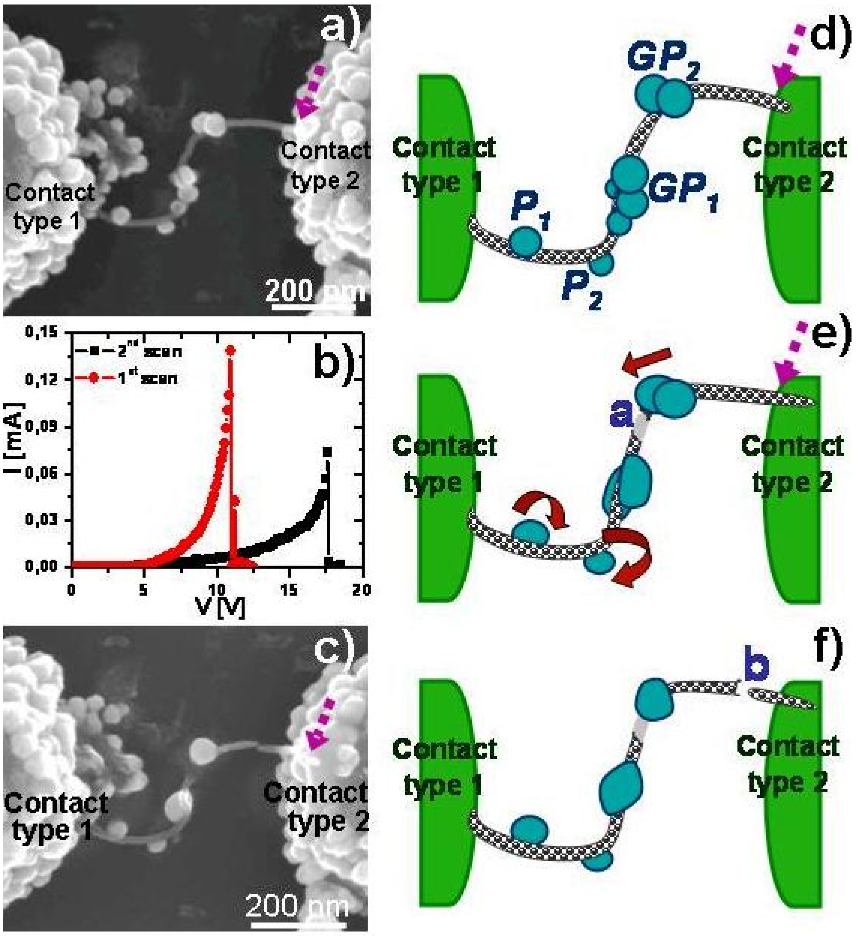

Figure 4.4: (a) SEM top-view image of one CNT interconnect across a 600 nm electrode gap after decoration with electrochemically deposited Ni particles. (b) I-V electrical scans under high vacuum conditions (10^{-5} mbar) promote the improvement of the type 2 contact on the right electrode, the motion, melting and merging of the Ni particles and the breakdown of the CNT interconnect as illustrated by the schematic sequence in (d), (e) and (f). The improvement of the type 2 contact is indicated by a dashed arrow in (a), (c), (d) and (e). The movement of the Ni particles is indicated by entire arrows in (e). The breakdown locations along the CNT interconnects are indicated as “a” in (e) and “b” in (f).

visible in the SEM image of Fig. 4.4 (c). The CNT is observed to move toward the right electrode, corresponding to an improvement of the type 2 contact (dashed arrows in Fig. 4.4 (a), (c), (d) and (e)). This event is not recorded as the sudden increase in current previously discussed (Section 4.3.1), but the current is observed to exponentially increase before the first breakdown event. After the second electrical scan (Fig. 4.4 (b)) the interconnect breaks finally down at the location indicated by b in Fig. 4.4 (f)), close to the type 2 contact. The two breakdown locations also suggest that the highest temperature along the CNT interconnect is reached between the CNT half length (first breakdown location, indicated by “a” in Fig. 4.4 (e)) and the type 2 contact (second breakdown location, indicated by “b” in Fig. 4.4 (f)).

4.3.4 Breakdown power, maximum current density and thermal conductivity

In order to infer the CNT properties from their breakdown conditions, we define the breakdown current (I_B, Fig. 4.2 (a)), as the maximum current that can flow through the CNT interconnects before breakdown of the first contact and the breakdown voltage (V_B, Fig. 4.2 (a)), as the corresponding maximum voltage. The total breakdown power ($P_{B_{tot}}$) is then defined as

$$P_{B_{tot}} = V_B \cdot I_B \ . \tag{4.1}$$

This is the total breakdown power as there are many CNT interconnects in parallel, while the breakdown power of one CNT interconnect (P_B) can be estimated as

$$P_B = \frac{P_{B_{tot}}}{n_{CNT}} = \frac{V_B \cdot I_B}{n_{CNT}} \ , \tag{4.2}$$

where n_{CNT} is the number of CNT interconnects, which is inferred from SEM images.

From the breakdown current it is also possible to estimate the maximum current density (J_{max}) that can flow through as-grown CNT interconnects:

$$J_{max} = \frac{I_B}{n_{CNT} \cdot A_{CNT}} = \frac{I_B}{n_{CNT} \cdot \pi \cdot (d_{CNT}/2)^2} \ , \tag{4.3}$$

where A_{CNT} is the cross section area of one CNT with diameter d_{CNT}.

Finally, if we rely on a diffusive thermal transport model and we assume that the heat is only removed through the contact of the CNTs to the electrodes and not through the surrounding environment, we can estimate the thermal conductivity (k) of as-grown CNTs from their breakdown power [17, 165]:

$$k = \frac{P_B \cdot l_B}{4 \cdot A_{CNT} \cdot \Delta T} = \frac{P_{B_{tot}} \cdot l_B}{4 \cdot n_{CNT} \cdot \pi \cdot (d_{CNT}/2)^2 \cdot \Delta T} \ , \tag{4.4}$$

where l_B is the location where the CNTs are observed to break down (CNT half length for symmetric thermal contacts to the electrodes) and ΔT is the breakdown temperature, defined as the difference between the maximum (at the breakdown location) and the minimum (at the contact to the electrodes) temperature along the CNT interconnect.

In Fig. 4.5 we compare the breakdown power (P_B, Fig. 4.5 (a)), the maximum current density (J_{max}, Fig. 4.5 (b)) and the thermal conductivity (k, Fig. 4.2 (c)) of a single CNT interconnect, estimated according to the Eqs. (4.2), (4.3) and (4.4), under atmospheric pressure and under high vacuum conditions (10^{-5} mbar), for electrode gaps (l_{gap}) ranging from 200 nm up to 5 μm. Each data point is an average of three measurements carried out on interconnects present on the same sample, with a comparable number of CNT interconnects n_{CNT} and electrical resistance for the same electrode gap. Note that we present results of measurements for configuration A. The total breakdown power is generally higher for configuration B than for configuration A, for the same electrode gap and for the same pressure conditions. However, as this difference is mostly due to a higher number of CNT interconnects n_{CNT}, the breakdown power and the breakdown current of a single CNT interconnect are comparable for the two configurations, as well as the maximum current density and the thermal conductivity.

The breakdown power of one CNT interconnect (Fig. 4.5 (a)) decreases from 0.6 mW to 0.1 mW under vacuum and from 0.16 mW to 0.03 mW under atmospheric pressure for electrode gaps increasing from 200 nm to 5 μm. The fitting of the data indicates that the data approximately follow a $P_B \propto (l_{gap})^x$ behavior, with $x \simeq -1/2$, in agreement with previous reports [162, 166]. The decrease of the breakdown power with increasing electrode gap is expected for suspended CNTs, as such

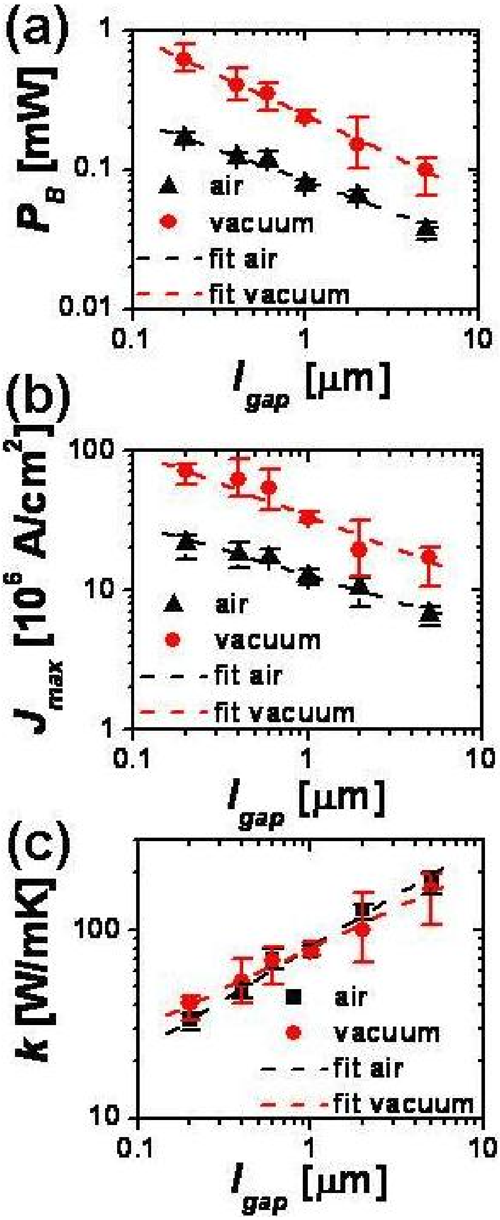

Figure 4.5: Calculated breakdown power (P_B, (a)), maximum current density (J_{max} , (b)) and thermal conductivity (k, (c)) of one CNT interconnect for electrode gaps (l_{gap}) of 0.2, 0.4, 0.6, 1, 2 and 5 μm under atmospheric pressure and under high vacuum conditions (10^{-5} mbar) with the related power law fittings. In the measurements the voltage is scanned from 0 up to 5 V at a scan rate of 5 mV/s with voltage intervals of 5 mV at room temperature. Each data point is an average of 3 measurements.

CNTs mostly release heat via the contact to the electrodes [167].

The breakdown power is estimated to be three times higher under vacuum than under atmospheric pressure for the same electrode gap. This result can have two explanations. If we do not neglect the heat removal via air, we expect that the temperature along the CNTs increases faster under vacuum than under atmospheric pressure. This increase may produce an effect of thermal annealing along the CNTs and increase the current and the corresponding breakdown power under vacuum. On the other hand, if we neglect the heat removal via air, this result proves that the CNT breakdown is mostly an oxidation event [17]. The presence of oxygen is less significative under vacuum than under atmospheric pressure and this allows that the CNTs carry a much higher electrical power before breaking down. Both explanations lead to the conclusion that the CNTs are able to reach temperatures much higher under vacuum than under atmospheric pressure. In particular, the ratio of 3 between the breakdown powers will exist between the breakdown temperatures ΔT.

According to previous reports, CNTs break down under atmospheric pressure at temperatures ranging from 350 °C (breakdown temperature of amorphous carbon [137]) to 700 °C (breakdown temperature of CNTs of high quality, grown by the arc-discharge method [168]). If the breakdown temperature is three times higher under vacuum, it will accordingly range between 1050 °C and 2100 °C. We demonstrated in Section 4.3.3 that the breakdown temperature under vacuum is higher than 1455 °C (Ni melting temperature). As our CNTs are defective because they are grown by CVD we can roughly estimate from these results a breakdown temperature of 500 °C under atmospheric pressure and 1500 °C under vacuum.

The values of the breakdown power are in line with previous reports for suspended CNTs. In Ref. [169] a suspended CNT with a length of 340 nm and a diameter of 20 nm was able to carry powers in the order of 0.15 mW under atmospheric pressure. In Ref. [126] a suspended CNT grown by CVD with a length of about 600 nm and a diameter of 25 nm was able to carry powers of 0.46 mW under vacuum. In Ref. [17] a suspended CNT produced by arc-discharge and deposited on top of prepatterned metal electrodes with a length of around 200 nm and a diameter of 8 nm was able to carry powers of 0.32 mW under atmospheric pressure and of 0.52 mW under vacuum.

The maximum current density (Fig. 4.2 (b)) ranges from 10^8 A/cm^2 to 10^7 A/cm^2 under high vacuum and from $2{\cdot}10^7$ A/cm^2 to $6{\cdot}10^6$ A/cm^2 under atmospheric pressure for electrode gaps increasing from 200 nm to 5 μm. Similar to the results obtained for the breakdown power, CNTs transport maximum current densities three times higher under vacuum than under atmospheric pressure because their breakdown is an event of oxidation of the shells. Note that a similar result was obtained for the maximum current density of CNT-based buckypaper in Ref. [170]. Finally note that this is an evaluation of the maximum current density as limited by Joule heating, while in literature the maximum current density of copper is typically evaluated as limited by electromigration.

The thermal conductivity (Fig. 4.2 (c)) is estimated to vary from 30 up to 200 W/mK for electrode gaps increasing from 200 nm to 5 μm. In the calculations we use breakdown temperatures (ΔT) of 500 °C under atmospheric pressure and 1500 °C under vacuum. Note that this way the thermal conductivity of the CNTs is about the same for measurements under vacuum and under atmospheric pressure conditions. The increase of the thermal conductivity with increasing electrode gaps is in agreement with theory [171] and follows approximately a $k \propto (l_{gap})^x$ power law behavior with $x = 0.42$-0.55. The values of the thermal conductivity are lower than in other reports, probably due to higher thermal contact resistances [172, 173]. Finally note that the estimation of the thermal conductivity relies on a diffusive thermal transport model where we assume that the heat is only removed through the contact of the CNTs to the electrodes and not through the surrounding environment.

If we evaluate the same parameters for the CNT decorated with Ni nanoparticles in Fig. 4.4 by considering the first breakdown event in Fig. 4.4 (b), we obtain 1.54 mW for the breakdown power, $1.2{\cdot}10^8$ A/cm^2 for the maximum current density and 680 W/mK for the thermal conductivity. These values are higher than the values in Fig. 4.5 for a similar sample due to the presence of the Ni particles on top of the CNT. The decorative particles appear to help the heat removal along the CNT and protect the CNT shells from oxidation [145]. This way the breakdown is delayed and both the breakdown power and the maximum current density are higher than in the absence of Ni decoration.

4.3.5 Contact improvement under vacuum

With the aim of understanding the origin of the sudden increase in current when carrying out electrical measurements under vacuum (see Fig. 4.2 (c)), we inspect the interconnects by SEM before and after the electrical measurement. In Fig. 4.6 we show two CNTs interconnecting opposing electrodes for configuration A before (Fig. 4.6 (a) and Fig. 4.6 (c)) and after (Fig. 4.6 (b) and Fig. 4.6 (d)) the electrical measurement carried out under vacuum (inset of (Fig. 4.6 (d)). CNTs are well connected to the electrode they grow from through type 1 contacts (left electrode in (Fig. 4.6 a), while a thin (about 7 nm large) air gap between one CNT and the opposing electrode (right electrode in (Fig. 4.6 a) is visible, corresponding to one of the type 2 contacts (indicated by the solid arrow in Fig. 4.6 (c)). During the electrical measurement a current increase of 0.04 mA is observed and the successive scan reveals a decrease in resistance (inset of Fig. 4.6 d). After the measurement the contacts appear to have improved ((Fig. 4.6 (b-d)). In particular, in Fig. 4.6 (d) the contact indicated by the dashed arrow appears to stick much better on the electrode and the contact indicated by the solid arrow does no longer have the previously observed air gap.

We may explain the above result as follows. The type 2 contacts are not reliable because they do not involve a chemical bonding between CNTs and metal [159]. This is visible in the case of Fig. 4.6 (c) (contact indicated by the solid arrow), where the CNT does not perfectly touch the metal surface, and in other cases where CNTs are observed to be just hanging above the metal electrode (like in the example of Fig. 4.3 (c), as it was confirmed by SEM tilted images, not shown). When a ramped voltage is applied to the CNT interconnects, the CNTs are electrostatically attracted towards the metal electrode, due to their close proximity to it. Once they get close to the metal electrode, the high temperatures reached by Joule heating promote the formation of carbide at the contact level. Consequently the type 2 contact improves and we observe an increase in current. Such an event is not observed for configuration B because most of the contacts are type 3 contacts (contacts between CNTs and not between CNTs and metal). It also does not

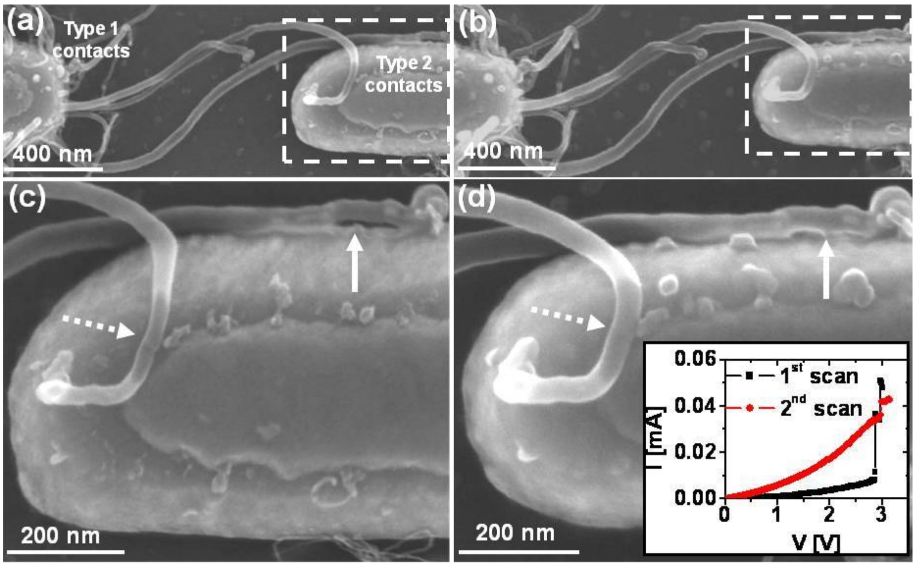

Figure 4.6: SEM top-view images of CNTs interconnecting a 1 μm TiN electrode gap in configuration A before ((a) and (c)) and after ((b) and (d)) the electrical scans in the inset of (d), carried out under high vacuum conditions (10^{-5} mbar). After the electrical scan the contact indicated by a dashed arrow appears to stick much better to the electrode and the contact indicated by a solid arrow does no longer have the previously observed air gap.

happen under atmospheric pressure for two reasons. First, under atmospheric pressure a thin layer of humidity covers the electrodes and allows conduction through the type 2 contacts and at the same time inhibits the electrostatic attraction. Second, CNTs can reach temperatures of the order of 1500 °C under vacuum, while they already break down at temperatures of the order of 500 °C under atmospheric pressure. As the temperature required to form titanium carbonitride (TiCN) is about 1400 °C [174], it follows that TiCN can be formed under vacuum but not under atmospheric pressure. Recently a similar behavior was observed at the contact between a CNT and a tungsten tip in a transmission electron microscope [110]. The Joule heating induced by the current flow caused the structural transformation of the interface between the CNT and the tungsten tip and promoted the formation of tungsten carbide with a consequent improvement of the electrical contact.

4.4 Conclusions

Joule heating induced electrical breakdown was studied for the CNT interconnects grown with the method proposed in Chapter 2. By decorating such interconnects with electrochemically deposited Ni nanoparticles the breakdown temperature reached along the CNTs is estimated to be 500 °C under atmospheric pressure and 1500 °C under high vacuum conditions. The CNT interconnects are demonstrated to be able to carry powers up to 0.6 mW under vacuum, three times higher than under atmospheric pressure, with a maximum current density between 10^7 and 10^8 A·cm^{-2} and a thermal conductivity up to 200 W/mK at room temperature. Before electrical breakdown under vacuum, improvements of the type 2 contacts are recorded and explained in terms of electrostatic attraction of the CNTs to the electrodes and consequent formation of titanium carbonitride. Our results prove that as-grown CNTs have appropriate properties for interconnects and NEMS applications where, e.g., the mechanical actuation is induced by thermal gradients generated by the flow of electrical current.

4.5 Outlook

In this outlook section we present some preliminary results that require further investigation about the merging of CNTs induced by Joule heating.

4.5.1 Merging of carbon nanotubes induced by Joule heating

In Fig. 4.7 we present an example of CNT interconnects for configuration A before (Fig. 4.7 (a)) and after (Fig. 4.7 (b) and Fig. 4.7 (c)) the electrical breakdown recorded in Fig. 4.7 (d). During the electrical scan and before the breakdown sudden increases of current are recorded as indicated by the arrows in Fig. 4.7 (d). At a voltage of about 5 V a first breakdown event is observed and is followed by another conduction ramp (between 5 and 7 V) and other consecutive breakdown events in a step-like fashion.

The breakdown locations are not easily identified because the breakdown probably happens at the CNT-metal contact and the tubes do not break and remain sticking on the SiON surface (Fig. 4.7 (c)). One of the connecting CNTs moves towards another CNT, as indicated by the arrows in Figs. 4.7 (a) and (b). One of the current increases in Fig. 4.7 (d) is probably related to this electrostatic motion. At the location indicated in Fig. 4.7 (c) by the dashed arrow the three CNT interconnects appear to be strongly bundled. It is hard to conclude from the SEM images wether or not they create a chemical bond. Two CNTs were previously demonstrated to join by electron beam induced welding [105] or current induced Joule heating [104]. In both cases the joining was induced by the local formation of defects (vacancies, interstitial sites) typically already present in CNTs grown by CVD. The formation of such contacts may explain the increases of current observed during the electrical measurements. Moreover, this result points to the possibility to form new types of CNT morphologies (CNT X junctions in this case) by Joule heating effects and should be further investigated by in situ TEM analysis.

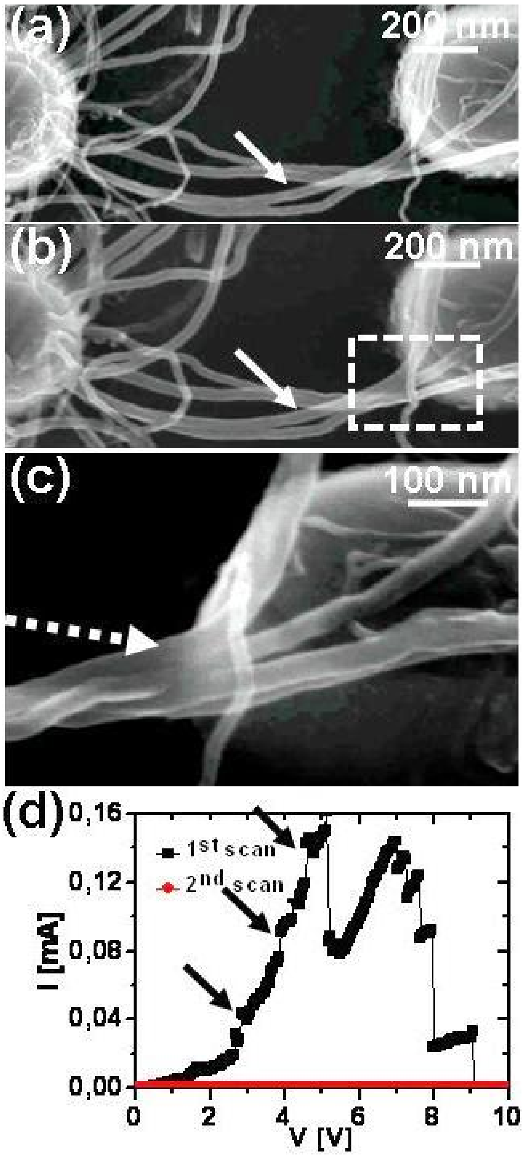

Figure 4.7: CNT interconnects in configuration A before (a) and after (b) and (c) the electrical breakdown recorded in (d). The arrows in (a) and (b) indicate the electrostatic motion of one contacting CNT towards another one after the electrical measurement. The image in (c) is an SEM tilted view of the area indicated by a dashed rectangle in (b). It highlights the region where the CNTs appear to bundle and locally merge as a result of the Joule heating produced by the current flow. The sudden increases of current observed during the electrical measurement before breakdown are indicated by arrows in (d).

Chapter 5

Excitation of the Mechanical Resonances of Carbon Nanotubes loaded with Nickel Particles

5.1 Introduction

CNT electromechanical resonators have been proposed as radio frequency electric field sensors (radio transmitter/receiver) [175] because the amplitude of their oscillations strongly varies with the frequency of the electric field when close to the resonance conditions. CNT resonators have also been proposed as mass sensors [176] and gas sensors [177] because the resonance conditions (frequency, amplitude, quality factor) are strongly dependent on the presence of an extra mass on the CNT resonator as well as on the surrounding environment.

The resonators can be excited by means of an alternating electrical signal (excitation signal) brought close to the CNT by an antenna gate [178, 179]. The frequency of this electrical excitation signal has to range between hundreds of MHz and GHz, depending on the geometrical parameters of the CNT [178]. Another possible method to excite the

CNT resonance is to apply a high DC voltage between the tip of a singly clamped CNT and an electrode in close proximity [180]. In this case the voltage needs to be on the order of 100 V since it has to promote the field emission from the CNT tip [180].

Unfortunately, the CNT growth structures presented in this thesis (Chapter 2) are designed for DC applications (CNT interconnects) rather than for AC applications. First, they do not contain a gate electrode that can bring the high frequency electrical excitation signal close to the CNTs. Such gate could be defined using electron beam lithography before growing the CNTs. However, its design is challenging because it needs to be adapted to make it compatible with a high frequency transmission line. Second, the metal electrodes the CNTs grow from are too thick and not appropriate for AC measurements. Their large thickness can shield the electrical excitation signal from the antenna gate and make it ineffective.

In a configuration where the CNTs do not contact the opposing electrode but remain suspended with their tips in close proximity to the opposing electrode, the CNT resonance could be excited by a high DC voltage applied between the electrodes similar to the approach in Ref. [180]. However, the measurement of the resonance frequency would not be straightforward in this case. It requires the use of an ultra-high vacuum chamber [180] and of a well designed measurement apparatus to achieve a high signal-to-noise ratio [181]. The reason is that the measurement in this case is based on the electrical detection of the high frequency component of the field emitted from the CNT tip [180].

The oscillations and the resonance conditions of the CNT oscillator can be detected using different approaches. A first approach is to use an AFM [182]. In this case the amplitude of the electrical excitation signal has to be modulated at a frequency equal to one of the resonance frequencies of the AFM cantilever [183, 184]. Another approach is to measure the change of the CNT resistance when sweeping the electrical excitation signal frequency [178, 179]. The CNT is piezoresistive and its resistance reaches a minimum at its resonance frequency [178, 179]. Finally, the CNT resonance can also be measured by electrically [181] or optically [185] detecting the high frequency component of the field emitted by the CNT tip while oscillating.

This chapter describes a novel method that does not require the use of an electric excitation signal to induce the mechanical resonances of suspended CNTs. Our method resembles the magnetic resonance force microscopy (MRFM) technique [25, 26]. MRFM is an imaging technique based on the detection of the force gradient induced by a sample under magnetic resonance which is attached to the AFM cantilever [25, 26]. Correspondingly, the proposed method relies on the excitation of a magneto-mechanical force gradient induced by a external inhomogeneous magnetic field on CNTs loaded with Ni nanoparticles (Ni-CNTs) that are under ferromagnetic resonance. Such method is more advantageous than the traditional electrical excitation because it does not require the fabrication of high frequency structures (high frequency gates, microstrips). Moreover, the resonance frequency of the Ni-CNTs is within a convenient range of tens of MHz, as an additional mass is added to the tip of the CNT oscillator [27]. The resonances of the Ni-CNTs are detected by AFM because the measurement is carried out on singly clamped CNTs. However, the resonance can also be detected by measuring the electrical resistance of the Ni-CNTs when they interconnect two opposing electrodes, as described in the Chapter 3.

The results described in this chapter demonstrate that it is possible to grow CNTs loaded with big (about 90 nm in diameter), i.e. ferromagnetic Ni particles by simply increasing the density of the ECD catalyst particles. Second, the obtained results demonstrate that the force experienced by the Ni particle spins immersed in a magnetic field that varies in space and in time is able to drive the Ni-CNTs into oscillation up to their resonance. Finally, the results prove that the Ni-CNT resonance frequencies detected by AFM are in good agreement with the theoretical estimates and that the quality factor and consequently also the amplitude of the oscillations are sensitive to the presence of helium gas in the surrounding environment.

This work was carried out at the Laboratory of Solid-State Physics and Magnetism of the KULeuven and the results will be submitted for publication in the near future.

The first part of the chapter (Section 5.2) describes the used materials and methods, i.e. the growth of Ni-CNTs in Section 5.2.1 and the method to excite and detect the mechanical resonances of the Ni-

CNTs in Section 5.2.2. In Section 5.3 we present the results related to the growth of the Ni-CNTs (Section 5.3.1) and the detection of their mechanical resonances and related quality factors and oscillation amplitudes under atmospheric conditions and in a helium gas environment (Section 5.3.2). The chapter ends with the conclusions (Section 5.3.3) and the outlook (Section 5.3.4).

5.2 Materials and Methods

5.2.1 Growth of carbon nanotubes loaded with Ni particles

Nickel catalyst particles are electrodeposited on TiN using the method described in Chapter 2. In a typical experiment a constant electrochemical potential of the order of -3 V is applied for 1 s. Next, CNTs are grown by CVD in a 20/200/1000 sccm of $C_2H_2/H_2/Ar$ gas flow at 8 Torr and a temperature of 640 °C for 3 minutes.

5.2.2 Magnetic excitation and atomic force microscopy detection of the mechanical resonances of carbon nanotubes loaded with Ni particles

A schematic view of the excitation and detection setup is presented in Fig. 5.1. The related excitation signals are presented in Fig. 5.2. A permanent magnet M_p is placed close to the sample in order to produce a constant polarizing magnetic field B_p (Fig. 5.2 (a)). This field allows to align the Ni particle spins. Its value is in the order of 60 mT. A small coil L_μ (2 mm in diameter) is placed nearby in order to generate a microwave frequency (f_μ) magnetic field B_μ (Fig. 5.2 (f)) perpendicular to B_p. This field allows to induce the magnetic resonance of the Ni particles [186]. Its frequency f_μ is in the order of 1.82 GHz. Finally, in order to generate a force that couples the magnetic resonance of the Ni particles to the mechanical resonance of the Ni-CNTs, a magnetic field gradient needs to be generated [186, 187]. The gradient is created by a small permanent magnet M_∇ that produces a spatially inhomogeneous

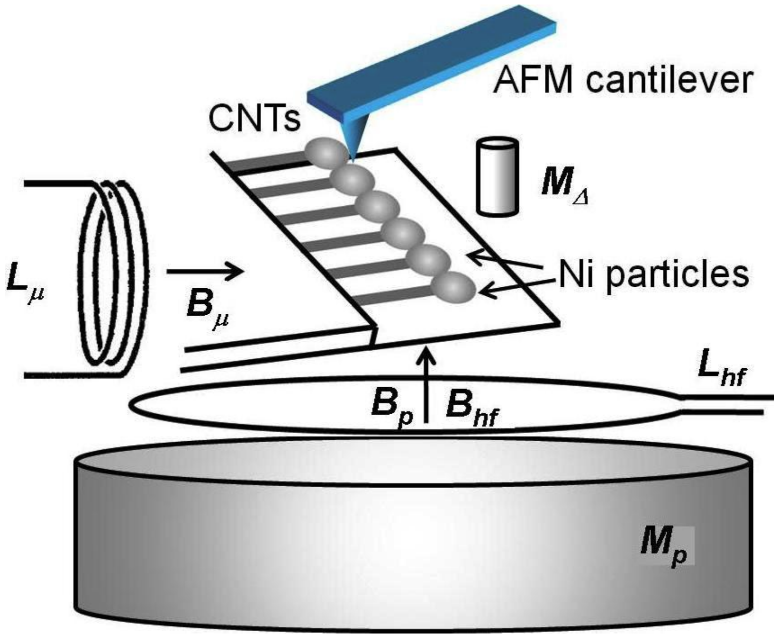

Figure 5.1: Schematic of the setup for the excitation and detection of the magneto-mechanical resonances of Ni-CNTs.

magnetic field (magnetic field gradient, ∇B). A time dependent magnetic field component is created by a coil L_{hf} that generates a high frequency (f_{hf}) magnetic field (B_{hf}, Fig. 5.2 (b)). The frequency f_{hf} is adjusted in the range of the mechanical resonance frequency of the Ni-CNTs (MHz). Note that B_{hf} modulates the constant polarizing magnetic field B_p as illustrated in Fig. 5.2 (c).

The force experienced by the Ni particle spins immersed in a magnetic field that varies in space (∇B) and in time (B_{hf}) cyclically inverts the Ni particle spins and drives the Ni-CNTs into an oscillation with an amplitude of a few nanometers. When the frequency of the magnetic field B_{hf} approaches the mechanical resonance frequency of the Ni-CNTs, the amplitude of their oscillations (A) becomes large with an amplification factor proportional to the quality factor Q of the Ni-CNT oscillator. The AFM tip is positioned above the Ni-CNT array in order to detect its mechanical oscillations. The tip is not able to follow so fast oscillations (in the range of the MHz) [183, 184]. The solution is to modulate in amplitude (AM) the field B_{hf} by a signal with a fre-

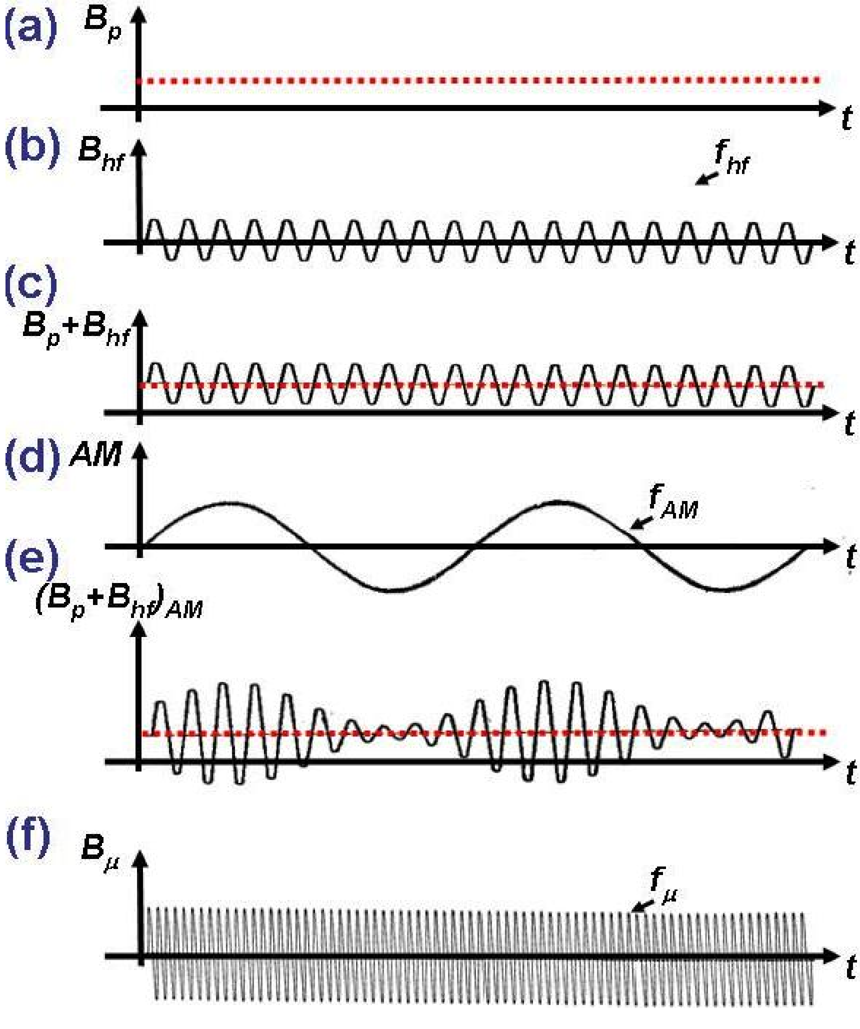

Figure 5.2: Schematic presentation of the different signals applied in the setup of Fig. 5.1.

quency (f_{AM}) equal to one of the resonance frequencies of the AFM cantilever (in the range of tens of kHz) [183, 184]. The AM signal is plotted in Fig. 5.2 (d), while the signal resulting from the AM modulation of B_p+B_{hf} is shown in Fig. 5.2 (e). This way, a signal generated by the nonlinear force-distance dependence between the cantilever tip and the Ni-CNT array and dependent on the amplitude of the oscillations can be detected [183, 184]. In particular, similarly to Refs. [183, 184], the imaging of the Ni-CNT oscillations is done at the fundamental resonance frequency of the cantilever ($f_{AM} = f_{cant1} = 60kHz$), whereas the second resonance frequency of the cantilever is used to provide standard AFM operation and topography imaging. The AFM operates in dynamic mode with a set point adjusted to minimize the parasitic forces applied on the Ni-CNTs by the AFM cantilever [183]. The measurements are performed under atmospheric conditions as well as in a helium gas environment.

5.3 Results and Discussion

5.3.1 Growth of carbon nanotubes loaded with Ni particles

In Fig. 5.3 (a) we show an SEM image of the catalyst particles deposited on the TiN sidewalls. The high electrochemical potentials applied for long times enable the deposition of high density ($\sim 10^{12}$ cm^{-2}) and big ($\sim$ 100 nm in diameter) particles that form a film rather than remaining as separate particles. Next, Ni-CNT arrays are grown by CVD from the deposited catalyst film as illustrated in the SEM images of Fig. 5.3 (b) and Fig. 5.3 (d) and in the schematic view of Fig. 5.3 (e). The CNTs grow underneath the catalyst layer that is lifted off from the TiN sidewalls resulting in a “tip growth process”. As such, the CNTs remain horizontal and freestanding with length l_{CNT} and loaded with Ni particles with diameter d_{Np} at their tips.

In Chapter 2 a preferential CNT “base growth” was observed by TEM inspection (Fig. 2.15), although catalyst particles were found also at the tip and along the CNTs (Fig. 2.16). The growth of CNTs underneath the Ni film suggests that the CNT nucleation is promoted on

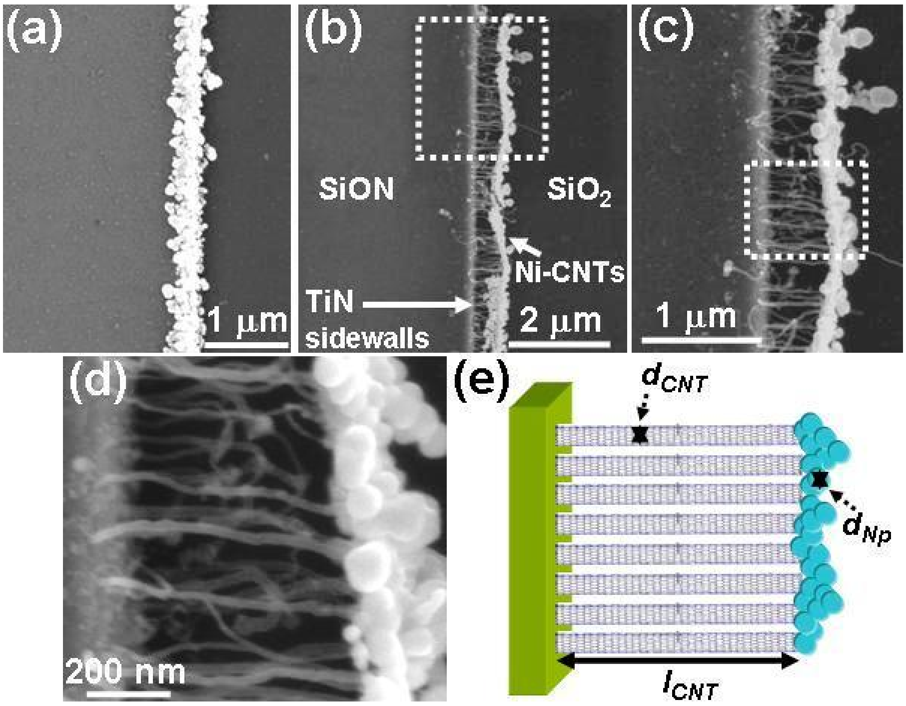

Figure 5.3: (a) SEM image of the Ni catalyst film deposited on the TiN sidewalls by applying a constant electrochemical potential of -3 V for 1 s. (b) Low and ((c) and (d)) higher magnification views of Ni-CNT arrays grown by CVD from the deposited catalyst film. (e) Schematic view of the Ni-CNT array.

the bottom Ni surface rather than on the top Ni surface [188]. The oxidation of the Ni top surface is likely the reason for its inactivity in the catalysis. The bottom Ni surface is protected from oxidation and is able to catalyze the CNT growth.

5.3.2 Mechanical resonances of carbon nanotubes loaded with Ni particles

In Fig. 5.4 we show the topographic AFM image (Fig. 5.4 (a)) and the corresponding image of the oscillations (Fig. 5.4 (b)) under atmospheric conditions. Note that the sample region is the one shown in the SEM image of Fig. 5.3 (c). The topographic image reveals that the CNTs

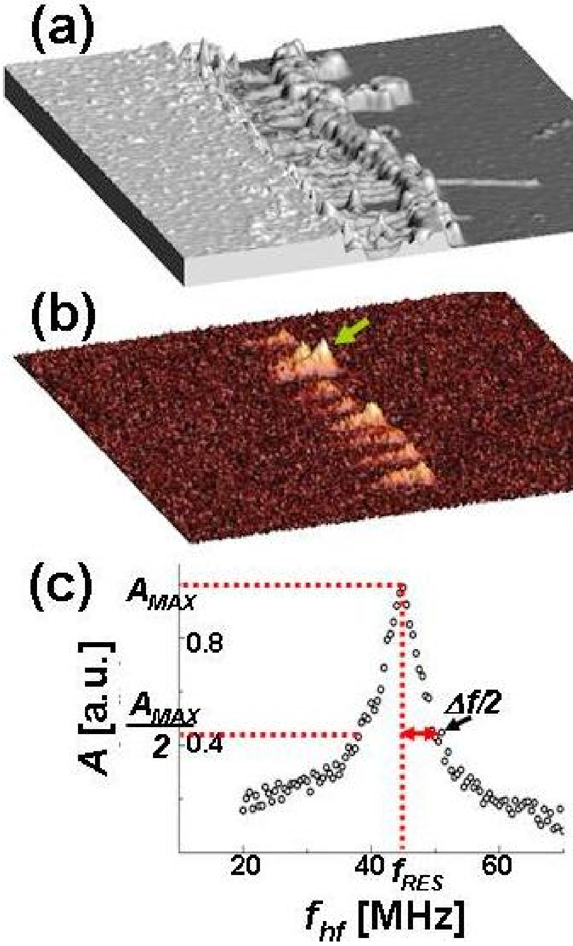

Figure 5.4: 3.75×3.75 μm^2 (a) topographic AFM image and (b) corresponding oscillation image of the Ni-CNT array under atmospheric conditions. (c) Resonance curve obtained for the Ni-CNT indicated by the arrow in (b). f_{hf}=45 MHz; B_μ = 60 mT; f_μ= 2 GHz.

form an uniform array parallel to the substrate with Ni particles clearly visible at their tips. The oscillation image contains a color contrast that reflects the amplitude of the oscillations A of the Ni-CNTs. Such contrast is maximized by tuning f_{hf} in order to reach the resonance condition for the majority of the Ni-CNTs in the array. Note that the most pronounced contrast appears at the free tips of the Ni-CNTs while a few Ni-CNTs are kept together by the Ni deposit at their tips and the amplitude of their oscillations is considerably smaller and not detectable.

In Fig. 5.4 (c) we show the resonance curve (oscillation amplitude versus f_{hf}) obtained for the Ni-CNT indicated by the arrow in Fig. 5.4 (b). The resonance occurs at a frequency f_{RES} of 45 MHz. The quality factor of an oscillator Q is defined as the ratio between the frequency f_{RES} and the half-bandwidth Δf/2 indicated in Fig. 5.4 (c) (half width of the resonance curve when the oscillation amplitude is at half the maximum amplitude A_{MAX}). For the Ni-CNT indicated by the arrow in Fig. 5.4 (b) Q is around 8.

If we model the Ni-CNT as a cylindrical elastic beam with an additional mass concentrated at its end, its fundamental resonance frequency f_{RES} can be expressed as [189]

$$f_{RES} = \sqrt{\frac{3\pi E d_{CNT}^4}{64 l_{CNT}^3 (m_{Np} + 0.24 m_{CNT})}}\ , \tag{5.1}$$

where E is the Young modulus of the CNT, d_{CNT} is the CNT diameter (Fig. 5.3 (e)), l_{CNT} is the CNT length (Fig. 5.3 (e)), m_{Np} is the mass of the Ni particles at the CNT tip and m_{CNT} is the CNT mass.

In Fig. 5.5 (a) we show the resonance frequencies measured with the setup in Fig. 5.1 and the related resonance frequencies calculated according to Eq. (5.1). The chart in Fig. 5.5 (a) is a 3D-diagram plotted in normalised coordinates of $d_{Np}^{-3/2}$ and $l_{CNT}^{-3/2}$. The resonance frequencies refer to the set of 11 Ni-CNT samples shown in Fig. 5.5 (c) with the geometrical parameters listed in Fig. 5.5 (d). For the same set of samples the measured quality factors are presented in Fig. 5.5 (b).

The graph in Fig. 5.5 (a) reveals a strong dependence of the resonance frequencies on the geometric parameters of the CNTs and the masses of the Ni particles, as predicted by the Eq. (5.1). On the

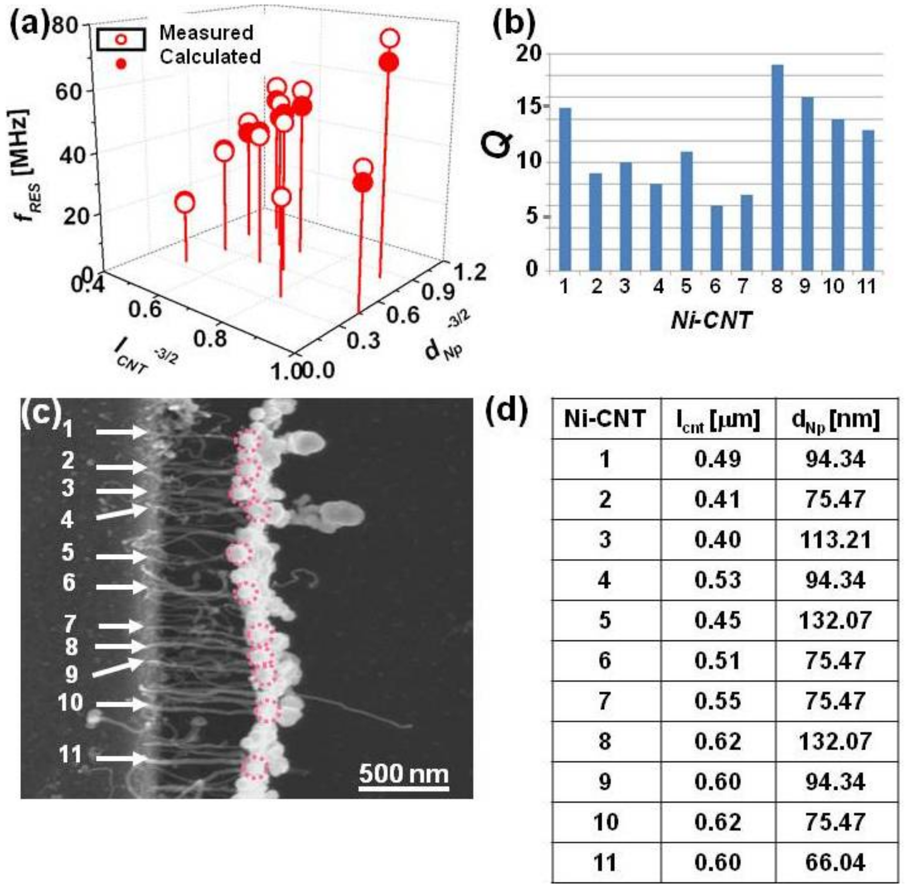

Ni-CNT	l_{cnt} [μm]	d_{Np} [nm]
1	0.49	94.34
2	0.41	75.47
3	0.40	113.21
4	0.53	94.34
5	0.45	132.07
6	0.51	75.47
7	0.55	75.47
8	0.62	132.07
9	0.60	94.34
10	0.62	75.47
11	0.60	66.04

Figure 5.5: (a) Theoretical and measured values of the resonance frequencies and (b) quality factors of the Ni-CNT samples indicated in (c) with the geometrical parameters listed in (d).

other hand, the different geometries of the oscillators are responsible for the different amplitude of the oscillations of different Ni-CNTs in Fig. 5.5 (b). The calculated resonance frequencies turn out to be in good agreement with the measured values. For example, we measure for the Ni-CNT 4 a resonance frequency of 45 MHz and calculate a resonance frequency of 43 MHz. For this CNT the corresponding Young modulus is about 90 GPa. Note that in the calculations we have assumed that the Ni particles have a spherical shape and that $m_{Np} \gg m_{CNT}$.

In Fig. 5.6 we compare the oscillation image for the above considered

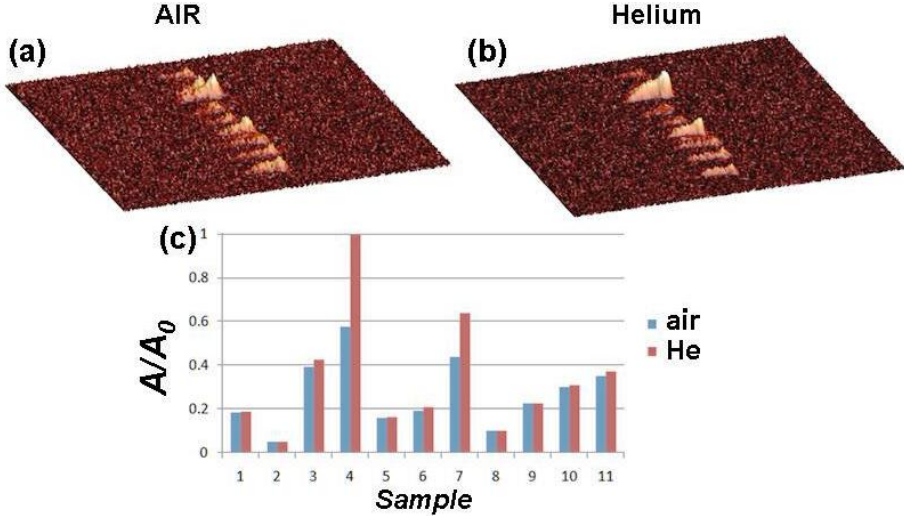

Figure 5.6: Oscillation images taken at an excitation frequency f_{hf}=45 MHz under (a) atmospheric conditions and (b) He-gas environment. (c) Normalized amplitudes of oscillations of the individual Ni-CNTs measured under atmospheric conditions and He gas environment.

Ni-CNT array under atmospheric conditions (Fig. 5.6 (a)) and helium gas environment (Fig. 5.6 (b)). The contrast present in Fig. 5.6 (b) is much higher than in Fig. 5.6 (a). This result indicates that the amplitude of the oscillations is larger under He gas environment than under atmospheric conditions as further confirmed by the chart in Fig. 5.6 (c). The latter summarizes the values of the oscillation amplitudes A normalised with respect to the maximum amplitude A_0 for the 11 Ni-CNTs of Fig. 5.5 (c) under atmospheric conditions and in helium gas environment. The difference in the oscillation amplitude is evident for the two environments, in particular for the samples number 4 and 7. Note that also the quality factor is higher in helium gas environment than under atmospheric conditions with a ratio of about 2, while the resonance frequency only slightly (by about 2%) increases (results not shown).

These results are consistent with the results of Ref. [190] that discusses the effects of temperature, pressure and environment on the resonance of microcantilevers. It is known that the quality factor of an oscillator as well as the amplitude of its oscillations are dependent on the gas environment, on the oscillator geometry, on the system internal friction and on the distance of the oscillator from the substrate. Nevertheless, it is still not clear which effect is dominant. In our case the increase of A/A_0 and of Q under He environment demonstrates that the gas environment has an important influence on the resonance conditions of an oscillator. In particular, this influence is mainly related to the viscosity of the gas environment [191]. The presence of helium favors the slip of the molecules present in the surrounding environment on the cantilever with a corresponding decrease of the viscosity when compared to the case of normal atmospheric conditions. As such, the oscillator is able to oscillate with larger amplitudes and corresponding higher quality factors.

Note that the proposed configuration of Ni-CNT arrays is advantageous for sensing applications. The Ni-CNTs form a long and uniform array of mechanical resonators with a corresponding increase of the number of sensors on the same substrate, i.e. the sensing statistics improves.

5.3.3 Conclusions

A new method to excite CNT-based mechanical resonators has been described. The method relies on the excitation of the ferromagnetic resonance of Ni particles present at the tips of suspended CNTs (Ni-CNTs). This method is advantageous in cases where the traditional electric/electrostatic excitation methods are not effective or cannot be implemented.

The Ni-CNTs are demonstrated to mechanically resonate under atmospheric conditions in a convenient range of radio frequencies of the order of tens of MHz, with reasonably high quality factors ranging from 6 to 19. Such resonators are demonstrated to be suitable for sensing applications as they reveal an increase of the quality factor of around 2 and, correspondingly, larger oscillation amplitudes under helium environment due to the decrease of the environment viscosity.

5.3.4 Outlook

CNT-based resonators are well known as atomic-resolution mass sensors [176, 177]. Sensitivity to masses as light as a few attograms has been reported for this type of sensors. As such, it would be interesting to test in the future the resonance response when a mass is added to the Ni-CNT resonators.

The power of the proposed growth technique is based, *inter alia*, on the possibility to tailor the geometrical parameters of as-grown CNTs. In the framework of the CNT mechanical characterisation it would be interesting to tailor the resonance response of the oscillators by changing their geometrical parameters, e.g. the CNT length as well as the Ni particle mass/size.

Finally, the role of factors other than the viscosity of the environment on the change of the quality factor when the system is under helium or different gas environment should be further investigated. Important results could come out from measurements carried out under vacuum conditions and under different gas pressure.

Conclusions

In this thesis we discussed some relevant problems related to the fabrication of surface plasmon resonance (SPR) sensors and carbon nanotube (CNT) based sensors and proposed some possible solutions to these problems.

Regarding the SPR sensors, a novel SPR sensor built on lithium niobate (LN) optical waveguides is proposed in **Part I** (**Chapter 1**). This sensor is studied and designed by numerical simulations with a module composed of a mode-matching solver and a three dimensional coupling matrices propagator. The results of our study reveal that the SPR always occurs at refractive index values between 1.8 and 2 when varying some of the design parameters such as LN-cut, wavelength of the input light, gold film thickness and length. The minimum resonance index with a good sensitivity of the sensor is achieved for a wavelength of 633 nm on a LN z-cut waveguide where a 50 nm thick and 2 mm long gold film is deposited. The resonance index is in this case around 1.8 and this sensor may be useful to analyse high index oxides or polymer films. Note that the variation of the SPR resonance with the thickness of the layers just above the sensing structure points towards another possible application of this sensor: as monitor of the thickness or of the adsorption of thin films.

The introduction of a matching layer of suitable thickness and refractive index in between the gold layer and the analyte allows us to tune the resonance index. In particular, a resonance index of 1.3 can be achieved with a matching layer of thickness 36 nm and refractive index 2.2. The resultant sensor looses sensitivity because the evanescent field, which is able to enter into the analyte is only a small fraction of the entire evanescent field. However, this sensor is now able to analyse aqueous solutions.

We conclude that our results described in **Part I** of this thesis demonstrate that for SPR sensors the resonance occurs at refractive indices that are strictly dependent on the refractive index of the substrate. However, it is always possible to tune the resonance index towards the desired values by adding a matching layer with appropriate thickness and refractive index between the metal film and the analyte layer. This approach can be extended to produce multi-analyte integrated sensors not only on lithium niobate but also on different optical crystals.

Regarding the CNT sensors (**Part II**), the conclusions of this thesis are more generally related to CNT electrical interconnects applications. As it was pointed out in the introduction, the most promising CNT sensors are electrical sensors. As such, the issues to be addressed for CNT sensor production are similar to the ones faced by the semiconductor industry to produce CNT electrical interconnects.

A novel method to grow CNT horizontal interconnects was proposed in **Chapter 2**. This method makes use of electrochemical deposition (ECD) to selectively deposit Ni catalyst nanoparticles on the sidewalls of metal electrodes. A high control over the density (up to 3×10^{11} particles cm^{-2}) and average size (15-30 nm) of the catalyst particles is demonstrated. This control is directly translated into a similar control over the CNT density and diameter. Horizontally suspended CNTs are grown by chemical vapor deposition (CVD) from one titanium nitride (TiN) electrode towards the opposing electrode or from both opposing electrodes. CNTs grown by this method present high quality multi-walled graphitic structure (transmission electron microscopy results) and they have a Raman D/G ratio of 0.6. These results indicate that these CNTs are of the highest quality that can be obtained using thermal CVD.

The results described in **Chapter 3** confirmed that the horizontally suspended CNTs grown with the method proposed in Chapter 2 are able to connect electrode gaps up to 5 μm. Lower resistance values are measured for smaller electrode gaps (200-600 nm) due to both a higher number of contacts and the increase in resistance with the CNT length. A record low value of 40 Ω is measured in the case of a 200 nm electrode gap and CNTs grown from both opposing electrodes. Electrical measurements carried out on low density CNT interconnects allow to evaluate the specific contact resistivity of two CNTs touching each other with their outermost shells. This resistivity of the order of 14 $\Omega\mu\text{m}^2$ is one order of magnitude lower than the specific contact resistivity of a CNT touching with its outermost shell the TiN surface (around 150 $\Omega\mu\text{m}^2$). Kelvin probe force microscopy imaging of the CNT interconnects proves that the contact resistance of a CNT grown from Ni catalyst particles electrodeposited on the TiN electrodes is much smaller than the resistances of the above described two types of contacts. A CNT-CNT contacting yield of up to 90% is demonstrated in the case of 200 nm electrode gaps and CNTs grown from both opposing electrodes. This result indicates that the proposed growth method may be effective in order to form low resistance CNT horizontal interconnects.

In **Chapter 4** the breakdown of the CNT interconnects induced by Joule heating effect was studied. By decorating such interconnects with electrochemically deposited Ni nanoparticles the breakdown temperature reached along the CNTs is estimated to be as high as 1500 °C under high vacuum conditions. The CNT interconnects are demonstrated to be able to carry electrical powers up to 0.6 mW under vacuum, three times higher than under atmospheric pressure, with a maximum current density between 10^7 and 10^8 $\text{A}\cdot\text{cm}^{-2}$ and a thermal conductivity up to 200 W/mK at room temperature. Before electrical breakdown under vacuum, improvements of the contacts are recorded and explained in terms of electrostatic attraction of the CNTs towards the electrodes and consequent formation of titanium carbonitride.

Finally, in **Chapter 5** a new method to excite CNT-based mechanical resonators is described. The method relies on the excitation of ferromagnetic resonance of Ni particles that are present at the tips of suspended CNTs (Ni-CNTs). This method is advantageous in cases where traditional electric/electrostatic based excitation methods are not effective or cannot be implemented. The Ni-CNTs are demonstrated to mechanically resonate under atmospheric conditions in a convenient range of radio frequencies of the order of tens of MHz, with reasonably high quality factors ranging from 6 to 19. Such resonators may be suitable for sensing applications as they reveal an increase of the quality factor by a factor of 2 and, correspondingly, larger oscillation amplitudes under helium environment, due to a decrease of the environment viscosity.

We conclude that the results described in **Part II** of this thesis demonstrate that the proposed CNT growth method allows to routinely grow CNT horizontal interconnects with good electrical, thermal and mechanical properties. Moreover, this method may be used to fabricate reliable CNT electrical interconnects, nanoelectromechanical systems (NEMS) and sensing devices.

Outlook

Possible future developments related to the work presented in this thesis were already described in the outlook sections at the end of each chapter and are briefly summarised in this section.

Regarding **Part I** of the thesis, we suggest to implement the proposed surface plasmon resonance (SPR) sensor on a y-waveguide in order to soften the requirements related to the laser source stability. Some first results concerning the design of low loss y-waveguides were presented in Section 1.6. Moreover, in order to improve the sensitivity of the SPR sensor we propose to electro-optically modulate the substrate refractive index in order to improve the signal-to-noise ratio [45, 53–55] and to investigate alternative SPR configurations such as ridge waveguides [56] and waveguides where the metal layer is constituted by metal particles. Both configurations allow to increase the sensitive surface [57] and, consequently, the sensitivity of the SPR sensor.

Regarding **Part II** of the thesis, the different aspects of the work concerning carbon nanotube (CNT) based interconnects and sensors (growth, electrical, thermal, mechanical and sensing characterisation) may have different future developments.

Concerning the CNT growth, we find that repeating the process of electrochemical deposition (ECD) and chemical vapor deposition (CVD) described in **Chapter 2** can provide an effective approach to grow new carbon based molecular junctions such as y- and x-junctions. The proposed approach and some preliminary results have been described in detail in the outlook Section 2.5.

The CNT bending observed for CNTs longer than 2 μm may be studied in more detail in order to clarify its cause and solve it, as this phenomenon can be a major problem when considering CNTs for long horizontal interconnects. A possible solution could be to fabricate slightly different growth test structures. For example, structures with thick electrodes (on the order of the CNT length we want to obtain) may extend the CNT horizontal alignment because the curvature of the electrode sidewalls would be proportionally reduced.

With regard to the contact properties of CNTs, which were electrically characterised in **Chapter 3**, we suggest to further investigate such contacts by transmission electron microscopy (TEM) analysis. Some scanning electron microscopy (SEM) images presented in the outlook Section 3.5 appeared to reveal a joining of the CNTs at the CNT-CNT contact level, but it is hard to conclude that we are dealing with a real merging of the tubes rather than with a simple contact. Although the results of the chapter demonstrate that the contact between two CNTs has a resistance that is sufficiently low to be used for interconnect applications, the possibility to join the CNTs more firmly is interesting and requires further investigation.

With regard to the scanning probe microscopy (SPM) approach used in **Chapter 3** to qualitatively investigate the CNT electrical interconnects, we highlighted the difficulty to do reliable SPM measurements on the suspended CNTs grown by our method. As discussed in the outlook Section 3.5, the pronounced topography of the growth structures (250 nm electrode thickness) as well as the CNT bending reduce the resolution of the SPM images and the information we can obtain from them. Where possible, we then recommend to use the SPM approach for in-plane CNTs.

With regard to the Joule heating of the CNT interconnects that was studied in **Chapter 4**, we suggest to further investigate with in-situ TEM analysis the possibility to join two CNTs by electrically induced heating. The formation of such junctions would provide the unique possibility to form new types of CNT morphologies (CNT x-junctions in this case) and would be of interest for further investigation since from the SEM images shown in the outlook Section 4.5 it is hard to conclude wether or not the CNTs join.

With regard to the Ni particle decoration used in **Chapter 4** to estimate the temperature profile along the CNTs, we believe that this approach has also great potential for nanoelectromechanical system (NEMS) applications where, for example, the mechanical actuation is induced by thermal gradients generated by the flow of electrical current. As briefly discussed in Section 4.3.3 some of the particles appear to move along the current carrying CNT driven either by a thermal [145, 154] or an electrical gradient [148]. We suggest to further study this thermally induced particle movement along CNT interconnects.

Finally, with regard to the CNT-based resonators described in **Chapter 5**, we suggest to test the resonance response when an extra mass is added to the resonator and when the geometrical parameters of the resonator, e.g. the CNT length or the Ni particle mass/size are tailored. These resonators may show extraordinary sensitivities as mass sensors [176, 177] and their mechanical properties may be better tested when varying their geometrical properties. Moreover, we suggest to further investigate the role of parameters other than the viscosity of the environment on the change of the resonator quality factor when the system is under helium gas environment. Important results may come out from measurements carried out under vacuum conditions and under different gas pressures.

Bibliography

[1] Yueh-Min Ray Huang, *Sensors*, Vol. 21 of *Advancements in Modeling, Design Issues, Fabrication and Practical Applications*, springer ed. (PUBLISHER, ADDRESS, 2008).

[2] K. Kalantar-zadeh and B. Fry, *Nanotechnology-Enabled Sensors*, springer ed. (PUBLISHER, ADDRESS, 2008).

[3] G. E. Moore, Mos Transistor as an Individual Device and in Integrated Arrays, Ieee Spectrum **2**, 49 (1965).

[4] A. Vaseashta and D. Dimova-Malinovska, Nanostructured and nanoscale devices, sensors and detectors, Science and Technology of Advanced Materials **6**, 312 (2005).

[5] J. Homola, S. S. Yee, and G. Gauglitz, Surface plasmon resonance sensors: review, Sensors and Actuators B-Chemical **54**, 3 (1999).

[6] N. Sihna, J. Ma, and J. T. W. Yeow, Carbon Nanotube-based Sensors, Journal of Nanoscience and Nanotechnology **6**, 573 (2006).

[7] J. Oh, Y. W. Chang, H. J. Kim, S. Yoo, D. J. Kim, S. Im, Y. J. Park, D. Kim, and K. H. Yoo, Carbon Nanotube-Based Dual-Mode Biosensor for Electrical and Surface Plasmon Resonance Measurements, Nano Letters **10**, 2755 (2010).

[8] C. Y. Kuo, C. L. Chan, C. Gau, C. W. Liu, S. H. Shiau, and J. H. Ting, Nano temperature sensor using selective lateral growth of carbon nanotube between electrodes, Ieee Transactions on Nanotechnology **6**, 63 (2007).

[9] Yoo K. P., Lim L. T., Min N. K., Lee M. J., Lee C. J., and Park C. W., Novel resistive-type humidity sensor based on multiwall car-

bon nanotube/polyimide composite films, SENSORS AND ACTUATORS B-CHEMICAL **145**, 120 (2010).

[10] Hu P. A., Zhang J., Li L., Wang Z. L., O'Neill W., and Estrela P., Carbon Nanostructure-Based Field-Effect Transistors for Label-Free Chemical/Biological Sensors, SENSORS **10**, 5133 (2010).

[11] B. Mahar, C. Laslau, R. Yip, and Y. Sun, Development of carbon nanotube-based sensors - A review, Ieee Sensors Journal **7**, 266 (2007).

[12] M. S. Dresslhaus, G. Dresslhaus, and P. Avouris, *Carbon Nanotubes synthesis, structure, properties and applications* (Springer, ciao, 2001), pp. 1–100.

[13] H. J. Li, W. G. Lu, J. J. Li, X. D. Bai, and C. Z. Gu, Multichannel ballistic transport in multiwall carbon nanotubes, Physical Review Letters **95**, 086601/1 (2005).

[14] Z. Yao, C. L. Kane, and C. Dekker, High-field electrical transport in single-wall carbon nanotubes, Physical Review Letters **84**, 2941 (2000).

[15] M. M. J. Treacy, T. W. Ebbesen, and J. M. Gibson, Exceptionally high Young's modulus observed for individual carbon nanotubes, Nature **381**, 678 (1996).

[16] P. Kim, L. Shi, A. Majumdar, and P. L. McEuen, Thermal transport measurements of individual multiwalled nanotubes, Physical Review Letters **87**, 1 (2001).

[17] P. G. Collins, M. Hersam, M. Arnold, R. Martel, and P. Avouris, Current saturation and electrical breakdown in multiwalled carbon nanotubes, Physical Review Letters **86**, 3128 (2001).

[18] N. Srivastava, R. V. Joshi, and K. Banerjee, Carbon nanotube interconnects: implications for performance, power dissipation and thermal management, International Electron Devices Meeting 2005 (IEEE Cat. No.05CH37703C) 4 pp.—CD (2005).

[19] J. Robertson, Growth of nanotubes for electronics, Materials Today **10**, 36 (2007).

[20] A. Romo Negreira, P. M. Vereecken, C. M. Whelan, and K. Maex, Nucleation and Growth Study of Nickel Nanoparticles on Silicon, ECS Transactions **2**, 409 (2007).

[21] A. Romo-Negreira, D. J. Cott, A. S. Verhulst, S. Esconjauregui, N. Chiodarelli, J. E. Weis, C. M. Whelan, G. Groeseneken, M. Heyns, S. De Gendt, and P. M. Vereecken, in *MRS Spring meeting* (PUBLISHER, San Francisco - CA, 2008), Vol. 1079E.

[22] A. Romo-Negreira, O. Richard, S. De Gendt, K. Maex, M.M. Heyns, and P. M. Vereecken, Science Advanced Materials **1**, 86 (2009).

[23] A. Romo-Negreira, D. J. Cott, S. De Gendt, K. Maex, M. M. Heyns, and P. M. Vereecken, Electrochemical Tailoring of Catalyst Nanoparticles for CNT Spatial-Dimension Control, Journal of the Electrochemical Society **157**, K47 (2010).

[24] M. Fujihira, Kelvin probe force microscopy of molecular surfaces, Annual Review of Materials Science **29**, 353 (1999).

[25] J. A. Sidles, J. L. Garbini, K. J. Bruland, D. Rugar, O. Zuger, S. Hoen, and C. S. Yannoni, Magnetic-Resonance Force Microscopy, Reviews of Modern Physics **67**, 249 (1995).

[26] P. E. Wigen, M. L. Roukes, and P. C. Hammel, Ferromagnetic resonance force microscopy, Spin Dynamics in Confined Magnetic Structures Iii **101**, 105 (2006).

[27] K. Kim, K. Jensen, and A. Zettl, Tuning Nanoelectromechanical Resonators with Mass Migration, Nano Letters **9**, 3209 (2009).

[28] B. Liedberg, C. Nylander, and I. Lundstrom, Surface-Plasmon Resonance for Gas-Detection and Biosensing, Sensors and Actuators **4**, 299 (1983), rz304 Times Cited:636 Cited References Count:0.

[29] J. Homola and M. Piliarik, *Surface Plasmon Resonance (SPR) Sensors* (Springer, ADDRESS, 2006), Vol. 4.

[30] O. A. Plaksin, Y. Takeda, H. Amekura, N. Umeda, K. Kono, N. Okubo, and N. Kishimoto, Optical monitoring of nanoparticle formation during negative 60 keV Cu ion implantation into LiNbO3, Applied Surface Science **241**, 213 (2005).

[31] S. Shandilya, M. Tomar, K. Sreenivas, and V. Gupta, Temperature Dependent Optical Properties of c axis Oriented LiNbO3 Thin Film Using Surface Plasmon Resonance, Journal of Lightwave Technology **28**, 3004 (2010).

[32] J. Homola, Present and future of surface plasmon resonance biosensors, Analytical and Bioanalytical Chemistry **377**, 528 (2003).

[33] B. Liedberg, C. Nylander, and I. Lundstrom, Biosensing with Surface-Plasmon Resonance - How It All Started, Biosensors & Bioelectronics **10**, R1 (1995).

[34] C. Nylander, B. Liedberg, and T. Lind, Gas-Detection by Means of Surface-Plasmon Resonance, Sensors and Actuators **3**, 79 (1982).

[35] J. Homola, J. Ctyroky, M. Skalsky, J. Hradilova, and P. Kolarova, A surface plasmon resonance based integrated optical sensor, Sensors and Actuators B-Chemical **39**, 286 (1997).

[36] J. Dostalek, J. Ctyroky, J. Homola, E. Brynda, M. Skalsky, P. Nekvindova, J. Spirkova, J. Skvor, and J. Schrofel, Surface plasmon resonance biosensor based on integrated optical waveguide, Sensors and Actuators B-Chemical **76**, 8 (2001).

[37] C. R. Lavers, K. Itoh, S. C. Wu, M. Murabayashi, I. Mauchline, G. Stewart, and T. Stout, Planar optical waveguides for sensing applications, Sensors and Actuators B-Chemical **69**, 85 (2000).

[38] R. Levy, A. Peled, and S. Ruschin, Waveguided SPR sensor using a Mach-Zehnder interferometer with variable power splitting ratio, Sensors and Actuators B-Chemical **119**, 20 (2006).

[39] R. Kashyap and G. Nemova, Surface plasmon resonance-based fiber and planar waveguide sensors, Journal of Sensors **2009**, 1 (2009).

[40] A. Busacca, M. Cherchi, L. Oliveri, C. Santini, S. Riva-Sanseverino, A. Parisi, S. Guarino, A. Cino, S. Stivala, L. Colace, and G. Assanto, in *Gruppo Elettronica* (PUBLISHER, Ischia (IT), 2006).

[41] K. K. Wong, *Properties of Lithium Niobate* (Institution of Engineering and Technology, ADDRESS, 2002).

[42] C. Santini, M. Cherchi, C. Giaconia, S. Riva-Sanseverino, A. Parisi, S. Guarino, and A. Cino, in *7th Symposium of European Vacuum Coaters* (PUBLISHER, Anzio (IT), 2007).

[43] S. Maier, *Plasmonics: Fundamentals and Applications* (Springer, ADDRESS, 2007).

[44] B. D. Gupta and R.K. Verma, Surface plasmon resonance-based fiber optic sensors: principle, probe designs, and some applications, Journal of Sensors **2009**, 1 (2009).

[45] T. J. Wang, W. S. Lin, and F. K. Liu, Integrated-optic biosensor by electro-optically modulated surface plasmon resonance, Biosensors & Bioelectronics **22**, 1441 (2007).

[46] S. Grilli, P. Ferraro, P. De Natale, B. Tiribilli, and M. Vassalli, Surface nanoscale periodic structures in congruent lithium niobate by domain reversal patterning and differential etching, Applied Physics Letters **87**, (2005).

[47] A. S. Sudbo, Problems in Vector Mode Calculations for Dielectric Wave-Guides, Linear and Nonlinear Integrated Optics **2212**, 26 (1994).

[48] A. S. Sudbo, Numerically Stable Formulation of the Transverse Resonance Method for Vector Mode-Field Calculations in Dielectric Wave-Guides, Ieee Photonics Technology Letters **5**, 342 (1993).

[49] A. S. Sudbo, Why Are Accurate Computations of Mode Fields in Rectangular Dielectric Wave-Guides Difficult, Journal of Lightwave Technology **10**, 418 (1992).

[50] A. S. Sudbo, Mode Conversion and Filtering of Bound Modes in Planar Wave-Guide Bragg Reflectors, Journal of Lightwave Technology **8**, 927 (1990).

[51] M. A. Ordal, L. L. Long, R. J. Bell, S. E. Bell, R. R. Bell, R. W. Alexander, and C. A. Ward, Optical-Properties of the Metals Al, Co, Cu, Au, Fe, Pb, Ni, Pd, Pt, Ag, Ti, and W in the Infrared and Far Infrared, Applied Optics **22**, 1099 (1983).

[52] A. Parisi, A. C. Cino, A. C. Busacca, M. Cherchi, and S. Riva-Sanseverino, Integrated Optic Surface Plasmon Resonance Measurements in a Borosilicate Glass Substrate, Sensors **8**, 7113 (2008).

[53] X. Ma, X. L. Xu, Z. Zheng, K. Wang, Y. L. Su, J. F. Fan, R. Zhang, L. S. Song, Z. Y. Wang, and J. S. Zhu, Dynamically modulated intensity interrogation scheme using waveguide coupled surface plasmon resonance sensors, Sensors and Actuators a-Physical **157**, 9 (2010).

[54] K. Wang, Z. Zheng, Y. L. Su, Z. Y. Wang, L. S. Song, and J. S. Zhu, Hybrid differential interrogation method for sensitive surface plasmon resonance measurement enabled by electro-optically tunable SPR sensors, Optics Express **17**, 4468 (2009).

[55] T. J. Wang and C. W. Hsieh, Phase interrogation of localized surface plasmon resonance biosensors based on electro-optic modulation, Applied Physics Letters **91**, (2007).

[56] T. J. Wang, C. W. Tu, and F. K. Liu, Integrated-optic surface-plasmon-resonance biosensor using gold nanoparticles by bipolarization detection, Ieee Journal of Selected Topics in Quantum Electronics **11**, 493 (2005).

[57] D. H. Wan, H. L. Chen, Y. T. Lai, C. C. Yu, and K. F. Lin, Use of Reversal Nanoimprinting of Nanoparticles to Prepare Flexible Waveguide Sensors Exhibiting Enhanced Scattering of the Surface Plasmon Resonance, Advanced Functional Materials **20**, 1742 (2010).

[58] K.B.K. Teo, C. Singh, M. Chhowalla, and W.I. Milne, Catalytic synthesis of carbon nanotubes and nanofibers, Encyclopedia of Nanocience and Nanotechnology **1**, 665 (2004).

[59] J. Kong, N. R. Franklin, C. W. Zhou, M. G. Chapline, S. Peng, K. J. Cho, and H. J. Dai, Nanotube molecular wires as chemical sensors, Science **287**, 622 (2000).

[60] H. J. Dai, E. W. Wong, and C. M. Lieber, Probing electrical transport in nanomaterials: Conductivity of individual carbon nanotubes, Science **272**, 523 (1996).

[61] A. P. Graham, G. S. Duesberg, R. V. Seidel, M. Liebau, E. Unger, W. Pamler, F. Kreupl, and W. Hoenlein, Carbon nanotubes for microelectronics?, Small **1**, 382 (2005).

[62] N. Chiodarelli, K. Kellens, D. J. Cott, N. Peys, K. Arstila, M. Heyns, S. De Gendt, G. Groeseneken, and P. M. Vereecken, Integration of Vertical Carbon Nanotube Bundles for Interconnects, Journal of the Electrochemical Society **157**, K211 (2010).

[63] P. Avouris, J. Appenzeller, R. Martel, and S. J. Wind, Carbon nanotube electronics, Proceedings of the Ieee **91**, 1772 (2003).

[64] A. Guo, Y. Y. Fu, C. Wang, L. H. Guan, J. Liu, Z. J. Shi, Z. N. Gu, R. Huang, and X. Zhang, Two-bit memory devices based on single-wall carbon nanotubes: demonstration and mechanism, Nanotechnology **18**, (2007).

[65] P. A. Williams, S. J. Papadakis, M. R. Falvo, A. M. Patel, M. Sinclair, A. Seeger, A. Helser, R. M. Taylor, S. Washburn, and R. Superfine, Controlled placement of an individual carbon nanotube onto a microelectromechanical structure, Applied Physics Letters **80**, 2574 (2002).

[66] N. R. Franklin and H. J. Dai, An enhanced CVD approach to extensive nanotube networks with directionality, Advanced Materials **12**, 890 (2000).

[67] Z. R. Abrams, Z. Ioffe, A. Tsukernik, O. Cheshnovsky, and Y. Hanein, A complete scheme for creating predefined networks of individual carbon nanotubes, Nano Letters **7**, 2666 (2007).

[68] Y. H. Lee, Y. T. Jang, C. H. Choi, D. H. Kim, C. W. Lee, J. E. Lee, Y. S. Han, S. S. Yoon, J. K. Shin, S. T. Kim, E. K. Kim, and B. K. Ju, Direct nanowiring of carbon nanotubes for highly integrated electronic and spintronic devices, Advanced Materials **13**, 1371 (2001).

[69] Y. S. Han, J. K. Shin, and S. T. Kim, Synthesis of carbon nanotube bridges on patterned silicon wafers by selective lateral growth, Journal of Applied Physics **90**, 5731 (2001).

[70] N. Chopra, P. D. Kichambare, R. Andrews, and B. J. Hinds, Control of multiwalled carbon nanotube diameter by selective growth

on the exposed edge of a thin film multilayer structure, Nano Letters **2**, 1177 (2002).

[71] A. Cao, R. Baskaran, M. J. Frederick, K. Turner, P. M. Ajayan, and G. Ramanath, Direction-selective and length-tunable in-plane growth of carbon nanotubes, Advanced Materials **15**, 1105 (2003).

[72] Y. G. Zhang, A. L. Chang, J. Cao, Q. Wang, W. Kim, Y. M. Li, N. Morris, E. Yenilmez, J. Kong, and H. J. Dai, Electric-field-directed growth of aligned single-walled carbon nanotubes, Applied Physics Letters **79**, 3155 (2001).

[73] A. Ural, Y. M. Li, and H. J. Dai, Electric-field-aligned growth of single-walled carbon nanotubes on surfaces, Applied Physics Letters **81**, 3464 (2002).

[74] J. B. K. Law, C. K. Koo, and J. T. L. Thong, Horizontally directed growth of carbon nanotubes utilizing self-generated electric field from plasma induced surface charging, Applied Physics Letters 243108 (2007).

[75] E. Joselevich and C. M. Lieber, Vectorial growth of metallic and semiconducting single-wall carbon nanotubes, Nano Letters **2**, 1137 (2002).

[76] H. Hongo, F. Nihey, and Y. Ochiai, Horizontally directional single-wall carbon nanotubes grown by chemical vapor deposition with a local electric field, Journal of Applied Physics **101**, (2007).

[77] H. B. Peng, T. G. Ristroph, G. M. Schurmann, G. M. King, J. Yoon, V. Narayanamurti, and J. A. Golovchenko, Patterned growth of single-walled carbon nanotube arrays from a vapor-deposited Fe catalyst, Applied Physics Letters **83**, 4238 (2003).

[78] K. H. Lee, J. M. Cho, and W. Sigmund, Control of growth orientation for carbon nanotubes, Applied Physics Letters **82**, 448 (2003).

[79] S. M. Huang, X. Y. Cai, C. S. Du, and J. Liu, Oriented long single walled carbon nanotubes on substrates from floating catalysts, Journal of Physical Chemistry B **107**, 13251 (2003).

[80] L. M. Huang, X. D. Cui, B. White, and S. P. O'Brien, Long and oriented single-walled carbon nanotubes grown by ethanol chemical vapor deposition, Journal of Physical Chemistry B **108**, 16451 (2004).

[81] W. W. Zhou, Z. Y. Han, J. Y. Wang, Y. Zhang, Z. Jin, X. Sun, Y. W. Zhang, C. H. Yan, and Y. Li, Copper catalyzing growth of single-walled carbon nanotubes on substrates, Nano Letters **6**, 2987 (2006).

[82] A. Reina, M. Hofmann, D. Zhu, and J. Kong, Growth mechanism of long and horizontally aligned carbon nanotubes by chemical vapor deposition, Journal of Physical Chemistry C **111**, 7292 (2007).

[83] Y. Liu, J. X. Hong, Y. Zhang, R. L. Cui, J. Y. Wang, W. C. Tan, and Y. Li, Flexible orientation control of ultralong single-walled carbon nanotubes by gas flow, Nanotechnology **20**, (2009).

[84] S. M. Huang, M. Woodson, R. Smalley, and J. Liu, Growth mechanism of oriented long single walled carbon nanotubes using "fast-heating" chemical vapor deposition process, Nano Letters **4**, 1025 (2004).

[85] Z. Jin, H. B. Chu, J. Y. Wang, J. X. Hong, W. C. Tan, and Y. Li, Ultralow feeding gas flow guiding growth of large-scale horizontally aligned single-walled carbon nanotube arrays, Nano Letters **7**, 2073 (2007).

[86] C. M. Orofeo, H. Ago, N. Yoshihara, and M. Tsuji, Top-down approach to align single-walled carbon nanotubes on silicon substrate, Applied Physics Letters **94**, (2009).

[87] T. Kamimura and K. Matsumoto, Controlling Direction of Growth of Carbon Nanotubes on Patterned SiO2 Substrate, Applied Physics Express **2**, (2009).

[88] C. Kocabas, S. J. Kang, T. Ozel, M. Shim, and J. A. Rogers, Improved synthesis of aligned arrays of single-walled carbon nanotubes and their implementation in thin film type transistors, Journal of Physical Chemistry C **111**, 17879 (2007).

[89] Seokwoo Jeon, Changgu Lee, Jinyao Tang, James Hone, and Colin Nuckolls, Growth of serpentine carbon nanotubes on quartz

substrates and their electrical properties, Nano Research **1**, 427 (2008).

[90] B. Zhang, G. Hong, B. Peng, J. Zhang, W. Choi, J. M. Kim, J. Y. Choi, and Z. Liu, Grow Single-Walled Carbon Nanotubes Cross-Bar in One Batch, Journal of Physical Chemistry C **113**, 5341 (2009).

[91] Y. Hayamizu, T. Yamada, K. Mizuno, R. C. Davis, D. N. Futaba, M. Yumura, and K. Hata, Integrated three-dimensional microelectromechanical devices from processable carbon nanotube wafers, Nature Nanotechnology **3**, 289 (2008).

[92] D. Routkevitch, A. A. Tager, J. Haruyama, D. Almawlawi, M. Moskovits, and J. M. Xu, Nonlithographic nano-wire arrays: Fabrication, physics, and device applications, Ieee Transactions on Electron Devices **43**, 1646 (1996).

[93] A. Thess, R. Lee, P. Nikolaev, H. J. Dai, P. Petit, J. Robert, C. H. Xu, Y. H. Lee, S. G. Kim, A. G. Rinzler, D. T. Colbert, G. E. Scuseria, D. Tomanek, J. E. Fischer, and R. E. Smalley, Crystalline ropes of metallic carbon nanotubes, Science **273**, 483 (1996).

[94] M. Tamura, Y. Kemmochi, Y. Murakami, N. Chino, M. Ogura, S. P. Naik, M. Takai, Y. Tsuji, S. Maruyama, and T. Okubo, Synthesis of single-walled carbon nanotubes in mesoporous silica film and their field emission property, Applied Physics a-Materials Science & Processing **84**, 247 (2006).

[95] C. Santini, D. J. Cott, A. Romo-Negreira, S. Riva-Sanseverino, S. De Gendt, and P. M. Vereecken, Growth and Electrical Characterisation of Horizontally aligned CNTs, ECS Transactions **18**, 845 (2009).

[96] C. A. Santini, D. J. Cott, A. Romo-Negreira, B. D. Capraro, S. R. Sanseverino, S. De Gendt, G. Groeseneken, and P. M. Vereecken, Growth and characterization of horizontally suspended CNTs across TiN electrode gaps, Nanotechnology **21**, (2010).

[97] D. R. Lide, *CRC Handbook of Chemistry and Physics*, 85th ed. (CRC Press, Boca Raton, 2004-2005).

[98] S. Hofmann, G. Csanyi, A. C. Ferrari, M. C. Payne, and J. Robertson, Surface diffusion: The low activation energy path for nanotube growth, Physical Review Letters **95**, (2005).

[99] M. Paunovic and M. Schlesinger, *Fundamentals of electrochemical deposition*, 2nd ed. (Wiley Interscience, ADDRESS, 2006).

[100] A. Kawabata, S. Sato, H. Shioya, T. Iwai, M. Nihei, D. Kondo, and Y. Awano, Direction-controlled growth of carbon nanotubes, Japanese Journal of Applied Physics **47**, 1975 (2008).

[101] J. N. Israelachvili, *Intermolecular and Surface Forces* (Academic Press, London, 1992).

[102] R. G. de Villoria, S. L. Figueredo, A. J. Hart, S. A. Steiner, A. H. Slocum, and B. L. Wardle, High-yield growth of vertically aligned carbon nanotubes on a continuously moving substrate, Nanotechnology **20**, (2009).

[103] Terrones M., Terrones H., Banhart F., Charlier J.-C., and Ajayan P.M., Coalescence of single-walled carbon nanotubes, Science **288**, 1226 (2000).

[104] C. H. Jin, K. Suenaga, and S. Iijima, Plumbing carbon nanotubes, Nature Nanotechnology **3**, 17 (2008).

[105] M. Terrones, F. Banhart, N. Grobert, J. C. Charlier, H. Terrones, and P. M. Ajayan, Molecular junctions by joining single-walled carbon nanotubes, Physical Review Letters **89**, (2002).

[106] S. Tuukkanen, S. Streiff, P. Chenevier, M. Pinault, H. J. Jeong, S. Enouz-Vedrenne, C. S. Cojocaru, D. Pribat, and J. P. Bourgoin, Toward full carbon interconnects: High conductivity of individual carbon nanotube to carbon nanotube regrowth junctions, Applied Physics Letters **95**, (2009).

[107] Li N., Chen X., Stoica L., Xia W., Qian J., Abmann J., Schuhmann W., and Muhler M., The catalytic synthesis of three-dimensional hierarchical carbon nanotube composites with high electrical conductivity based on electrochemical iron deposition, Advanced Materials **19**, 2957 (2007).

[108] Lepro X., Vega-Cant Y., Rodriguez-Macias F.J., Bando Y., Golberg D., and Terrones M., Production and characterisation of coaxial nanotube junctions and networks of CNx/CNT, Nano Letters **7**, 2220 (2007).

[109] Unger E., Duesberg G. S., Liebau M., Graham A. P., Seidel R., Kreupl F., and Hoenlein W., Decoration of multi-walled carbon nanotubes with noble- and transition-metal clusters and formation of CNT-CNT networks, Applied Physics A **77**, 735 (2003).

[110] M. S. Wang, D. Golberg, and Y. Bando, Interface Dynamic Behavior Between a Carbon Nanotube and Metal Electrode, Advanced Materials **22**, 93 (2010).

[111] T. L. Li, J. H. Ting, and B. Z. Yang, Conducting properties of suspended carbon nanotubes grown by thermal chemical vapor deposition, Journal of Vacuum Science & Technology B **25**, 1221 (2007).

[112] S. C. Lim, J. H. Jang, D. J. Bae, G. H. Han, S. Lee, I. S. Yeo, and Y. H. Lee, Contact resistance between metal and carbon nanotube interconnects: Effect of work function and wettability, Applied Physics Letters **95**, (2009).

[113] Q. Ngo, D. Petranovic, S. Krishnan, A. M. Cassell, Q. Ye, J. Li, M. Meyyappan, and C. Y. Yang, Electron transport through metal-multiwall carbon nanotube interfaces, Ieee Transactions on Nanotechnology **3**, 311 (2004).

[114] A. Felten, I. Suarez-Martinez, X. X. Ke, G. Van Tendeloo, J. Ghijsen, J. J. Pireaux, W. Drube, C. Bittencourt, and C. P. Ewels, The Role of Oxygen at the Interface between Titanium and Carbon Nanotubes, Chemphyschem **10**, 1799 (2009).

[115] J. O. Lee, C. Park, J. J. Kim, J. Kim, J. W. Park, and K. H. Yoo, Formation of low-resistance ohmic contacts between carbon nanotube and metal electrodes by a rapid thermal annealing method, Journal of Physics D-Applied Physics **33**, 1953 (2000).

[116] A. A. Kane, T. Sheps, E. T. Branigan, V. A. Apkarian, M. H. Cheng, J. C. Hemminger, S. R. Hunt, and P. G. Collins, Graphitic Electrical Contacts to Metallic Single-Walled Carbon Nanotubes Using Pt Electrodes, Nano Letters **9**, 3586 (2009).

[117] T. Saito, T. Yamada, D. Fabris, H. Kitsuki, P. Wilhite, M. Suzuki, and C. Y. Yang, Improved contact for thermal and electrical transport in carbon nanofiber interconnects, Applied Physics Letters **93**, (2008).

[118] L. F. Dong, S. Youkey, J. Bush, J. Jiao, V. M. Dubin, and R. V. Chebiam, Effects of local Joule heating on the reduction of contact resistance between carbon nanotubes and metal electrodes, Journal of Applied Physics **101**, (2007).

[119] P. M. Ryan, A. S. Verhulst, D. Cott, A. Romo-Negreira, T. Hantschel, and J. J. Boland, Optimization of multi-walled carbon nanotube-metal contacts by electrical stressing, Nanotechnology **21**, (2010).

[120] Y. Woo, G. S. Duesberg, and S. Roth, Reduced contact resistance between an individual single-walled carbon nanotube and a metal electrode by a local point annealing, Nanotechnology **18**, (2007).

[121] K. Rykaczewski, M. R. Henry, S. K. Kim, A. G. Fedorov, D. Kulkarni, S. Singamaneni, and V. V. Tsukruk, The effect of the geometry and material properties of a carbon joint produced by electron beam induced deposition on the electrical resistance of a multiwalled carbon nanotube-to-metal contact interface, Nanotechnology **21**, (2010).

[122] C. X. Chen, L. J. Yan, E. S. W. Kong, and Y. F. Zhang, Ultrasonic nanowelding of carbon nanotubes to metal electrodes, Nanotechnology **17**, 2192 (2006).

[123] L. Huang, E. F. Chor, Y. Wu, and Z. Guo, Investigations of niobium carbide contact for carbon-nanotube-based devices, Nanotechnology **21**, (2010).

[124] M. Zhang, Z. Y. Zhou, X. Yang, and X. Y. Ye, Pinning of single-walled carbon nanotubes by selective electrodeposition, Electrochemistry Communications **10**, 1559 (2008).

[125] H. O. Jacobs, H. F. Knapp, S. Muller, and A. Stemmer, Surface potential mapping: A qualitative material contrast in SPM, Ultramicroscopy **69**, 39 (1997).

[126] M. S. Wang, J. Y. Wang, Q. Chen, and L. M. Peng, Fabrication and electrical and mechanical properties of carbon nanotube interconnections, Advanced Functional Materials **15**, 1825 (2005).

[127] Q. Chen, S. Wang, and L. M. Peng, Establishing Ohmic contacts for in situ current-voltage characteristic measurements on a carbon nanotube inside the scanning electron microscope, Nanotechnology **17**, 1087 (2006).

[128] M. Nihei, M. Horibe, A. Kawabata, and Y. Awano, Simultaneous formation of multiwall carbon nanotubes and their end-bonded ohmic contacts to Ti electrodes for future ULSI interconnects, Japanese Journal of Applied Physics Part 1-Regular Papers Short Notes & Review Papers **43**, 1856 (2004).

[129] N. Srivastava and K. Banerjee, Performance analysis of carbon nanotube interconnects for VLSI applications, Iccad-2005: International Conference on Computer Aided Design, Digest of Technical Papers 383 (2005).

[130] C. Berger, P. Poncharal, Y. Yi, and W. de Heer, Ballistic conduction in multiwalled carbon nanotubes, Journal of Nanoscience and Nanotechnology **3**, 171 (2003).

[131] S. D. Li, Z. Yu, C. Rutherglen, and P. J. Burke, Electrical properties of 0.4 cm long single-walled carbon nanotubes, Nano Letters **4**, 2003 (2004).

[132] M. S. Purewal, B. H. Hong, A. Ravi, B. Chandra, J. Hone, and P. Kim, Scaling of resistance and electron mean free path of single-walled carbon nanotubes, Physical Review Letters **98**, (2007).

[133] Y. Chai, Z. Y. Xiao, and P. C. H. Chan, Horizontally aligned carbon nanotube bundles for interconnect application: diameter-dependent contact resistance and mean free path, Nanotechnology **21**, (2010).

[134] P. W. Chiu and S. Roth, Carbon nanotube nanocontact in T-junction structures, Applied Physics Letters **91**, (2007).

[135] Y. Matsuda, W. Q. Deng, and W. A. Goddard, Contact resistance properties between nanotubes and various metals from quantum mechanics, Journal of Physical Chemistry C **111**, 11113 (2007).

[136] C. Lan, P. Srisungsitthisunti, P. B. Amama, T. S. Fisher, X. F. Xu, and R. G. Reifenberger, Measurement of metal/carbon nanotube contact resistance by adjusting contact length using laser ablation, Nanotechnology **19**, (2008).

[137] K. Molhave, S. B. Gudnason, A. T. Pedersen, C. H. Clausen, A. Horsewell, and P. Boggild, Transmission electron microscopy study of individual carbon nanotube breakdown caused by Joule heating in air, Nano Letters **6**, 1663 (2006).

[138] C. Berger, Y. Yi, J. Gezo, P. Poncharal, and W. A. de Heer, Contacts, non-linear transport effects and failure in multi-walled carbon nanotubes, New Journal of Physics **5**, (2003).

[139] Ba L., Shu J., Lu Z. H., Li J. T., Lei W., Wang B. P., and Li W. S., Probing local electric field distribution of nanotube arrays using electrostatic force microscopy, JOURNAL OF APPLIED PHYSICS **93**, 9977 (2003).

[140] He Y. R., Ong H. G., Zhao Y., He S. L., Li L. J., and Wang J. L., Study of Charge Diffusion at the Carbon Nanotube-SiO2 Interface by Electrostatic Force Microscopy, JOURNAL OF PHYSICAL CHEMISTRY C **113**, 15476 (2009).

[141] Pisana S., Zhang C., Ducati C., Hofmann S., and Robertson J., Enhanced subthreshold slopes in large diameter single wall carbon nanotube field effect transistors, IEEE TRANSACTIONS ON NANOTECHNOLOGY **7**, 458 (2008).

[142] T. D. Yuzvinsky, W. Mickelson, S. Aloni, G. E. Begtrup, A. Kis, and A. Zettl, Shrinking a carbon nanotube, Nano Letters **6**, 2718 (2006).

[143] A. Subramanian, L. X. Dong, J. Tharian, U. Sennhauser, and B. J. Nelson, Batch fabrication of carbon nanotube bearings, Nanotechnology **18**, (2007).

[144] V. V. Deshpande, H. Y. Chiu, H. W. C. Postma, C. Miko, L. Forro, and M. Bockrath, Carbon nanotube linear bearing nanoswitches, Nano Letters **6**, 1092 (2006).

[145] A. Barreiro, R. Rurali, E. R. Hernandez, J. Moser, T. Pichler, L. Forro, and A. Bachtold, Subnanometer motion of cargoes driven

by thermal gradients along carbon nanotubes, Science **320**, 775 (2008).

[146] H. Somada, K. Hirahara, S. Akita, and Y. Nakayama, A Molecular Linear Motor Consisting of Carbon Nanotubes, Nano Letters **9**, 62 (2009).

[147] B. C. Regan, S. Aloni, K. Jensen, R. O. Ritchie, and A. Zettl, Nanocrystal-powered nanomotor, Nano Letters **5**, 1730 (2005).

[148] B. C. Regan, S. Aloni, R. O. Ritchie, U. Dahmen, and A. Zettl, Carbon nanotubes as nanoscale mass conveyors, Nature **428**, 924 (2004).

[149] L. X. Dong, X. Y. Tao, M. Hamdi, L. Zhang, X. B. Zhang, A. Ferreira, and B. J. Nelson, Nanotube Fluidic Junctions: Internanotube Attogram Mass Transport through Walls, Nano Letters **9**, 210 (2009).

[150] W. Y. Jang, N. N. Kulkarni, C. K. Shih, and Z. Yao, Electrical characterization of individual carbon nanotubes grown in nanoporous anodic alumina templates, Applied Physics Letters **84**, 1177 (2004).

[151] W. Yi, L. Lu, D. L. Zhang, Z. W. Pan, and S. S. Xie, Linear specific heat of carbon nanotubes, Physical Review B **59**, R9015 (1999).

[152] E. Pop, D. Mann, Q. Wang, K. Goodson, and H. J. Dai, Thermal conductance of an individual single-wall carbon nanotube above room temperature, Nano Letters **6**, 96 (2006).

[153] Y. H. Lee, J. H. Lee, S. J. Chung, S. Lee, and B. K. Ju, Carrier carrying capacity of one-step grown suspended carbon nanotube bridge with carbon nanotube contact electrodes: For practical one-dimensional electronics, Applied Physics Letters **89**, (2006).

[154] T. D. Yuzvinsky, W. Mickelson, S. Aloni, S. L. Konsek, A. M. Fennimore, G. E. Begtrup, A. Kis, B. C. Regan, and A. Zettl, Imaging the life story of nanotube devices, Applied Physics Letters **87**, (2005).

[155] Y. Wei, P. Liu, K. L. Jiang, L. Liu, and S. S. Fan, Breaking single-walled carbon nanotube bundles by Joule heating, Applied Physics Letters **93**, (2008).

[156] L. Shi, J. H. Zhou, P. Kim, A. Bachtold, A. Majumdar, and P. L. McEuen, Thermal probing of energy dissipation in current-carrying carbon nanotubes, Journal of Applied Physics **105**, (2009).

[157] T. Y. Choi, D. Poulikakos, J. Tharian, and U. Sennhauser, Measurement of thermal conductivity of individual multiwalled carbon nanotubes by the 3-omega method, Applied Physics Letters **87**, (2005).

[158] P. Poncharal, C. Berger, Y. Yi, Z. L. Wang, and W. A. de Heer, Room temperature ballistic conduction in carbon nanotubes, Journal of Physical Chemistry B **106**, 12104 (2002).

[159] C.A. Santini, A. Volodin, C. Van Haesendonck, S. De Gendt, G. Groeseneken, and P.M. Vereecken, CNT-CNT contact: an alternative towards low resistance horizontal interconnects, in submission (2010).

[160] G. E. Begtrup, K. G. Ray, B. M. Kessler, T. D. Yuzvinsky, H. Garcia, and A. Zettl, Probing nanoscale solids at thermal extremes, Physical Review Letters **99**, (2007).

[161] V. V. Deshpande, S. Hsieh, A. W. Bushmaker, M. Bockrath, and S. B. Cronin, Spatially Resolved Temperature Measurements of Electrically Heated Carbon Nanotubes, Physical Review Letters **102**, (2009).

[162] H. Y. Chiu, V. V. Deshpande, H. W. C. Postma, C. N. Lau, C. Miko, L. Forro, and M. Bockrath, Ballistic phonon thermal transport in multiwalled carbon nanotubes, Physical Review Letters **95**, (2005).

[163] H. Maune, H. Y. Chiu, and M. Bockrath, Thermal resistance of the nanoscale constrictions between carbon nanotubes and solid substrates, Applied Physics Letters **89**, (2006).

[164] M. A. Kuroda and J. P. Leburton, Joule heating induced negative differential resistance in freestanding metallic carbon nanotubes, Applied Physics Letters **89**, (2006).

[165] E. Pop, Energy Dissipation and Transport in Nanoscale Devices, Nano Research **3**, 147 (2010).

[166] J. Cao, Q. Wang, and H. Dai, Electron transport in very clean, as-grown suspended carbon nanotubes, Nature Materials **4**, 745 (2005).

[167] X. Y. Huang, Z. Y. Zhang, Y. Liu, and L. M. Peng, Analytical analysis of heat conduction in a suspended one-dimensional object, Applied Physics Letters **95**, (2009).

[168] P. M. Ajayan, T. W. Ebbesen, T. Ichihashi, S. Iijima, K. Tanigaki, and H. Hiura, Opening Carbon Nanotubes with Oxygen and Implications for Filling, Nature **362**, 522 (1993).

[169] A. Subramanian, T. Y. Choi, L. X. Dong, J. Tharian, U. Sennhauser, D. Poulikakos, and B. J. Nelson, Local control of electric current driven shell etching of multiwalled carbon nanotubes, Applied Physics a-Materials Science & Processing **89**, 133 (2007).

[170] J. G. Park, S. Li, R. Liang, X. Fan, C. Zhang, and B. Wang, The high current-carrying capacity of various carbon nanotube-based buckypapers, Nanotechnology **19**, (2008).

[171] N. Mingo and D. A. Broido, Length dependence of carbon nanotube thermal conductivity and the "problem of long waves", Nano Letters **5**, 1221 (2005).

[172] R. Prasher, Thermal boundary resistance and thermal conductivity of multiwalled carbon nanotubes, Physical Review B **77**, (2008).

[173] Q. W. Li, C. H. Liu, and S. S. Fan, Thermal Boundary Resistances of Carbon Nanotubes in Contact with Metals and Polymers, Nano Letters **9**, 3805 (2009).

[174] M. A. Worsley, J. D. Kuntz, P. J. Pauzauskie, O. Cervantes, J. M. Zaug, A. E. Gash, J. H. Satcher, and T. F. Baumann, High surface area carbon nanotube-supported titanium carbonitride aerogels, Journal of Materials Chemistry **19**, 5503 (2009).

[175] J. Weldon, K. Jensen, and A. Zettl, Nanomechanical radio transmitter, Physica Status Solidi B-Basic Solid State Physics **245**, 2323 (2008).

[176] K. Jensen, K. Kim, and A. Zettl, An atomic-resolution nanomechanical mass sensor, Nature Nanotechnology **3**, 533 (2008).

[177] H. Y. Chiu, P. Hung, H. W. C. Postma, and M. Bockrath, Atomic-Scale Mass Sensing Using Carbon Nanotube Resonators, Nano Letters **8**, 4342 (2008).

[178] V. Sazonova, Y. Yaish, H. Ustunel, D. Roundy, T. A. Arias, and P. L. McEuen, A tunable carbon nanotube electromechanical oscillator, Nature **431**, 284 (2004).

[179] A. K. Huttel, G. A. Steele, B. Witkamp, M. Poot, L. P. Kouwenhoven, and H. S. J. van der Zant, Carbon Nanotubes as Ultrahigh Quality Factor Mechanical Resonators, Nano Letters **9**, 2547 (2009).

[180] J. A. Weldon, B. Aleman, A. Sussman, W. Gannett, and A. K. Zettl, Sustained Mechanical Self-Oscillations in Carbon Nanotubes, Nano Letters **10**, 1728 (2010).

[181] J. Gaillard, R. Ciocan, M. Skove, and A. M. Rao, Electrical detection of oscillations in micro- and nano-cantilevers using harmonic detection of resonance, Material and Devices for Smart Systems II **888**, 35 (2006).

[182] A. Volodin, D. Buntinx, M. Ahlskog, A. Fonseca, J. B. Nagy, and C. Van Haesendonck, Coiled carbon nanotubes as self-sensing mechanical resonators, Nano Letters **4**, 1775 (2004).

[183] A. Volodin, C. Van Haesendonck, R. Tarkiainen, M. Ahlskog, A. Fonseca, and J. B. Nagy, AFM detection of the mechanical resonances of coiled carbon nanotubes, Applied Physics a-Materials Science & Processing **72**, S75 (2001).

[184] D. Garcia-Sanchez, A. S. Paulo, M. J. Esplandiu, F. Perez-Murano, L. Forro, A. Aguasca, and A. Bachtold, Mechanical detection of carbon nanotube resonator vibrations, Physical Review Letters **99**, (2007).

[185] S. T. Purcell, P. Vincent, C. Journet, and V. T. Binh, Tuning of nanotube mechanical resonances by electric field pulling, Physical Review Letters **89**, (2002).

[186] S. Kuehn, S. A. Hickman, and J. A. Marohn, Advances in mechanical detection of magnetic resonance, Journal of Chemical Physics **128**, (2008).

[187] D. Rugar, C. S. Yannoni, and J. A. Sidles, Mechanical Detection of Magnetic-Resonance, Nature **360**, 563 (1992).

[188] Wei B., Zhang Z. J., Ramanath G., and Ajayan P. M., Lift-up growth of aligned carbon nanotube patterns, Applied Physics Letters **77**, 2985 (2000).

[189] D. H. Wu, W. T. Chien, C. S. Chen, and H. H. Chen, Resonant frequency analysis of fixed-free single-walled carbon nanotube-based mass sensor, Sensors and Actuators a-Physical **126**, 117 (2006).

[190] J. Mertens, E. Finot, T. Thundat, A. Fabre, M. H. Nadal, V. Eyraud, and E. Bourillot, Effects of temperature and pressure on microcantilever resonance response, Ultramicroscopy **97**, 119 (2003).

[191] G. Y. Chen, R. J. Warmack, A. Huang, and T. Thundat, Harmonic Response of near-Contact Scanning Force Microscopy, Journal of Applied Physics **78**, 1465 (1995).